Understanding the mechanical response of bacterial cell walls and cell membranes against antimicrobial agents

By

Garima Rani

PHYS10201504003

The Institute of Mathematical Sciences, Chennai

A thesis submitted to the

Board of Studies in Physical Sciences

In partial fulfillment of requirements

for the Degree of

DOCTOR OF PHILOSOPHY

of

HOMI BHABHA NATIONAL INSTITUTE

August, 2020

Homi Bhabha National Institute

Recommendations of the Viva Voce Committee

As members of the Viva Voce Committee, we certify that we have read the dissertation prepared by Garima Rani entitled "Understanding the mechanical response of bacterial cell walls and cell membranes against antimicrobial agents" and recommend that it may be accepted as fulfilling the thesis requirement for the award of Degree of Doctor of Philosophy.

Chairman - Rajesh Ravindran — Date: 4. Jan.2021

Guide/Convenor - Satyavani Vemparala — Date: 4. Jan.2021

Examiner - Prof K Ganapathy Ayappa — Date: 4. Jan.2021

Member 1 - Sanatan Digal — Date: 4. Jan.2021

Member 2 - Sibasish Ghosh — Date: 4. Jan.2021

Member 3 - Pinaki Chaudhuri — Date: 4. Jan.2021

Final approval and acceptance of this thesis is contingent upon the candidate's submission of the final copies of the thesis to HBNI.

I hereby certify that I have read this thesis prepared under my direction and recommend that it may be accepted as fulfilling the thesis requirement.

Date: 4. Jan.2021

Place: Chennai

Satyavani Vemparala
Guide

STATEMENT BY AUTHOR

This dissertation has been submitted in partial fulfillment of requirements for an advanced degree at Homi Bhabha National Institute (HBNI) and is deposited in the Library to be made available to borrowers under rules of the HBNI.

Brief quotations from this dissertation are allowable without special permission, provided that accurate acknowledgement of source is made. Requests for permission for extended quotation from or reproduction of this manuscript in whole or in part may be granted by the Competent Authority of HBNI when in his or her judgement the proposed use of the material is in the interests of scholarship. In all other instances, however, permission must be obtained from the author.

Garima Rani

DECLARATION

I hereby declare that the investigation presented in the thesis has been carried out by me. The work is original and has not been submitted earlier as a whole or in part for a degree / diploma at this or any other Institution / University.

Garima Rani

LIST OF PUBLICATIONS ARISING FROM THE THESIS

1. "Importance of being cross-linked for the bacterial cell wall",
   Garima Rani and Issan Patri,
   Phys. Rev. E 100, 062408 (2019).

2. "Modelling heterogeneities in the crosslinked bacterial sacculus",
   Garima Rani and Issan Patri,
   Phys. Rev. Research 2, 013090 (2020).

3. "Aggregation of methacrylate-based ternary biomimetic polymers in solution",
   Garima Rani, Kenichi Kuroda and Satyavani Vemparala,
   J. Phys.: Condens. Matter 33, 064003 (2020).

4. "Towards designing globular antimicrobial peptide mimics: role of polar functional groups in biomimetic ternary antimicrobial polymers",
   Garima Rani, Kenichi Kuroda and Satyavani Vemparala,
   Soft Matter, DOI: 10.1039/D0SM01896A (2021) .

5. "The function of peptide-mimetic anionic functionality and salt bridge in the antimicrobial activity and conformation of cationic amphiphilic copolymers",
   Rajani Bhat[§], Leanna Foster[§], **Garima Rani**[§], Satyavani Vemparala and Kenichi Kuroda,
   Submitted (2020).

[§]Equal contribution.

[‡]Other Journal Publications

1. "Impurity-induced current in a Chern insulator",
   Vibhuti Jha[§], **Garima Rani**[§] and R. Ganesh,
   Phys. Rev. B 95, 115434 (2017).

2. "Modeling cell-substrate de-adhesion dynamics under fluid shear",
   Renu Maan, **Garima Rani**, Gautam I. Menon and Pramod A. Pullarkat,
   Physical Biology 15, 046006 (2018).

Garima Rani

[‡]Not part of this thesis.
[§]Equal contribution.

List of presentations and participations at conferences

1. EMBO Workshop on Experimental and Theoretical approaches to Cell Mechanics, RRI and NCBS, Bangalore, 2017.
2. Bangalore School on Statistical Physics, ICTS, Bangalore, 2017.
3. ICTP-ICTS Winter School on Quantitative Systems Biology, ICTS, Bangalore, 2017.
4. Poster presentation, Indian Statistical Physics Community Meeting, ICTS, Bangalore, 2018.
5. Talk presentation, Compbio Annual Meeting, Institute of Mathematical Sciences, Chennai, 2018.
6. Talk presentation, PALM international summer school - Physical approach to understanding microbial life, Gif-sur-Yvette, France, 2018.
7. Poster presentation, EMBO Workshop, Physics of Integrated Biological systems, Cargese, France, 2018.
8. Talk presentation, 12th International Conference on Complex Fluids and Soft Matter (COMPFLU-18), IIT Roorkee, 2018.
9. Talk presentation, 2nd Mechanobiology Meeting, Quy Nhon, Vietnam, 2019.
10. Poster presentation, EMBO Symposia, Mycobacterial Heterogeneity and Host Tissue Tropism, National Institute of Immunology (NII) and International Centre of Genetic Engineering & Biotechnology (ICGEB), New Delhi, 2020.

Research visits and seminars

1. Seminar, Dept. of Physics and Astrophysics, University of Delhi, April 2018.

2. Seminar, Raman Research Institute, Bangalore, May 2018.

3. Research intern, Mechanobiology Institute, NUS Singapore, December 2019.

Anirvedam cha daakshyam cha manasashchaaparaajayam

Karyasiddhikaraanyaahuh

-Valmiki Ramayana, Kaand 4: Parva 49: Shloka 6

Dedicated to my beloved grandfather

ACKNOWLEDGEMENTS

First and foremost, I am thankful to my advisor Prof. Satyavani Vemparala for providing me tremendous support and encouragement throughout my PhD journey. She gave me a lot of confidence by allowing me freedom to explore research directions. Her valuable suggestions, comments and guidance have appreciably enhanced the quality of my work. I am also grateful to her for supporting me to attend various conferences and visits to present my work.

I would like to thank my doctoral committee members Prof. R. Rajesh, Prof. Sanatan Digal, Prof. Sibasish Ghosh and Prof. Pinaki Chaudhuri for encouragement and suggestions on my work. Special thanks to Prof. R. Rajesh for running the random excursions journal club, in which I delivered talks on some beautiful papers, which has been a memorable experience for me.

I would like to thank my collaborators Dr. Issan Patri, Prof. Kenichi Kuroda, Dr. Rajani Bhat, Dr. Leanna Foster, Dr. R. Ganesh, Vibhuti Jha, Dr. Renu Maan, Prof. Gautam I. Menon and Prof. Pramod Pullarkat. I am indebted towards Prof. Gautam I. Menon, Dr. R. Ganesh and Dr. Issan Patri for the various fruitful discussions during the initial years of my PhD which helped me learn a lot about the subject and research in general. I am thankful to Prof. Yashodhan Hatwalne for giving me chance to visit Raman Research Institute and for various lengthy and meaningful discussions on continuum physics, which laid the foundation of my research. I acknowledge Prof. Namrata Gundiah, Prof. Mandar M. Inamdar for the amazing discussions on physics of cells.

I am thankful to my M.Sc teachers at University of Delhi, Prof. Debajyoti choudhury, Prof. Sanjay Jain, Prof. Patrick Das Gupta, Prof. Swarnendu Sarkar and

Prof. T.R Seshadri, from whom I have learnt a lot. My gratitude to Prof. Sanjay Jain, supervisor of my M.Sc dissertation project, in which I took my first baby steps into the world of bacteria. I express my sincere thanks to Prof. KPN Murthy for allowing me to attend his classes on Monte Carlo Methods in CMI, which helped me learn a lot. I am also indebted to him for his guidance and encouragement.

I would like to thank various conferences and workshops where I got a chance to present my research. I am thankful to get an opportunity to have inspiring discussions with eminent researchers of the bacterial cell wall, whose works have had a strong influence on me, including Prof. KC Huang, Prof. Sean X. Sun, Prof. Sven van Teeffelen, Prof. Vincent Fromion and Dr. Cyrille Billaudeau. I am thankful to Prof. Anupam Sengupta and Dr. Tetsuya Hiraiwa for the various constructive discussions and for their encouragement, which pushed me to do better work. I am grateful to Dr. Tetsuya Hiraiwa for giving me the opportunity to do internship in Mechanobiology Institute, where I had some awesome discussions with him and his research group. I will always cherish the amazing experiences I had, of meetings and discussions with Dr. Omkar Deshmukh, Dr. Sharareh Tavaddod and Dr. Yanina Alvarez.

For my work I have extensively used the high performance computing facilities of IMSc, special thanks to the clusters Nandadevi and Annapurna. I am very thankful to computing support staff at IMSc, especially Mr. Mangal Pandi and Mr. Srinivasan for troubleshooting any and every issue that cropped up at any hour of time. A huge thanks to members of IMSc administration and library staff for providing a positive atmosphere to carry out this research work in a peaceful manner. I am also grateful to support staff, especially Mahalakshmi aunty for being so loving and caring to me.

Very thankful to my friends- Janani, Surabhi, Amir, Pooja, Sudharsan, Anbu, Sarjick and my office mates Pratik, Anuj, Amit and Roohani. Special thanks to Janani

for her encouragement and help, during my darkest phase in IMSc. Thanks for all the fun we had together- walks, temple visits and food trips! I would like to thank Subhankar and Srivatsa for various discussions during PhD course work. I am thankful to Shivam and Himalaya for the lengthy discussions we had on various problems, which I am hopeful will lead to some interesting results in future.

I would once again like to thank Issan for helping me cross every hurdle in these 5 years. Thanks for everything, for being a great friend and support. Let's hope we work on many more interesting projects together.

Finally, I wish to thank my family- my parents, brother, bhabhi and nephew. Thanks to my parents for allowing me to stay away from home and pursue my PhD, but also for being there to listen when I needed them, to share my frustrations. Heartfelt thanks to my Late Grandparents, for their unconditional love and blessings. Besides this, I would like to extend my sincere thanks to all who have directly or indirectly helped me in the successful completion of this work.

Abstract

In this thesis, we employ biophysical methods to study the design principles of the bacterial cell wall and to study the efficacy of biomimetic methacrylate polymers as antimicrobial agents. Specifically, in the first part of the thesis, we explore the design principles underpinning the viability of the cell wall of bacteria, which is primarily composed of the peptidoglycan (PG) network, a mesh of relatively long and stiff glycan chains, cross-linked intermittently by flexible peptides. We examine the molecular level architecture of the PG mesh and its role in enhancing the toughness or the resistance to crack propagation, of the cell wall. We also investigate the effect of variability in the elastic properties of the PG mesh on its bulk mechanical response, by studying an appropriately modelled spring system using theoretical methods and simulations. In the second part of the thesis, we study the conformational landscape, aggregation dynamics and interactions with model bacterial membrane of biomimetic methacrylate ternary antimicrobial polymers (AMPolys), utilizing detailed atomistic molecular dynamics simulations. Our aim here is to go beyond the traditional binary composition design, constituting hydrophobic and charged cationic groups, of such AMPolys, by including additional functional groups in order to better optimize their antimicrobial action. We specifically examine the role played by neutral polar groups in influencing the aggregation dynamics of such polymers in solution phase and study their membrane-interactions in depth. Further, we also investigate the conformational landscape of AMPolys that have anionic functional groups as constituents, with particular focus on probing the formation of salt bridges and their role in determining the conformational dynamics of such polymers.

Contents

List of Figures

List of Tables

Chapter 1

Introduction

Bacteria are microscopic, prokaryotic, single celled organisms that are some of the first life forms to have appeared on Earth. One of the most successful organisms, bacteria are adapted to thrive in staggeringly diverse environments ranging from soil, water, human gut, hot springs, marshlands, even radioactive waste, that no higher form of life manage to survive in [1, 24]. Typically, bacteria are an order of magnitude smaller than eukaryotic cells. However, a wide diversity in the dimensions of bacterial cells has been observed, with the smallest known bacteria, members of the class *Mycoplasma*, measuring only around 200 - 300 nm in size [25], while the largest bacteria are clearly visible to the naked eye, for example *Thiomargarita namibiensis* is around 5 mm long [26]. The morphological diversity of bacteria is also displayed by a large variation in shapes of the bacterial cells, ranging from spherical (e.g. *Staphylococcus aureus*) to rod shaped (e.g. *Escherichia coli*) and spiral shaped (e.g. *Helicobacter pylori*) to even more exotic shapes like star shaped (e.g. bacteria of genus *Stella*) and square (e.g. *Haloquadratum walsbyi*)[27, 28].

Bacteria form complex and varied associations with other organisms including humans. Many species of bacteria like *Lactobacillus*, *Bifidobacteria*, *Streptococcus thermophilus* have a peaceful coexistence with humans, often playing a beneficial role, for

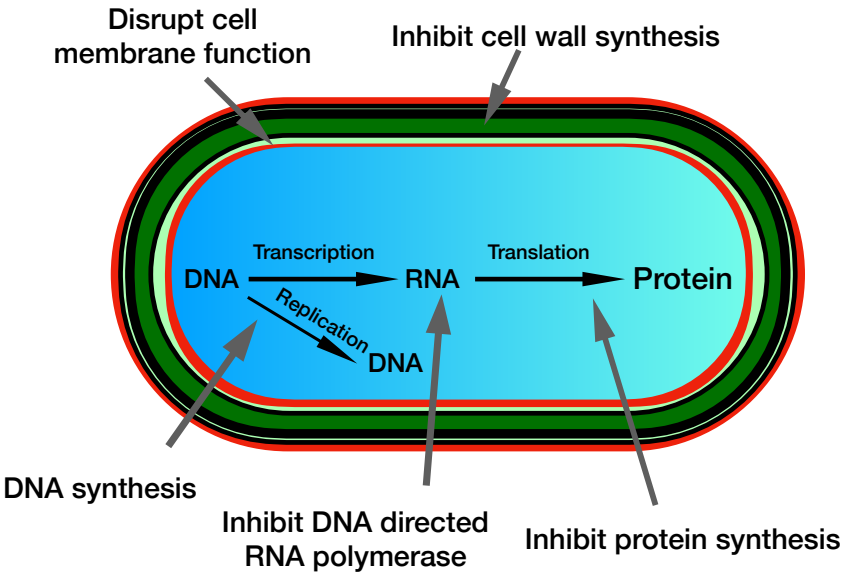

Figure 1.1: Schematic representation of the mode of action of various antibacterial agents, which target different components of the bacterial cell. For example, penicillin and other β-lactam antibiotics target cell wall synthesis, rifamycins and rifampin inhibit RNA synthesis or antibacterial agents like lipopeptide and polymyxins disrupt plasma membrane of the cell [29].

instance in the human digestive system. However, while only about 5% of bacterial species are pathogenic, they are responsible for several atrocious and life threatening diseases. For instance, *Escherichia coli* (*E.coli*) is responsible for some of the most frequently caused bacterial infections, including urinary tract infection (UTI), meningitis, diarrhea [30]. Pathogenic bacteria cause several other diseases such as tuberculosis, pneumonia, typhus, plague, diphtheria, typhoid, cholera, syphilis, and leprosy [2]. The primary line of defence against such bacterial infections thus far has been antibiotics. Antibiotics are effective therapeutic agents that fight bacterial infections either by killing bacteria or slowing its growth, usually by impeding crucial cellular functions in the bacterial cell like cell wall synthesis, protein synthesis in the cell and other similar functions (Fig. 1.1). However, in recent times several strains of bacteria have displayed an alarming rise in resistance to antibiotic treatment. This has rendered several commonly used antibiotics largely ineffective. The graveness of the problem can be gauged from the fact that strains of *E.coli* bacteria

have even developed resistance to colistin and carbapenem, two "last resort" antibiotics [3]. This presents an immensely daunting public health crisis, so much so that it is estimated that by 2050, infections from multi-drug resistant pathogens will cause higher mortality than cancer [4]. Therefore, exploration and design of newer antibacterial agents is urgently imperative. For this, an important pathway is to utilize biophysical methods to unravel the design principles of the bacterial cell and to model the action of antimicrobial agents on them, thus enabling us to effectively design and test the efficacy of new age antibacterials.

1.1 Bacterial cell envelope

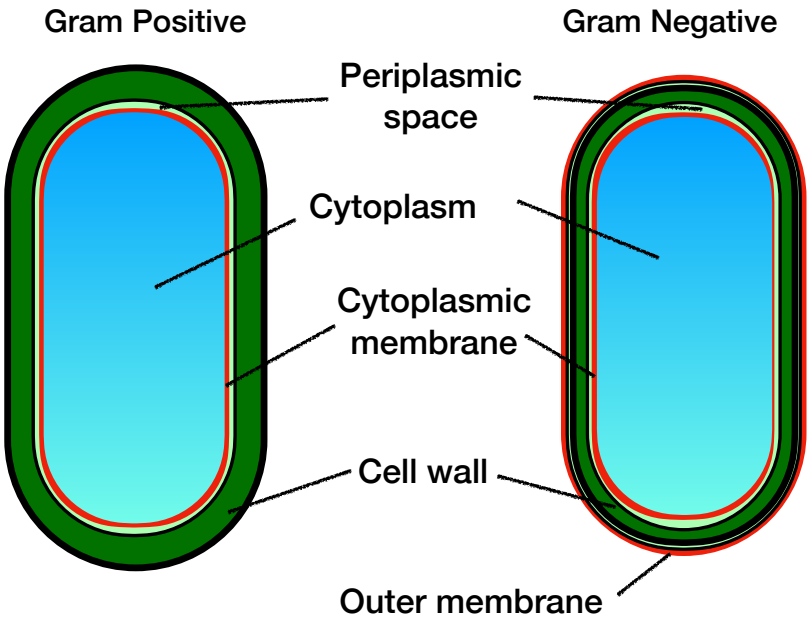

Figure 1.2: Structure of Gram-positive and Gram-negative bacteria.

The bacterial cell structure is constantly under challenges, often arising from the highly challenging habitats in which it grows. The bacterial cell envelope, which is the structure that surrounds the cytoplasm of the cell, is the primary defence of the cell against such hostile conditions. It is the essential and primary determinant of cell shape, while counteracting the high internal pressure caused by osmotic flow

of water, referred to as turgor pressure. Unlike animal cells which usually have a definite boundary of only the plasma membrane that separates the interior of the cell from the outside environment, the bacterial cell envelope is a complex multi-component structure [31]. Based on the fundamental structural difference in the cell envelope, bacteria are broadly classified into two classes, Gram-positive and Gram-negative bacteria, based on the more than 100 year old Gram staining procedure [32]. One group of bacteria retain the stain, referred to as Gram-positive, and the other do not, referred to as Gram-negative bacteria (Fig. 1.2). In both classes of bacteria, cell envelope is constituted of a phospholipid bilayer, referred to plasma membrane or inner membrane or cell membrane, which is encased by a relatively rigid exoskeleton, referred to as the cell wall, that plays the key structural role in determining cell shape (the space in between the cell membrane and the cell wall is referred to as the periplasmic space). A suitable analogy of this structure is given by comparing it with a rubber tyre with an inner tube [33], with the inner tube acting analogous to the cell membrane, sealing off the interior of the tyre and the tyre itself acting similarly as the cell wall, resisting the pressure built up inside while allowing the tyre to sustain its shape. In Gram-negative bacteria however, the cell wall itself is further surrounded by a second lipid bilayer, referred to as the outer membrane, which consists of phospholipids only on the inner leaflet and lipopolysaccharides on the outer leaflet [31]. Being critical for the survival of the cell, it is not surprising that the cell envelope is a major target for a range of antibacterial agents, including antibiotics, antimicrobial peptides and biomimetic antimicrobial polymers [34, 35, 36, 37].

1.2 Cell wall design principles

The cell wall is a structural layer of the bacterial cell which forms a rigid protective casing surrounding the cell, just outside its inner membrane. The cell wall plays

a definitive role in controlling cell shape, growth and division of bacteria [5, 28]. Understanding its structure holds particular significance due to its necessity for the survival of bacterial cells and due to it being absent in mammalian cells, making it an ideal target for several powerful antibiotics, including β-lactam antibiotics like penicillin [38, 39]. In both Gram-negative and Gram-positive bacteria, the primary component of the cell wall is the polymer peptidoglycan (PG), also called murein (Fig. 1.3). The chemical composition of the peptidoglycan structure is largely conserved across the vast majority of bacterial species: it is a sturdy mesh of relatively rigid glycan chains, which are made up of repeating units of the disaccharides *N*-acetylglucosamine (Glc*N*Ac or NAG) and *N*-acetylmuramic acid (Mur*N*Ac or NAM), connected by glycosidic bonds and cross-linked intermittently by stretchable peptides - peptide stems are attached to the the lactyl group of the NAM residues, typically containing 5 amino acids in the sequence L-alanine (L-ALA), D-iso-glutamate (GLU), meso-diamino pimelic acid (DAP), D-alanine (D-ALA) and D-alanine (D-ALA), with the cross-linking generally occurring between the carboxyl group of the position 4 D-ALA and the amino group of the position 3 DAP [5]. Indeed, it is the largest occurring macromolecule in nature [5, 9]. Gram-positive and Gram-negative bacterial cell walls differ in their thickness - in Gram-negative bacteria, the cell wall is a thin network (3-7 nm) between the inner membrane and the outer membrane, while in Gram-positive bacteria, it is an order of magnitude thicker (20-100 nm) [5]. As mentioned in Section 1.1, the bacterial cell is under high internal pressure referred to as turgor pressure. This pressure can be remarkably high (e.g. $\sim 1-3$ atm for Gram-negative bacteria like *E.coli* and ~ 20 atm for Gram-positive bacteria like *B.subtilis*) and a primary function of the cell wall is to resist this pressure, thus allowing the cell to maintain its characteristic shape and remain viable [5]. Indeed, cell wall deficient strains of *E.coli*, referred to as L-forms, have been isolated under appropriate conditions and it has been observed that such strains lack the rod shape of wild type *E.coli*, instead having a more spherical shape, underlining the

importance of the cell wall of bacteria in maintaining its characteristic shape [31].

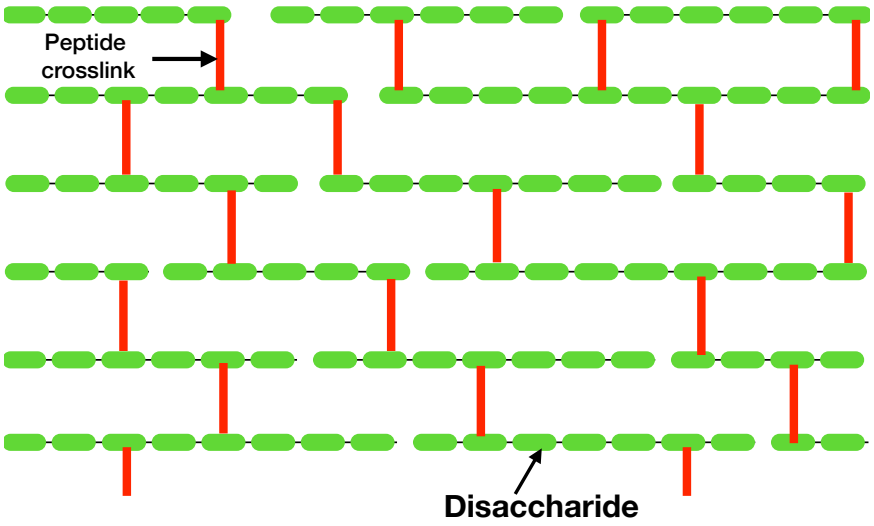

Figure 1.3: Illustrative description of the structure of the peptidoglycan (PG) mesh. The glycan chains are made up of alternating units N-acetylglucosamine (Glc$N$Ac or NAG) and N-acetylmuramic acid (Mur$N$Ac or NAM), connected by a glycosidic bond, referred to as a disaccharide unit. These sugar chains are cross-linked intermittently by stretchable peptide bonds.

Structure of the peptidolgycan mesh

We now discuss the structure of the peptidoglycan mesh, focussing particularly on the case of the rod shaped, Gram-negative bacteria *E.coli*. It is notable that *E.coli*, which is typically around 1-2 μm in length and around 0.5 μm in radius, is one of the most widely studied bacterial species, often referred to as the lab workhorse, due to its extensive use in experiments performed in laboratory setting [40]. While the chemical features of the cell wall peptidoglycan are well studied and understood for a long time, the precise physical arrangement of the various components comprising the PG layer has been quite challenging to unravel using direct imaging techniques. Though some studies had suggested a scaffold model of PG layer [41], with the glycan strands arranged perpendicular to the cell surface, more recent experimental

studies using electron cryo-tomography (ECT) on purified sacculi of *E.coli* have revealed that the arrangement of the peptidoglycan in the cell wall consists of a single layered, planar network with glycan strands oriented in the circumferential direction [42] .

Two important design features of the PG mesh are the distribution of the lengths of the circumferentially oriented glycan strands and the degree of cross-linking of the peptide stems, which refers to the proportion of the peptide stems in PG layer that are cross-linked. In the first case, it is interesting to note that the glycan strands do not span the entire circumference of the rod shaped bacteria but are usually much shorter in length. In fact, it has been shown, using high performance liquid chromatography (HPLC), that the average length of all the glycan strands in the murein sacculus is ~ 21 disaccharide units, while for around 70% of the glycan strands, their length distribution has an even lower average value of ~ 8.9 disaccharide units, highlighting the substantial presence of short length glycan strands in the PG mesh of *E.coli* [11]. For the second case, it has been deduced that peptide stems rotate around the glycan backbone by roughly 90° per disaccharide unit, from which it can be concluded that only around 50% of the peptide stems remain in the same plane as the PG layer and are therefore available for cross-linking, with the degree of crosslinking in case of *E.coli* having been typically observed to be around 30% [10, 13].

It is notable that the PG layer undergoes steady remodeling during cell growth. In *E.coli*, nascent glycan strands are synthesised and then inserted into the PG layer using enzymes that reside in the inner membrane [5]. However, for appropriate incorporation of these new glycan strands into the PG network, existing peptide cross-links need to cleaved. This task is carried out by the action of hydrolytic enzymes or hydrolases, referred to as endopeptidases [43, 44]. This is particularly remarkable since the PG layer is under high turgor pressure and hence, it is necessary

that cleaving of existing cross-links is carried out in a carefully coordinated manner, ensuring that the PG mesh is robust enough to ensure cell viability at all times. This process is yet to be unravelled completely, though several models have been proposed, for instance the "make before break" model [33], which hypothesizes that new PG material is inserted into the PG mesh before the bonds connecting older material in the mesh are cleaved and ejected out. In accordance with this, a "three for one" growth model has been proposed for case of the single layer peptidoglycan in *E.coli* [13], in which an old glycan strand is replaced by three new glycan strands, with the new strands initially being crosslinked to the strands adjacent to the old one, which is then cleaved off by the action of hydrolytic enzymes and the three new glycan strands are inserted in its place. It is pertinent to note that the processes of synthesis of nascent PG material and its incorporation into the PG layer, on one hand and the process of cleaving off and removal of older PG material by the action of hydrolases, on the other hand, are crucial to the survival of the cell, with inhibition of either process leading to rapid cell lysis [5, 45]. Indeed, β-lactam antibiotics kill bacteria by inhibiting the incorporation of newer PG material into the existing PG mesh [35, 46].

MreB cytoskeleton

An important feature of the cells of several species of bacteria is the actin homologue MreB cytoskeleton [8, 47]. It plays an important role in the growth of the cell and in maintenance of the shape in rod shaped bacteria like *E.coli* [48, 49]. Treating *E.coli* cells with the MreB disrupting antibiotic A22 results in the distortion of their cylindrical uniformity. After washout however, MreB filaments reassemble, and rod shape of the cells is slowly recovered, underlining the importance of MreB in ensuring the ability of the cell to maintain its shape [50]. Several early papers suggested, based on *in vivo* observations, that MreB formed as a cell spanning

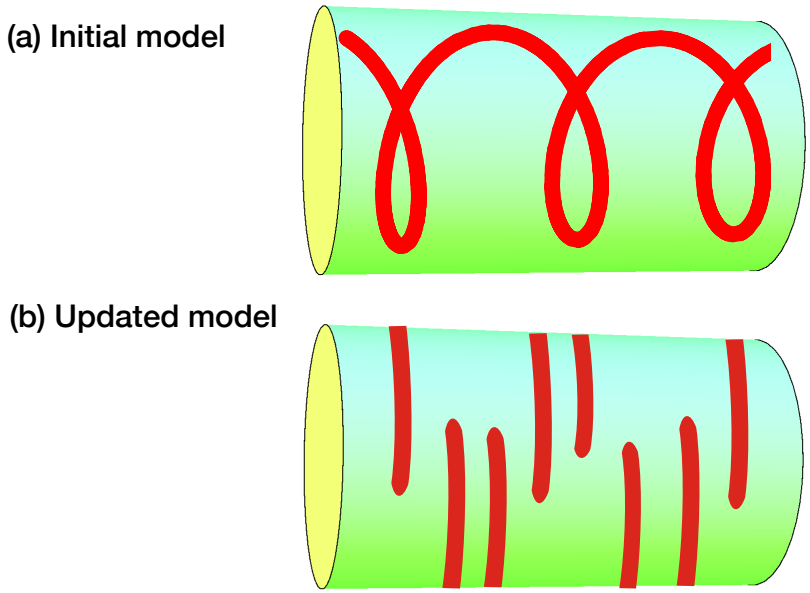

Figure 1.4: Models of MreB cytoskeleton *in vivo*. (a) Initial studies reported MreB polymers formed as cell spanning helix in rod shaped cells. (b) Newer experiments have established that MreB forms disconnected filament assemblies, aligned in the hoop direction of rod shaped cells.

helix [47, 51] (Fig. 1.4(a)). However, more recent studies, using high resolution light micropscopy, have invalidated this model and have established that MreB forms disconnected assemblies in the cell that move processively in the hoop direction of rod shaped cells[52, 53, 54] (Fig. 1.4(b)). The *in vivo* ultrastructure of MreB remains to be unravelled, however it has been observed *in vitro* that MreB forms bundles in solutions [55] and binds as filaments to membranes [56]. It is notable that studies have suggested that MreB may contribute to cell stiffness and is rigidly linked to the cell wall, with this composite structure possibly acting to suppress the onset of instability during growth of rod-shaped cells [6, 50].

Key question: How does the molecular level architecture of the PG mesh determines its material properties and protects it from mechanical failure?

The molecular level architecture of the PG mesh displays an array of design features, including length distribution of the glycan chains, degree of cross-linking and appropriate placement of the peptide cross-linkers along the glycan backbone, whose relevance in determining the bulk material properties of the cell wall remains to be fully explored and elucidated. The PG mesh faces a variety of mechanical requirements from its structure- it needs to be stiff enough to bear the high turgor pressure, elastic enough to allow for cell growth and tough enough to protect the cell from mechanical failure due to crack propagation. For a given material, stiffness refers to its ability to bear loads without large deformations while toughness refers to its resistance to crack propagation (which in this thesis we will quantify by calculating the tearing energy and the critical crack length, formally defined in Chapter 2). Perhaps the most vexing problem in engineering materials is to simultaneously ensure that the material is stiff, ensuring the ability to bear loads without large deformations and tough, ensuring that material can effectively resist crack propagation under loading, since these two requirements are typically conflicting [57]. In this regard, nature has proved itself as the "best engineer" with naturally occuring biomaterials like wood, bone, nacre, etc exhibiting structures that show remarkable orders of stiffness to resist high tension forces while being sufficient tough to prevent failure due to cracking [58, 59, 60]. Unravelling the ultrastructure of such materials has led to deep insights into the way their mechanical properties is underpinned by their molecular scale architecture. For the peptidoglycan mesh of the bacterial cell wall, a variety of methods have been developed to understand and measure its stiffness. For instance, Gumbart et al. [9] developed an all-atom model of the PG mesh of *E.coli* and by varying the glycan strand length and measuring the elastic modulus

under loading, were able to show that the elastic modulus along the hoop direction increases with increase in average glycan strand length. Tuson et al. [61] encapsulated bacteria cells in agarose of defined stiffness and by measuring the growth rate of cells combined with theoretical modelling, were able to extract the longitudinal elastic modulus of the cell and study the effect of MreB depolymerization on it. On the other hand, the structural components of the bacterial cell wall which underpin its toughness remains to be elucidated. Such studies have been carried out for several other naturally occurring materials. For instance, in case of nacre, it has been shown that its high order of toughness is a result of the presence of long molecules with folded or looped domains, as deduced by using Atomic Force Microscopy (AFM) to stretch the molecules exposed on the surface of freshly cleaved nacre, with the fibers elongating in a stepwise manner as the folded domains unfolded, giving rise to a saw-tooth shaped force-extension curve [62]. **In this thesis, we study the molecular scale design of the PG mesh of *E.coli* to understand its role in determining its bulk material properties. In particular, we explore the effect of short length glycan strands, degree of cross-linking and peptide cross-linking at the termini of glycan strands in enhancing the toughness of the PG mesh. We also investigate the effect that variability in the elastic properties of the molecular components of the PG mesh, specifically the peptide cross-linkers, have on its bulk mechanical response.**

1.3 Cytoplasmic cell membrane

The cell membrane, variously referred to as the cytoplasmic membrane or plasma membrane or the inner membrane, of bacterial cells is a phospholipid bilayer. Phospholipids, which contain phospate, are dominant components of all lipid membranes. In general, phospholipids are amphipathic, meaning they have both hydrophilic and hydrophobic parts- one end of these lipids contains a hydrophilic head group and

at the other end there are two hydrophobic tails. Phospholipids are an important functional entity of cell membranes in particular and indeed, of life in general, with their amphipathic nature leading to the formation of a wide range of self-assembled structures when exposed to water or aqueous solution. The driving force for such self-assembly is the hydrophobic nature of the lipid tails whereas the stability of the structure is anchored by the polar headgroups. Arguably, the most important such structural self assembly in biological cells is the formation of lipid bilayers, which are two-layered structures with the hydrophilic heads of the lipids facing outwards, contacting the aqueous fluid both inside and outside the cell while the neutral, long, hydrophobic tails are driven inward and point towards one another to avoid interactions with the polar aqueous environment. Such lipid bilayers form the structural basis of all cell membranes, making an excellent barrier between the inner and outer parts of the cell, being nearly impermeable for ions and most polar molecules due to the presence of the hydrophobic core. Lipid membranes also contain transport systems necessary to facilitate the transfer of nutrients into the cell and waste products out of the cell [63]. Further, in case of the prokaryotic bacterial cells, which lack intracellular organelles, all the membrane associated functions of eukaryotic cell organelles are performed in the cell membrane [31].

Structure of cell membrane

Lipid bilayers, which form the basic structural unit of the cell membrane, were first recognized by Gorten and Grendel in 1925 for mammalian red blood cells [65]. However, the structure of the cell membranes remained unclear and it was only in 1972 that the most accepted model of cell plasma membranes, the "fluid mosaic model", was proposed by Singer and Nicholson [66], in which, the membrane is interpreted as a two-dimensional fluid composed of oriented lipids and globular proteins (Fig. 1.5). The lipid molecules, in particular phospholipids, can move freely in the plane of the

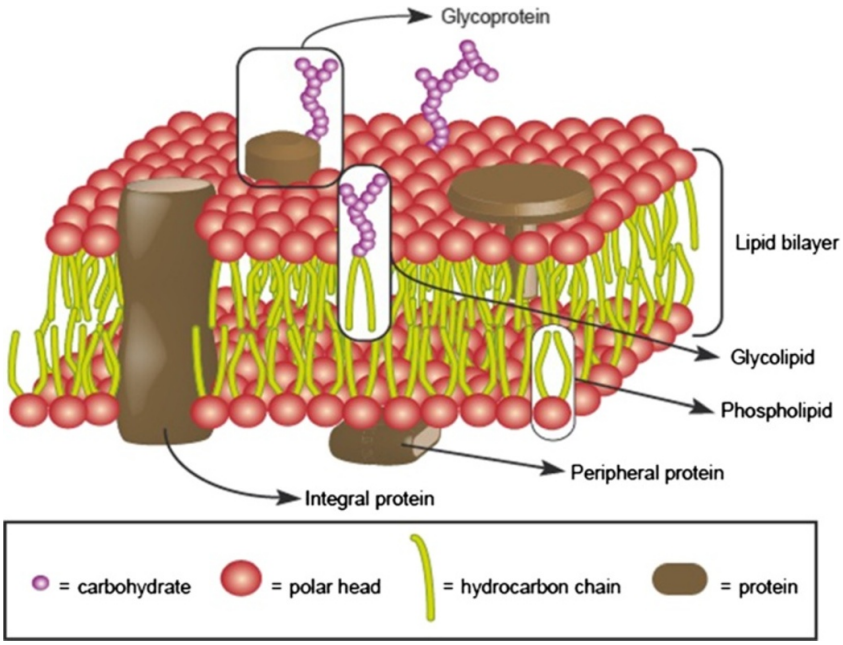

Figure 1.5: Schematic representation of the fluid mosaic model of the cell membrane. Figure is reproduced from Ref. [64] under Creative Commons CC BY 4.0.

bilayer, while membrane proteins that are embedded in the lipid bilayer can diffuse laterally in the lipid matrix unless restricted by special interactions. This simple model has been able to give a good qualitative understanding of several fundamental features of the cell membrane, in particular highlighting the importance of hydrophobic interactions which form the thermodynamic key for the formation and stability of biological membranes and their interaction with membrane proteins. However, the model is not adequate to explain various complex interactions and functions of the cell membrane, which include specialized roles of membrane domains, microstructure of cell membrane, and generally, understanding the lipid-protein and lipid-lipid interactions. Nevertheless, the fluid mosaic model has served as the foundation for subsequently developed updated models [67]. Recent advances in computation have made possible to model realistic biological membranes, focussing on lipid composition. In this thesis, we focus on the atomistic computational model of bacterial cell membrane, details of the model will be described in section 4.4.

In case of *E.coli*, the primary components constituting the lipid bilayer are zwitte-

rionic phosphatidyl ethanolamine (PE) and anionic phosphatidyl glycerol (PG). In this case, the composition is about $70-80\%$ PE, $20-25\%$ PG and lesser amounts of cardiolipin, phosphatidyl serine and other minor lipids [31, 68, 69]. In sharp contrast, the concentrations of lipids PE and PG in mammalian cell membranes are much lower. For instance, in blood cells, the concentrations of lipids PE and PG are around 6% and 2% of all the phospolipids in the membrane [70]. In fact, the major phospolipid component of mammalian cell membranes is phosphatidyl choline (PC) [70], which is rarely present in bacterial cell membranes [68]. This difference in the composition of bacterial cell membranes and mammalian cell membranes makes the cell membrane an apt target for antimicrobial agents, which can selectively attack and destroy bacterial cells in an effective manner (see Fig. 1.6).

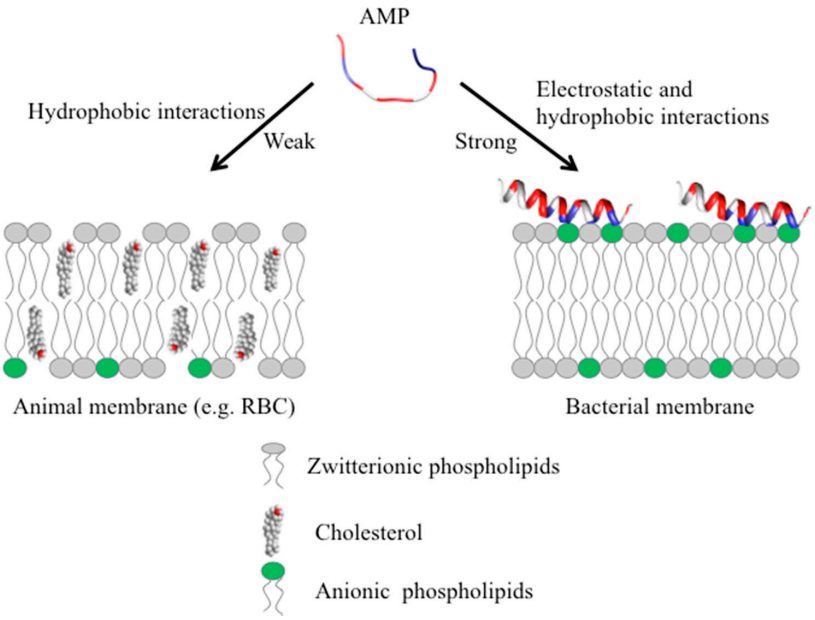

Figure 1.6: Interaction of cationic AMPs at the surface of the mammalian red blood cell (RBC) membrane (left) and bacterial cell membrane (right). The presence of negatively charged head groups (PG lipids) in the outer leaflet of bacterial cell membranes, leading to strong electrostatic interactions with the positively charged AMPs. On the other hand, the outer leaflets of the mammalian cell membranes are primarily composed of zwitterionic phospolipids (e.g. PC) and other neutral components like cholestrol. Figure reproduced from Ref. [71].

1.3.1 Antimicrobial action on bacterial cell membrane

Antimicrobial agents are natural or synthetic medications that are used to treat infections caused by a variety of pathogens (e.g., virus, fungi, bacteria, parasites). It is vital that these agents have the ability to selectively kill microbial cells without gravely affecting host cells like mammalian cells. For a long time, antibiotics have been the most effective defence against infections caused by bacterial cells. However, the emergence and rapid spread of bacteria that are resistant to antibiotic treatment, combined with lack of new antibiotics, has posed a serious concern for public health, necessitating the development of alternate therapeutic agents that do not induce significant resistance in bacteria. Since 1980s, antimicrobial peptides (AMPs) have been identified as an answer to this riddle [72, 73].

Antimicrobial peptides

Antimicrobial peptides (AMPs), also known as host defense peptides, are components of the innate immune system of eukaryotes which can kill infecting bacteria, without harming the host cells and without inducing significant resistance in bacteria [74, 75, 76]. Typically, they are small cationic, amphipathic peptides that are biologically active compounds, and are now known to exist in all multicellular organisms [72]. An early discovery of an AMP was that of Magainin-2, isolated from the African clawed frog *Xenopus laevis* [77]. Thousands of other AMPs have since been discovered. AMPs are commonly classified based on their secondary structures [78, 79, 80], which include α-helices (e.g. LL37), β-sheets (e.g. Protegrin-1), mixed α/β structure (e.g. human β defensin 2) or extended random structure (e.g. Indolicidin) (see Fig. 1.7).

The physiochemical makeup of the wide variety of AMPs has some interesting common features- they are relatively short chained peptides consisting of 5-50 amino

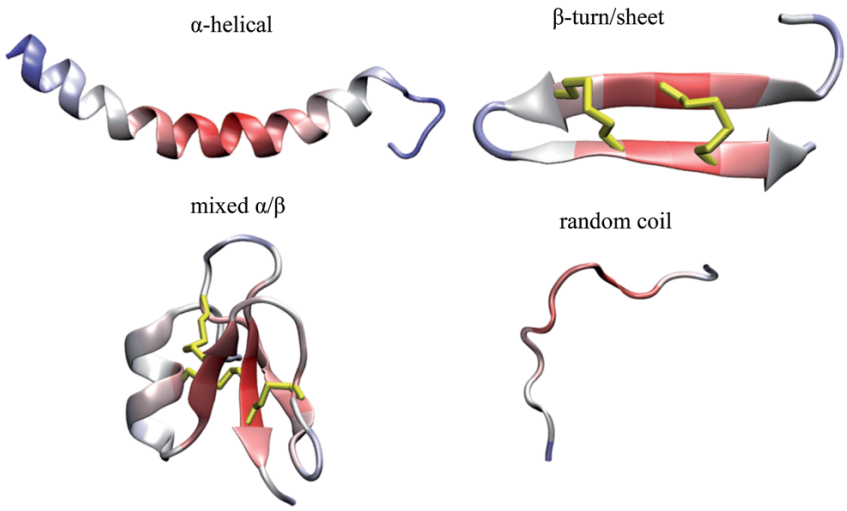

Figure 1.7: Secondary structures of AMPs- the α helical LL37, $\beta-$sheet of Protegrin-1, mixed α/β structure of human β defensin 2 and extended coil structure of Indolicidin. Disulphide bonds, which cross-link different regions of the AMPs and act to stabilize peptide conformations, are depicted as yellow sticks. Most $\alpha-$helical and random AMPs lack disulphide bonds, while many $\beta-$turn/sheet and mixed α/β AMPs exhibit disulphide bonds. Figure reproduced from Ref. [81] with permission of Royal Society of Chemistry ; permission conveyed through Copyright Clearance Center, Inc.

acid sequences having cationic residues with net charge +2 to +9 and exhibiting significant presence of hydrophobic residues [19, 82]. The key question is to understand the mechanism of antimicrobial action of such AMPs and the role of factors such as their size, charge, hydrophobicity, in it.

Mechanism of action of AMPs

AMPs are considered as one of the most promising candidates for fighting pathogens due to their broad range of activity and limited toxicity to the host cells [73]. The action of cationic AMPs on cell membranes has been well described by membrane permeabilization [83], where the cationic peptides bind and interact with the negatively charged lipids in the bacterial membranes, leading to the formation of tran-

sient pores on the membrane which cause considerable conformational changes in their structure while also inducing structural reorganization of the membrane lipids, ultimately leading to disruption of membrane integrity and cell death [84, 85, 86]. In addition, recent studies have also shown that AMPs could act by translocating across the outer cell membrane and affecting several essential processes like altering cytoplasmic-membrane, septum formation, inhibiting cell-wall synthesis, protein synthesis or enzymatic activity, all of which can cause cell death [87]. Of all these known mechanisms, the plasma membrane-disrupting ability of these peptides has attracted the most interest. Initial accummulation of the AMPs at the membrane surface is driven by the significant presence of negatively charged lipid head groups (e.g. PG lipids), leading to strong electrostatic interactions, as well as by hydrophobic interactions (Fig. 1.6 and Fig. 1.8(a)). Several models have been proposed to describe the membrane disrupting action of AMPs that occurs thereafter, for instance, transmembrane pore forming models like "barrel-stave" and "toroidal-pore" models and non - pore forming models which include "carpet" model and "detergent"-like model [87, 88]. We now briefly describe these models- in the barrel-stave model, the initial orientation of the AMPs is parallel to the membrane surface, but subsequent penetration and insertion towards the membrane core occurs in a perpendicular orientation (Fig. 1.8(b)), which promotes lateral peptide-peptide interactions. In this case, amphipathic structure of the peptide plays a necessary and essential role in the pore formation mechanism, with the hydrophobic regions of the peptide interacting with the membrane lipids and the hydrophilic regions facing the lumen of the pore. In the toroidal pore model, the peptide again insert towards the membrane core perpendicular to the plane of the bilayer, with the hydrophilic regions of the peptides interacting with the lipid head groups and the hydrophobic regions penetrating into the hydrophobic core of the bilayer (Fig. 1.8(c)). In the process, the peptides induce a local inward curvature of the membrane, resulting in the lining of the pore by lipid molecules as well. In both cases, of the barrel stave model and the toroidal pore

model, the formation of such pores results eventually in membrane depolarization and subsequently, cell death. However, AMPs can act without forming pores in the

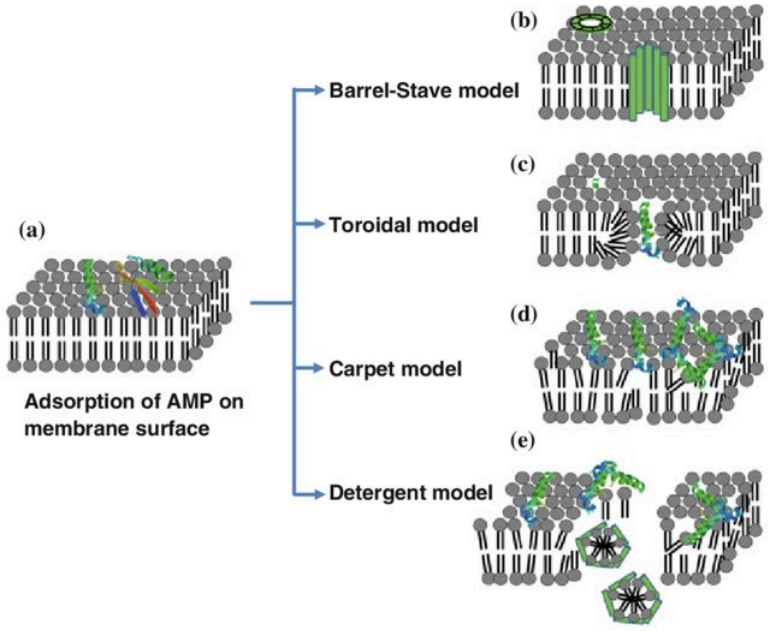

Figure 1.8: A cartoon illustrating various models of antimicrobial peptides (AMPs) action on cell membranes. After initial binding of AMP on the membrane surface (a), membrane disruption can be either through transmembrane pore formation (b,c), or other possible mechanisms (d,e). Figure reproduced from Ref. [89] with permission of Springer Nature ; permission conveyed through Copyright Clearance Center, Inc.

membrane structure- one such model is the carpet model, in which the peptides aggregate and adsorb parallel to the lipid bilayer, covering local areas of the membrane surface akin to a "carpet" (Fig. 1.8(d)). Beyond a given threshold concentration, the peptides cause unfavourable interactions on the membrane surface by rotating and thereby redirecting phospholipids bound to them. Consequently, this results in a detergent-like activity, which eventually disintegrates the membrane by forming micelles. This ultimate disintegration of the membrane structure into micelles is also known as the detergent-like model (Fig. 1.8(e)).

It is notable that the outer surfaces of Gram-positive and Gram-negative bacteria, which are substantially different in nature, need to be crossed by AMPs to access cell membrane and interior of the cell. In case of the Gram positive cell wall, the

outer surface is the thick peptidoglycan mesh, which most AMPs seem to cross fairly easily, taking advantage of its mesh like structure [90]. For Gram negative bacteria, the outer membrane, presents a different sort of surface interaction for attacking AMPs and in this case, several AMPs are able to cross it by a charge exchange mechanism [91]. These peptides can then traverse the thin PG network in this case to gain access to the cell membrane.

Nonetheless, despite their great importance and distinct advantages over antibiotics, creating therapies with AMPs is not unproblematic and exhibit drawbacks, including their high cost of manufacturing and lack of synthetic scalability, hampered by limited bioavailability and susceptibility to degradation due to proteolysis. These issues have thus far limited their clinical usage [36].

1.4 Biomimetic antimicrobial polymers

To overcome the issues limiting therapeutic use of antimicrobial peptides, one promising direction explored in recent years has been the designing of synthetic mimics of AMPs. Perhaps the most unique feature of AMPs is that the molecular mechanism of their antimicrobial action is independent of specific receptors or specific protein-protein interactions [92]. Further, though AMPs are relatively small structurally and exhibit similar physiochemical features of net positive charge and hydrophobic side chains, yet no common sequence or arrangement of the constituent functional residues has been found. These findings suggest that an appropriate "balance" between the various functional groups, particularly the cationic and hydrophobic residues, is a key attribute of the antimicrobial action of AMPs, rather than their exact amino acid sequence and secondary structural conformation. This motivated the first steps to create polymer mimcs of AMPs or AMPolys, minimally composed of charged cationic and hydrophobic functionalities. Typically, AMPolys

are made in agreement with physical characteristics of AMPs like low molecular weight with short chain lengths and similar cationic charge. Examples of synthetic antimicrobial polymers include those based on methacrylate [93], norbornene [94], nylon [95], vinyl ether [96] and alternating ring-opening metathesis polymerization (ROMP) copolymers [97] (see Fig. 1.9). Design of such polymers for biomedical utility, however, requires not only comparable activity to AMPs, but also good levels of specificity, in other words, their ability to selectively kill bacteria over human cells, as well [19, 92, 98, 99]. Extensive modulation of the structural design of AMPolys has been attempted to ensure optimal levels of antimicrobial action and specificity. These include controlling their composition and length, sequencing of functional groups along the polymer backbone, percentage of constituent hydrophobic and cationic groups, molecular weight of the polymer chain, all of which can have an effect on the antimicrobial efficacy and selectivity of action of AMPolys [100, 101]. In summary, appropriately designed biomimetic polymers exhibit significant potential as thepareutic agents that can be used as replacements for AMPs, as they can be cost-effective with great scalability, with the advantage to easily tune the chemical composition and distribution of groups along the polymer chain to ensure optimal levels of antimicrobial action and specificity.

Key question: How to design AM polymers that even more effectively mimic the evolutionarily optimized design of natural AMPs?

Studies on AMP-mimic polymers have largely focussed on polymers have a binary composition, constituting of cationic and hydrophobic moieties, as these functionalities have been thought to be the minimum requirements for the bactericidal activity [16, 18, 102, 103]. The design of such binary polymers is simple; however, it is difficult to simultaneously optimize the composition of the constituent functional groups for ensuring potent antibacterial activity and reasonable selectivity. The

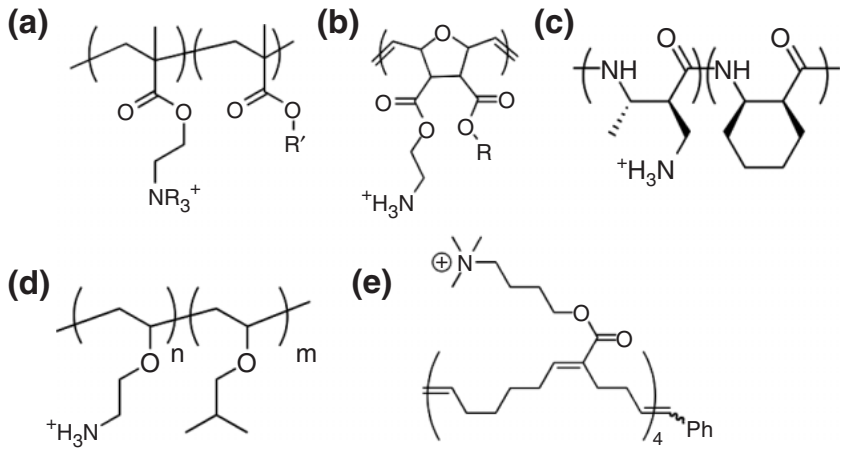

Figure 1.9: Examples of AMP-mimetic antimicrobial polymers includes those based on (a) methacrylate, (b) norbornene, (c) nylon, (d) vinyl ether, (e) alternating ring-opening metathesis polymerization (ROMP) copolymers. Figure reproduced from Ref. [92] with permission of John Wiley and Sons ; permission conveyed through Copyright Clearance Center, Inc.

coupling of cationic and hydrophobic monomer units in the binary systems restrict the independent control of electrostatic and hydrophobic insertion of polymers into membranes. Indeed, naturally occuring AMPs are not just binarily composed of hydrophobic and cationic functionalities, rather they are typically constituted of a multitude of functional amino acids [19, 104]. In this context, it is notable that in general, neutral polar residues are one of the most common constituents of natural AMPs [19]. Further, while AMPs generally display an overall positive charge, many of them, including defensin, magainin, LL-37, have anionic amino acids in their sequences [20, 105, 106]. This inspires the following natural question- What role do such neutral polar or anionic amino acids play in the antimicrobial action of AMPs and do they possess some unique functional characteristics relevant for biomimicry? **In this thesis, we use detailed atomistic molecular dynamics (MD) simulations to study ternary biomimetic polymers, constituting of additional functionalities, apart from the cationic and hydrophobic functionalities.**

A key purpose for this is to implement insights from the evolutionarily optimized design of AMPs, in which presence of such additional functionalities is extremely common, to the molecular design of AM polymers, that have been missing in the traditional binary polymer approach, which can ultimately help in optimizing the efficacy of AM polymers by improving their antimicrobial activity and selectivity.

1.5 Summary and thesis outline

This thesis is divided into two parts. In the first part, aspects of the molecular scale architecture of the peptidoglycan (PG) mesh and their effect on its material properties are explored, utilizing theoretical methods. The effect of variability in the elastic properties of the peptide cross-linkers of the PG mesh on its bulk mechanical response is also investigated, utilizing theoretical methods and computer simulations. In the second part of the thesis, we study the conformational landscape, aggregation dynamics and interactions with model bacterial membrane of biomimetic antimicrobial polymers (AMPolys),utilizing detailed atomistic molecular dynamics simulations. The role played by neutral polar groups and appropriate sequencing of the functional moieties along the polymer backbone in influencing the aggregation dynamics of such polymers and their membrane-interactions is studied in depth, utilizing detailed atomistic molecular dynamics simulations. Further, we also investigate the conformational landscape of AMPolys that have anionic functional groups as constituents, with particular focus on probing the formation of salt bridges and their role in determining the conformational dynamics of such polymers.

The rest of this thesis is organized as follows:

In Chapter 2, we explore the role of various design features of the cell in enhancing the toughness of the cell wall. We explain how the glycan strand length distribution, the degree of cross-linking and the placement of the cross-links on the glycan

strands can act in tandem to ensure that the cell wall offers sufficient resistance to propagation of cracks. Further, we suggest a possible mechanism by which peptide bond hydrolysis, via judicious cleaving of peptide cross-links, can act to mitigate this risk of failure. We also study the reinforcing effect of MreB cytoskeleton, which can offer a degree of safety to the cell wall. However, we show that the cross-linked structure of the cell wall is its primary line of defense against mechanical failure. This chapter is based on work published in Ref. [107].

In Chapter 3, motivated by the question of understanding the effect of variability in the material properties of the peptide crosslinkers on the bulk mechanical properties of the cell wall structure of bacteria, we study a spring system in which variability is encoded by assigning values of spring constants and rupture strengths of the constituent springs from appropriate probability distribution. Using analytical methods and computer simulations, we study the response of the spring system to shear loading and observe how heterogeneities inherent in the system can heighten the resistance to failure. We derive the force extension relation of the system and explore the effect that the disorder in values of spring constant and rupture strength has on load carrying capacity of the system and failure displacement. We also study a discrete step shear loading of the system, exhibiting a transition from quasibrittle to brittle response controlled by the step size, providing a possible framework to experimentally quantify the disorder in analogous structures. This chapter is based on work published in Ref. [108].

In Chapter 4, we provide a summary of the molecular dynamics (MD) simulation technique. We describe the bonded and non-bonded interactions between the constituent atoms, boundary conditions, ensembles and computational models relevant to this thesis.

In Chapter 5, we explore the conformational landscape of aggregates formed in solution phase by ternary biomimetic antimicrobial methacrylate polymers, composed of

hydrophobic, charged cationic and polar functional groups and compare it with aggregate morphologies of binary methacrylate polymers, composed only of hydrophobic and charged cationic functional groups. The effect of sequence of the constituent functional groups on aggregate conformation is also studied by considering random and block sequences along the polymer backbone. We show that while binary polymers tend to form robust aggregates, replacing some of the hydrophobic groups with overall charge neutral polar groups weakens the aggregate considerably, leading to increased conformational fluctuations and formation of loose-packed, open aggregates, particularly in the case of random ternary polymers. This chapter is based on work done in Ref. [109].

In Chapter 6, we consider ternary biomimetic antimicrobial polymers that are composed of hydrophobic, cationic and anionic functional groups. We explore the effect of inclusion of the anionic groups in determining the conformational landscape of such polymers in solution phase. We specifically focus on investigating the formation and lifetime of salt bridges between pairs of oppositely charged cationic and anionic moieties and the effect of such interactions on specific conformations of the polymer in solution phase. Our results show that salt bridges act as transient cross-linkers, which affect polymer conformation and lead to a dynamic switching between compact and extended conformations. This chapter is based on work done in Ref. [110].

In Chapter 7, we study the interaction of methacrylate ternary polymers, composed of charged, hydrophobic and polar groups in random configuration as well as in block arrangement of polar groups, with the bacterial model membrane and compare it with the membrane interaction of traditional binary polymers, consisting only of charged and hydrophobic groups. We show that ternary polymers can penetrate deep into the membrane, with even a single polymer having a marked affect on the membrane structure, inducing extensive lipid reorganisation in its vicinity. We also investigate in detail the membrane insertion modes of the ternary polymer models,

showing that in this case, a clear segregation of constituent functional groups is absent, unlike the case binary polymers. Finally, we examine membrane interactions of aggregates of binary and ternary polymers, exhibiting that weak ternary aggregates undergo rapid partitioning and subsequently, insertion into membrane interior, while such polymer partitioning is constrained for the stronger binary aggregates. This chapter is based on work done in Ref. [111].

Chapter 2

Safeguarding the bacterial cell wall against mechanical failure

2.1 Introduction

For the bacterial cell wall, which is constituted primarily of the peptidoglycan mesh, it is imperative to be stiff enough to bear the high turgor pressure and maintain shape as well as being adequately tough, so as to resist mechanical failure due to crack propagation. While the stiffness of the bacterial cell wall has been well studied [6, 7, 44, 112], our aim here is to understand its toughness, or resistance to propagation of cracks, an immensely desirable materials property [57]. The cell wall, which is under high turgor pressure, can have cracks on its surface as a consequence of its design [113], and these can play an important role in ensuring passage of nutrients and waste products through the peptidoglycan layer. In fact, permeability of cell walls of bacteria has been much studied [114, 115, 116] and pores of size as large as 10 nm in diameter have also been observed [117]. On the other hand, in bacteria like *Staphylococcus aureus*, mechanical crack propagation has been shown to drive daughter cell separation [118], which indicates that bacterial cells are adapted

to be able to tune mechanical failure modes. However, the relation of the molecular level architecture of the cell wall to its toughness remained to be elucidated. Use of mechanical modelling of the cell wall is particularly relevant in this context since such studies have led to remarkable insights into the structure of the cell wall. For instance, Huang et al. [119] developed a simple elastic model for the Gram-negative cell wall to gain insight into the mechanical response of cell shape to cell wall damage. Jiang and Sun [120] utilized a theoretical mechanochemical approach to describe the interplay of cell wall growth, mechanics, and cytoskeletal filaments in shaping the bacterial cell. Nguyen et al. [121] studied a coarse grained model of the cell wall to explore the remodelling of peptidoglycan during growth of the cell wall and highlighted the process by which local coordination of the enzymes can introduce new material into an existing unilayer PG network, while maintaining cell wall integrity and rod shape.

In this chapter, we examine the role of various design components of the cell in securing the cell wall against mechanical failure. In particular, we explore the role of the geometry of the cell, the cross-linked polymeric structure of the cell wall and the role of the MreB cytoskeleton in ensuring sufficient resistance to propagation of cracks. Our model studies the Gram-negative rod-shaped bacteria (e.g. *Escherichia coli*), with a single layer of the peptidoglycan mesh. In short time scales relevant to the problem, the behavior of the cell wall is perfectly elastic [122, 123]. As noted in section 1.2, the peptidoglycan mesh in this case consists of glycan strands oriented in the circumferential direction, cross-linked intermittently by peptide bonds. Modelling the cell both as an elastic plate and cylindrical shell, we estimate the critical crack lengths under stress due to turgor pressure. We show that cross-linking is crucial for maintaining the integrity of the cell wall, since the minimum energy needed for crack propagation, called the tearing energy, is largely controlled by the degree of cross-linking. We exhibit the important role that appropriately cross-linked shorter length glycan strands can play in enhancing the tearing energy, which gives an ex-

planation of striking experimental observations on the extensive presence of short length glycan strands in the peptidoglycan mesh [11] and the strong propensity of the glycan strands to be cross-linked at the terminating units [10, 12]. We also analyse how peptide bond hydrolysis can be used by the cell as a defence mechanism against cracking, exhibiting that such hydrolysis can act to increase the tearing energy. Finally, we probe the role of the MreB cytoskeleton which can promote cell wall toughness by exerting an inward directed pressure countering the turgor pressure. Our results indicate that the cross-linked structure of the cell wall plays the more important role in safeguarding the cell against failure due to crack propagation. This chapter is based on work published in reference [107].

2.2 Cell Wall as pressurized shell

To model the bacterial cell, we employ thin shell theory. Thin elastic shells are elastic bodies whose thickness is small compared to their other dimensions, so effectively they can be treated as two-dimensional elastic bodies and whose natural configuration is non flat, therefore their analysis necessitates a deeper appreciation of geometry. Analysis of deformations of thin shells and their elastic energy dates back to Rayleigh [124] who recognised that their elastic energy will in general involve both stretching and bending energies. Since then shell theory has been extensively developed [125]. Further, shell theory has also been instrumental in the study of mechanobiology of cells, allowing for an apt model to probe cellular geometry and its influence on biological processes. In case of bacteria, the application of shell theory to study such cells was pioneered by Koch [33] and has since been widely used to study bacterial cells in a wide variety of contexts [50, 61, 120, 126, 127].

We model the bacterial cell wall as a cylindrical thin shell, loaded with uniform internal pressure P, corresponding to the turgor pressure in the cell, as depicted in

Fig. 2.1. The radius of the shell is R and its thickness, h. Since h/R is small (relevant parameter values are listed in Table 2.1), we can treat the cell wall as effectively two dimensional, describing it by its central (neutral) surface. In particular, we will be using thin shell theory, with all moment expressions being neglected, in other words, we will be using "membrane theory" of thin shells [125]. We now want to derive the equilibrium equations for this system. More generally, we derive the equations of equilibrium for an axisymmetric Hookean shell loaded with uniform internal pressure P. The shell has uniform thickness denoted h and (not necessarily uniform) parallel radius denoted R.

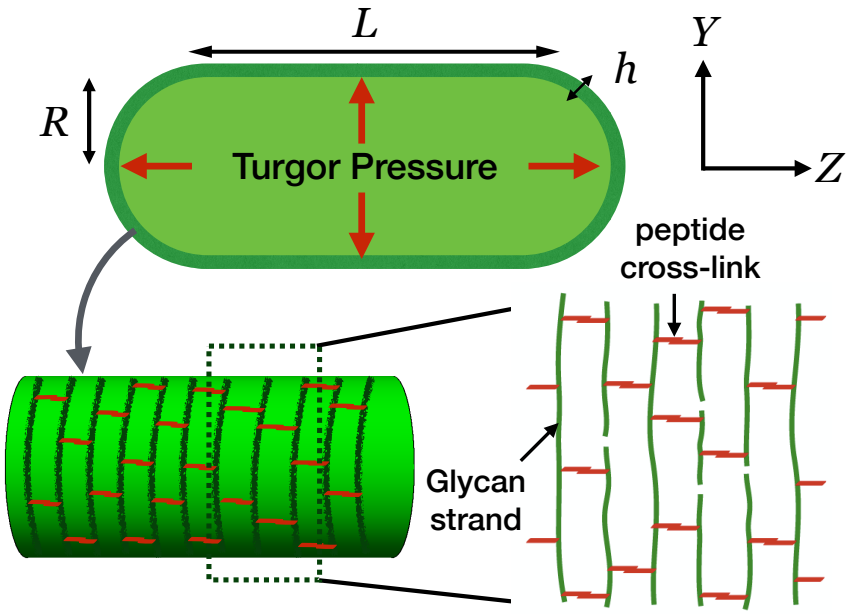

Figure 2.1: The bacterial cell wall modelled as a pressurised cylindrical shell of radius R, thickness h and with the length denoted L. Glycan strands of variable lengths, aligned on an average in the circumferential direction, are cross-linked intermittently by peptide bonds.

We first describe the geometry of surface of revolution, which is generated by rotating a given plane curve (called the meridian) around an axis lying in its plane. Intersecting planes perpendicular to axis of rotation with the surface gives circles, which are called parallels. The surface can thus be parametrized by coordinates (s, ϕ), where s denotes the arc length of the meridian curve (hence, it denotes the

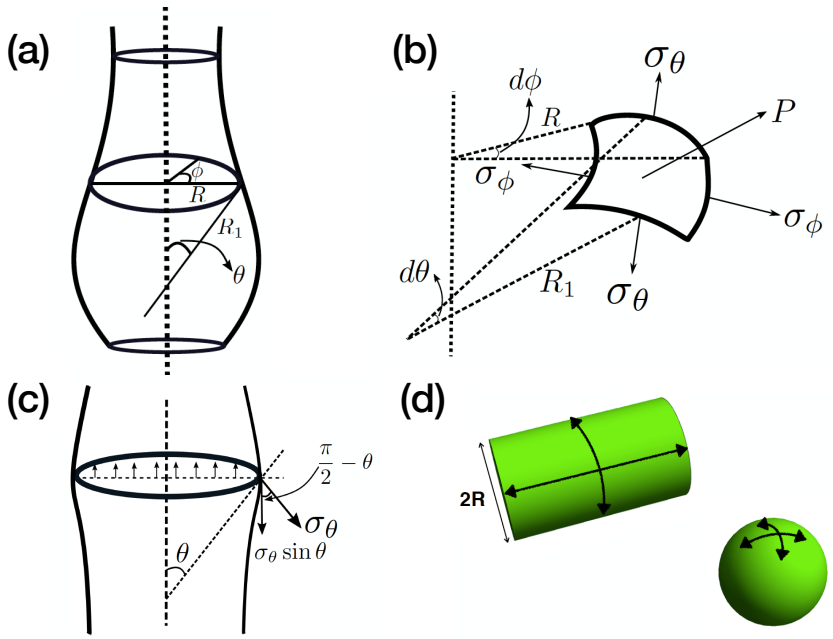

Figure 2.2: (a) Surface of revolution parameterized in spherical polar coordinates. (b) Force balance for forces acting in the surface normal direction. (c) Force balance for forces acting in the axial direction. (d) Principal axes for cylinder and sphere.

common distance of all points lying in the parallel, as measured along the meridian curve from its starting point), while the angle ϕ fixes the position of the point on the parallel (Fig. 2.2(a)). Since the coordinate s determines the parallel, the radius of the parallel R will also be a function of it. We also denote by θ the angle made by the normal to the surface at a given point with the axis of rotation. This surface of revolution gives the "middle surface" of the shell of revolution, which is then completely determined geometrically by the middle surface and by its thickness h.

To determine the equations of equilibrium, we utilize a force balance approach. Due to the assumption of thin shell and due to loading being a uniform internal pressure, we only need to consider the stresses σ_ϕ and σ_θ (Fig. 2.2(b)). The forces due to the internal pressure and due to the stress resultants must be in equilibrium at each point and in all directions. We fix a small patch on the middle surface. The radius of the associated parallel is R and the associated meridional radius of curvature is R_1 (which in other words is the radius of the circle that best fits the meridian curve as it passes through the surface patch). Then the area of the patch is $\approx (Rd\phi)(R_1 d\theta)$.

We first compute the force balance in the surface normal direction (Fig. 2.2(b)). Since the internal pressure is acting in the direction of the normal to the surface, thus the force exerted in the (outward) normal direction on the patch is given by $P(Rd\phi)(R_1 d\theta)$. The force exerted on the upper and lower parts of the patch due to the meridional stress σ_θ is given by $\sigma_\theta R d\phi h$ in either direction. Taking components of both these forces in the (inward) normal direction and summing them, we get that the force exerted in the (inward) normal direction, due to meridional stress, is given by $2\sigma_\theta h R d\phi \sin(\frac{d\theta}{2}) \approx \sigma_\theta h R d\phi d\theta$. Similarly, in the hoop direction, we have that the force exerted on either side of the patch is given by $\sigma_\phi h R_1 d\theta$ and the force then in the (inward) radial direction is got by summing the radial components of both the forces, and is equal to $\sigma_\phi h R_1 d\theta d\phi$. The component of this force in the (inward) normal direction is given by $\sigma_\phi h R_1 d\theta d\phi \sin\theta$ (Fig. 2.2(b)). Thus, we have by force balance in the normal direction,

$$\sigma_\phi h R_1 d\theta d\phi \sin\theta + \sigma_\theta h R d\phi d\theta = P(Rd\phi)(R_1 d\theta) \tag{2.1}$$

Dividing Equation 2.1 by the $RR_1 d\theta d\phi$, we get the so called "membrane equation"

$$\frac{\sigma_\phi \sin\theta}{R} + \frac{\sigma_\theta}{R_1} = \frac{P}{h} \tag{2.2}$$

Now, we do a similar force balance in the axial direction (Fig. 2.2(c)). The force exerted in the axial direction, due to the internal pressure, is simply $P\pi R^2$. This is countered by the force on the surface, exerted by the meridional stress σ_θ, whose component in the axial direction is given by $\sigma_\theta \sin\theta$. Thus, the force exerted is equal

to $2\pi Rh\sigma_\theta \sin\theta$. So, by force balance in the axial direction, we have

$$2\pi Rh\sigma_\theta \sin\theta = P\pi R^2 \tag{2.3}$$

and therefore, we have

$$\sigma_\theta = \frac{PR}{2h\sin\theta} \tag{2.4}$$

Plugging in this value of σ_θ in Equation 2.2, we get

$$\sigma_\phi = \frac{PR}{h\sin\theta}\left(1 - \frac{R}{2R_1\sin\theta}\right) \tag{2.5}$$

In the special case of a circular cylinder, of fixed radius R, we have $\theta = \pi/2$ and $1/R_1 = 0$, and so,

$$\sigma_\theta = PR/2h \tag{2.6}$$

and

$$\sigma_\phi = PR/h \tag{2.7}$$

In this case, we have that the meridional stress is along the axial direction and also the axial stress, which we denote σ_z. Note that a stress anisotropy exists in the cylindrical case, with $\sigma_\phi/\sigma_z = 2$.

2.3 Cell Wall Crack Energetics

The study of cracks, or fracture mechanics, while attempted in various ways in the 19th century, had its true genesis in the pioneering work of Griffith [128], who developed a energy balance criterion to study thin crack on a solid body under applied stresses. Since then fracture mechanics has been extensively studied, with the development of linear elastic fracture mechanics, elastic plastic fracture mechanics [58, 129] and more recently, application of modelling techniques like phase field modelling to study dynamic fracture [130].

We now analyse crack on the bacterial cell wall. Since stress in the hoop direction is twice the stress in the axial direction, longitudinal cracks are subject to a larger stress, as they are aligned perpendicular to the hoop direction. Indeed, cylindrical pressure vessels predominantly display longitudinal cracks, for this reason, including well known examples occurring in daily life like sausages and pipes cracking longitudinally [131]. For rod shaped bacteria, like *E.coli*, which is under high turgor pressure, a corresponding stress anisotropy indicates the possibility of similar failure due to cracking in the longitudinal direction. Our aim here is to understand the structural features of the cell wall which protect it from such failure along the axial direction. We model a crack on the cell wall in two ways: (1) by considering a centrally placed crack on an infinite plate, thus neglecting curvature effects, and (2) considering a longitudinally aligned crack on a pressurized shell, thus accounting for cell curvature. We assume for simplicity that the shell is isotropic with elastic modulus denoted E.

2.3.1 Elastic energy release

In the first case, we begin with a thin plate of thickness h placed in the $Y-Z$-plane, with a tensile load $\sigma = PR/h$ applied in the Y-direction. A crack of total length $2c$ is

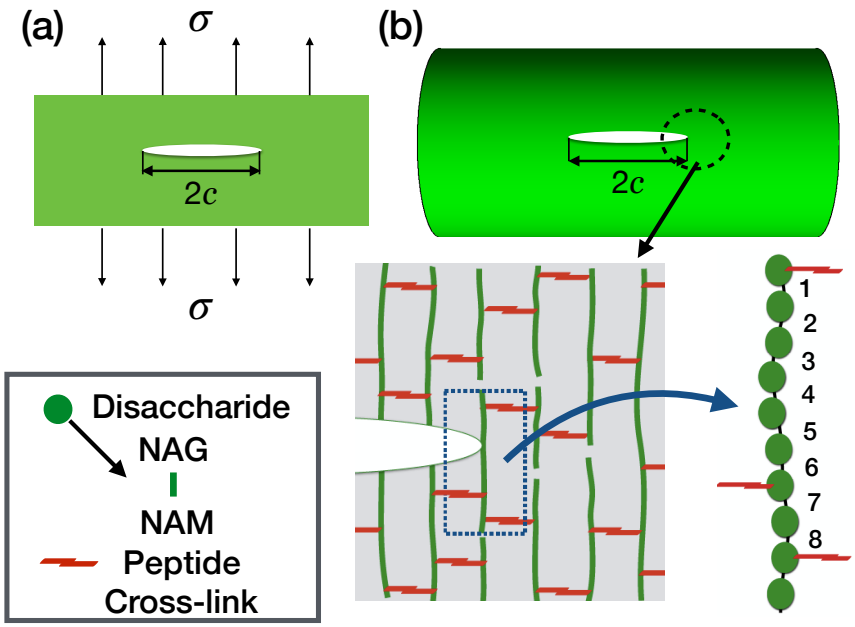

Figure 2.3: (a) A crack of length $2c$ on a thin plate of thickness h with a remote load σ acting on it, perpendicular to the line of crack. (b) A longitudinally aligned crack on the cell wall. Near the tip, the crack comes up against a glycan strand, here illustrated having a length of 10 disaccharide units, with average number of glycosidic bonds connecting the disaccharides between adjacent cross-links calculated as $n = 4$. Each disaccharide unit consists of alternating sugars NAG and NAM connected by a glycosidic bond. Note that the depiction of the peptidoglycan sacculus here is illustrative, in general, the meshwork might exhibit high amount of disorder.

introduced, along the Z-axis, as shown in Fig. 2.3(a). The crack lengths of interest to us are considerably smaller than the radius and length of the cell wall. We can thus treat the plate as infinite. To calculate the critical crack length, beyond which crack propagation becomes energetically favourable, we use an energy balance criterion, studied by Griffith [128] which compares the energy required to break atomic bonds, thus leading to new surfaces, to the strain energy released as the crack enlarges. To formally state our case again, we have a centrally placed thin crack of length $2c$ in the infinite plate with uniform thickness h, with the plate represented by $Y - Z$ plane. The crack is placed on the Z-axis, aligned in the Z-direction with the middle point of the crack at the origin and a remote load σ applied in the positive and negative Y-direction. When an increment in the length of the crack occurs, there is a release of strain energy and crack propagation becomes energetically favourable

when this release of strain energy, due to increment in crack length, is greater than the surface energy which is needed to break the bonds of the specimen. The critical point is reached when both are balanced, which we write mathematically as

$$0 = -\frac{d\mathcal{E}_p}{dc} + \frac{d\mathcal{E}_a}{dc} = \frac{d(-\mathcal{E}_p + \mathcal{E}_a)}{dc} \tag{2.8}$$

Here $\mathcal{E}_p$ is the strain energy released, $\mathcal{E}_a$ is the surface energy, dc denotes the crack length increment and we have that the total energy, denoted $\mathcal{E}_t$, is given as $\mathcal{E}_t = -\mathcal{E}_p + \mathcal{E}_a$. So, the critical crack length is the length at which the total energy attains its maxima. It is assumed that the crack growth is slow (quasi-static case) and that energy dissipation, due to friction and plastic deformations, is negligible.

We note that the strain energy released associated to the crack formation is the same as the work done by the application of a tensile load σ along the crack surfaces in the opening up of the crack. Thus, we have

$$\mathcal{E}_p = 2h \int_{-c}^{c} \frac{1}{2} \sigma u_y dz = 2h\sigma \int_{-c}^{c} \frac{1}{2} u_y dz \tag{2.9}$$

Here, the factor 2 accounts for the two (upper and lower) crack surfaces and u_y denotes the displacement of the upper crack surface, given in the case of plane stress for a thin centrally placed crack as [129]

$$u_y = \frac{2\sigma}{E} \sqrt{c^2 - z^2} \tag{2.10}$$

Substituting this in Equation 2.9 and noting that the rightmost integral simply gives the area of an ellipse with semi-major axis c and semi-minor axis $c\sigma/E$, we get that the strain energy released in this case is given as

$$\mathcal{E}_p = \frac{\sigma^2}{E} h\pi c^2 \tag{2.11}$$

As noted, we have considered an isotropic model of the cell wall. One can consider an orthotropic cell wall model [107], in which case, this term has to be modified with additional elastic constants incorporated into the expression. However, it can be shown that the strain energy released in this anisotropic model is comparable to the isotropic model used here [107].

Now, for the crack to propagate, the bonds in the plate have to be broken and hence, an amount of work equal to bond energy must be performed. Let G_0 represent the minimum tearing energy (in units J/m^2), required for the crack to propagate by breaking bonds in its path. Then, for a crack of length $2c$, we have

$$\mathcal{E}_a = 2G_0ch \tag{2.12}$$

Substituting $\mathcal{E}_p$ and $\mathcal{E}_a$ in Eq 2.8 appropriately, we get

$$c_f = \frac{G_0E}{\pi\sigma^2} \tag{2.13}$$

which is the critical crack length, interpreted as the length above which a crack will grow uncontrollably. In our case, since $\sigma = PR/h$, we thus have

$$c_f = \frac{G_0Eh^2}{\pi P^2R^2} \tag{2.14}$$

We note that this paradigm of modelling curved objects by flat surfaces has been utilized widely, both in the case of bacteria [132] and other cells [133].

Role of curvature

In the second case, we incorporate the cell curvature into our calculation. We consider a longitudinally aligned, through the thickness crack of length $2c$ on a thin,

pressurized, cylindrical shell as shown in (Fig. 2.3(b)) and calculate the effect of geometry on the strain energy released. In this case, apart from in-plane deformations, there is an additional out-of-plane deformation in a small region around the crack resulting from the action of normal force due to internal pressure which is directed through the shell [134, 135, 136]. The deflection δ in the normal direction, which in this case is the radial direction, varies over the distance l. The bending energy per unit area is given by $e_b \sim \kappa_b \frac{\delta^2}{l^4}$, where we have used that the curvature change is of the order $\frac{\delta}{l^2}$ [137]. The total bending contribution (ignoring all coefficients) concentrated over the area l^2 is then given by

$$\mathcal{E}_b \sim \frac{\kappa_b \delta^2}{l^2} \tag{2.15}$$

where, $\kappa_b \approx Eh^3$ is the bending rigidity.

The strain tensor for the stretching energy is of the order of $\frac{\delta}{R}$, that is, $\epsilon \sim \frac{\delta}{R}$, where R is the radius of the cylinder. The corresponding stress is then $\sigma \sim E\frac{\delta}{R}$ and the stretching energy per unit area is given by $e_s = \frac{Eh\delta^2}{R^2}$. Thus, the total stretching energy contribution is (ignoring all coefficients)

$$\mathcal{E}_s \sim \frac{Y\delta^2}{R^2} l^2 \tag{2.16}$$

where, $Y = Eh$ is the 2-D Young's modulus for the case of plane stress.

The curvature correction energy term $\mathcal{E}_{cyl}$ is therefore given by

$$\mathcal{E}_{cyl} \sim \frac{Eh^3\delta^2}{l^2} + \frac{Eh\delta^2}{R^2} l^2 \tag{2.17}$$

Minimizing the total energy in Equation 2.17, $\frac{d\mathcal{E}_{cyl}}{dl} = 0 \Rightarrow l = l_m = \sqrt{Rh}$, which gives us a new elastic length scale for localization of deformation.

Plugging in the value of l_m obtained above, we get

$$\mathcal{E}_{cyl} \sim \frac{Eh^2\delta^2}{R} \tag{2.18}$$

We denote the force acting on the crack periphery, due to internal pressure, by f. Varying $\mathcal{E}_{cyl}$ with respect to δ and equating it to the work done by the force f, we get

$$f \sim \frac{Eh^2\delta}{R} \tag{2.19}$$

The force acts along the line of the crack, and hence, the area over which normal stress is applied is of the order of c^2, where $2c$ is the crack length. It follows then that the force acting is of the order of $f \sim Pc^2$, where P is the internal pressure. Substituting this value of f in Equation 2.19, we get the normal deflection $\delta \sim \frac{Pc^2R}{Eh^2}$. Therefore, using Equation-2.18, we get

$$\mathcal{E}_{cyl} = K_1\frac{Eh^2\delta^2}{R} = K_1\frac{P^2R^2}{Eh}\frac{c^4}{Rh} = K_1\frac{\sigma^2c^2h}{E}\frac{c^2}{Rh} \tag{2.20}$$

where K_1 is a dimensionless constant. This constant $K_1 \sim \pi(0.317\sqrt{12(1-\nu^2)})$ [134], where ν denotes the Poisson's ratio of the shell material. Since $0 \leq \nu \leq 1/2$ [122], we have that $K_1 \approx \pi$. Therefore, we get that the total strain energy released is given by

$$\mathcal{E}_i \simeq \mathcal{E}_p + \mathcal{E}_{cyl} = \mathcal{E}_p\left(1 + \frac{c^2}{Rh}\right) \tag{2.21}$$

We can now calculate the critical crack length c_f using energy balance criterion as in the planar case. This is then given as the unique (positive) real root of the cubic

equation

$$c^3 + c\frac{Rh}{2} - \frac{G_0 ERh}{2\pi\sigma^2} = 0 \tag{2.22}$$

where $\sigma = \sigma_\phi = PR/h$ (such a cubic equation, of the general form $t^3 + pt + q$ is termed as the depressed cubic equation and its discriminant Δ is always negative when $p > 0$, in which case it will have a unique real root, which is always positive if in addition we have $q < 0$).

To understand the effect of geometry of the cell wall, a comparison of these two cases needs to made. For this, we first need to compute the minimum tearing energy G_0, which we do in the following section.

2.3.2 Tearing Energy: Role of Cross-Links

A crack typically propagates by rupturing the bonds lying across its plane [129]. The tearing energy is conventionally calculated by estimating the energy cost for disrupting the bonds lying across the plane of the crack. However, in a cross-linked polymer, as the crack propagates, it encounters chains of monomers lying between adjacent cross-links. The forces involved are transmitted through the cross-links. So, in order to break the chain, each bond in the chain has to be supplied energy almost equalling the energy required to rupture them even though one of the bonds might eventually rupture [138, 139]. Thus, the cross-linked polymeric structure of the peptidoglycan mesh can safeguard the cell against mechanical failure by resisting crack propagation in this manner.

For an axially aligned crack on the cell wall to propagate, it must cross a number of glycan strands cross-linked by peptide bridges. Glycan strands are made up of repeating disaccharide units of N-acetylglucosamine (NAG) and N-acetylmuramic

acid (NAM). A peptide stem of few amino acids is attached to NAM. The glycosidic bonds between the alternating sugars NAG and NAM form the backbone of the glycan chain [29]. So, if there are on an average m such bonds between adjacent cross links, then total energy needed to disrupt the chain will be $\approx mE_c$, where E_c denotes the dissociation energy of the bond. Let Σ denote the number of glycan strands crossing per unit area in the fracture plane. We then have

$$G_0 \approx mE_c\Sigma \tag{2.23}$$

To relate m to the average length of the glycan chain between adjacent cross-links (say l_{avg}), we define n to be the average number of glycosidic bonds connecting the disaccharide units between adjacent cross-links (see Fig. 2.3(b)). It follows then that $m = 2n$ and $l_{avg} = (n+1)$ disaccharides (hence, representing G_0 in terms of n allows us to compare its value to l_{avg}).

We estimate G_0 as follows- the average dissociation energy of a glycosidic bond, specifically, a C$-$O bond, is of the order of $E_c \approx 6 \times 10^{-19} J$ [120]. The thickness of the cell wall is ≈ 5 nm and the glycan inter-strand spacing is ≈ 2nm (see Table 2.1). We then get $\Sigma \approx (6 \times 10^{16}/m^2)$. Next we estimate n across a given glycan strand, which we relate here to the glycan strand length. For a given glycan strand, which we for convenience denote g, we have

$$n = \frac{c-1}{i-1} \tag{2.24}$$

where c denotes the total number of disaccharide units between the two extreme cross-links of g (in other words, we are counting those disaccharide units in the glycan strand that lie between any pair of adjacent cross-links) and i denotes the total number of cross-linked peptide stems on the glycan strand g. In the limit of long glycan strands spanning the circumference of the cell, we have $n \sim 1/k$, where

k denotes the degree of cross-linking across the glycan strand as in this case, due to periodicity, $c = l$, where l denotes the total number of disaccharide units for the given glycan strand g. Since l is large, it follows that $n \sim 1/k$ where k denotes the fraction of cross-linked peptides. In the case of *E.coli*, peptide stems rotate around the glycan backbone by roughly 90° per disaccharide [13], so only 50% of the peptide stems are available for cross-linking and it has been observed that the degree of cross-linking is around 30% [10], so $n \sim 3$. This also illustrates how a lower degree of cross-linking can enhance the toughness of the cell wall.

However, we now exhibit that placing of the cross-links at the terminating units can increase the value of n for shorter length glycan strands substantially. In particular, for glycan strands which are cross-linked at the ends, the value of the numerator in Equation 2.24 is maximized. To see this, let us consider a glycan strand g of length l disaccharide units. It follows from Equation 2.24 that the value of n for a strand of fixed length will be maximized when the peptide stems at the end of the glycan strands are cross-linked. In this case, $c \sim l$. Also, for the degree of cross-linking denoted k, we will have $i \sim kl$. Therefore, taking n now as a function of l, we have

$$n(l) \sim \frac{l-1}{kl-1} \tag{2.25}$$

Taking $k = 0.3$ and allowing for at least two cross-links across the length of the strand, we get $n \sim 3-6$. The value of n decreases as the length of the glycan strand increases and for length of glycan strand $l \sim 7-8$, the value of $n \sim 5-6$. Now, given a glycan strand length distribution p, the average value of n across the cell wall is

$$n_{avg} = \sum n(l)p(l) \tag{2.26}$$

where $p(l)$ denotes the proportion of glycan strand lengths of length l. It is clear that

a higher proportion of glycan strands of strand lengths $\sim 7-8$ disaccharide units will enhance the average value of n across the cell wall (note that for very short strands with length 4 disaccharides or less, only a single peptide stem will be cross-linked with cross-linking degree around 30% [140], so a similar analysis is not possible). So, in summary, we conclude that for any glycan strand which are cross-linked at their termini and allowing for at least two cross-links across the strand, we get $n \sim 3-6$, with strands of length $7-8$ disaccharides being optimal in this regard, having $n \sim 5-6$, while in the limit of long glycan strands, we have $n \sim 3$. This in particular can explain the following remarkable experimental observations 1- in Ref. [11], where HPLC analysis of glycan strand length distribution detected a substantial presence of short length glycan strands, with the length distribution having a mean value of ~ 8 disaccharides for about 70% of the strands and 2- in Ref. [5, 10, 12], which concluded that $\geq 80\%$ of the 1,6 anhydroMur$N$Ac terminal muropeptides are cross-linked and suggested similar proportions of cross-linking at the Glc$N$Ac termini as inferred from peptidoglycan labelled with galactosyl transferase. Our analysis underlines the significance of terminally cross-linked short length glycan strands and in particular, gives an illustration of how design features of the cell wall that underpin the disorder in its structure can affect its mechanical properties in a significant manner.

Glycan strands are intially polymerized in longer lengths of upto 50 disaccharide units and are thereafter shortened by the action of appropriate lytic transglycosylases (LTs), to tailor-fit into the PG mesh [141]. Although the exact algorithm that the cell follows to cleave glycan strands is not clear, it is pertinent to note that by appropriate cutting of these strands, the cell can increase the value of n. For instance, n increases when glycan strands are cut in between adjacent in-plane cross-linked peptide stems and interestingly, the preference of glycan strands to maintain terminal cross-links does seem to indicate that LTs which cleave glycan strands subsequent to polymerization, frequently act on them in this manner.

The extent of cross-linking also plays a key role in our analysis. A high degree of cross-linking increases the stiffness of the cell wall [6]. However, it follows from Eqn. 2.23 and Eqn. 2.24 that in this case, the tearing energy is lower, thus making the structure vulnerable to cracks. On the other hand, while a lower degree of cross-linking increases the tearing energy, it also makes the cell wall less stiff [112]. Thus, the extent of cross-linking has to be delicately balanced to ensure optimal levels of stiffness and toughness. A key mechanism of the cell wall is that of hydrolysis or the cleavage of pre-existing peptide and glycosidic bonds in the peptidoglycan mesh. Experiments indicate that *E.coli* mutants which are deficient in hydrolysis enzymes undergo rapid lysis, proving the essential role it plays in ensuring cell viability [45]. Our analysis suggests that peptide bond cleavage due to hydrolysis can secure the cell by increasing resistance to crack propagation: For the crack to propagate, it has to stretch all glycosidic bonds between adjacent cross-links before one of them ruptures. A possible way to arrest the progress of the crack is thus to cleave a peptide bond, so that the number of bonds between adjacent cross-links increases, in other words the value of n increases. This is analogous to the common trick employed by mechanics to arrest the progress of a crack by drilling a small hole at the tip of the crack [142]. The timescale involved in peptide bond cleavage can however impose an upper limit on the crack speed, below which bond cleavage action to inhibit crack propagation is feasible- assuming that hydrolases diffuse sufficiently fast to act uniformly across the cell wall and that the mechanical stress on the peptide bonds is only due to the turgor pressure, we first calculate the rate of peptide bond cleavage. In one cell cycle, with time $\tau = 20$ minutes, a turnover of $40\% - 50\%$ of the cell wall material takes place [13] and between two adjacent circumferential cross-section of the cell, there are ≈ 500 cross-links (with 30% cross-linking and $\sim 2\pi R$ disaccharides comprising all glycan strands in a cross-section). So, peptide cross-links between two adjacent cross-sections are excised at a rate of $k_1 \sim 10 - 12$ min^{-1}. Now, since a peptide bond has to be cleaved in the time that the crack front traverses the inter-strand distance

d, the speed is thus limited to $\sim 18 - 24$ nm min^{-1} or slower. However, higher stresses on the cross-linkers in the vicinity of the crack tip can potentially lead to a surge in the hydrolytic activity locally. While the exact effect of mechanical stress on the rate of severing of cross-linkers is not clear, it has been hypothesized that increasing stress results in lowering of the energy barrier to hydrolysis, thus resulting in a higher rate of breakage of cross-linkers [33]. Nonetheless, for fast moving cracks, cross-link cleavage is likely to be not fast enough to act. For instance, in the case of *S.aureus*, daughter cell separation, for which mechanical crack propagation has been implicated, happens at speed around $1\mu\text{m}/s$ [118]. For crack speed of this order, peptide hydrolysis is unlikely to be able to play a mitigating role.

2.3.3 Critical Crack Length

We now calculate critical crack lengths in the planar case as well as the cylindrical case. In Fig. 2.4, we plot the total energy ($\mathcal{E}_t$), defined as the difference of the strain energy released and the surface energy, against the crack length, in these two cases, varying the value of n. The critical crack length is obtained at the maxima of the energy curve, which we observe, increases as the value of n increases. For the cylindrical case, the critical crack length is smaller than the planar case, with this difference increasing with increase in value of n. Thus at lower crack length values, the planar case provides a good approximation to the case of a crack on the cell wall under turgor pressure. However, at higher crack lengths, curvature becomes important and the planar approximation starts to break down. In the case $n = 1$, which corresponds to a 100% cross-linked sacculi, the critical crack length is small, with $c \approx 6$ nm. When the effect of cross-linking is completely ignored, that is when a very thin crack propagates by disrupting the bonds lying across the fracture plane (so $m = 1$ in Equation 2.23), then critical crack length is even smaller. This underlines the significance of appropriate levels of cross-linking in maintaining the

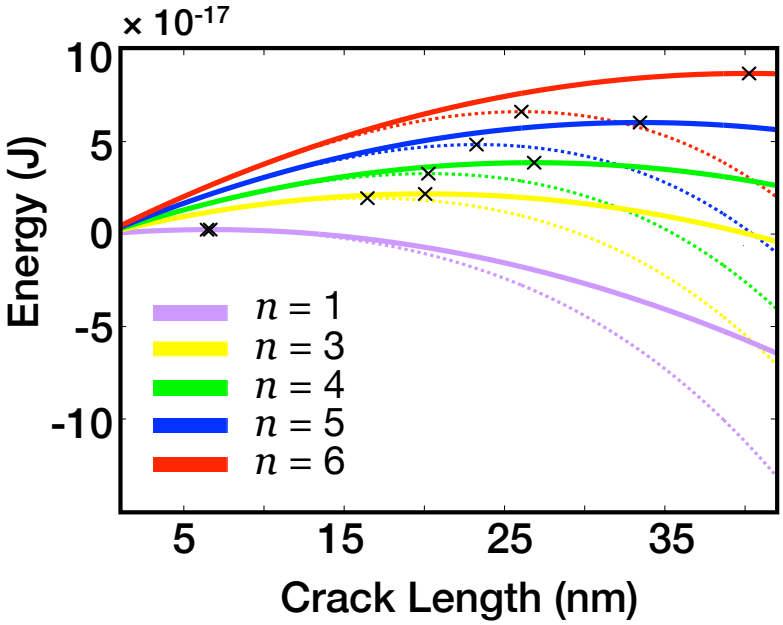

Figure 2.4: Total energy $\mathcal{E}_t$ against crack length c, for different degrees of effect of crosslinking. The solid lines represent the plane case, while dotted lines represent the cylinder case. The cross ($\times$) represent the critical crack lengths c_f. For values of the elastic modulus E, the cylinder radius R and the thickness h, see Table 2.1.

integrity of the cell wall. It is also instructive here to note that the total energy at the critical crack length compares well to the total energy of the glycosidic bonds comprising the glycan strands lying between adjacent cross-links times the number of strands spanning the length c_f (with inter-glycan strand distance ~ 2 nm). For instance, in the $n = 3$ case, the number of glycosidic bonds lying between adjacent cross-links is $2n = 6$ and with $c_f \sim 20$ nm, the number of glycan strands spanning this distance is ~ 10, so we can then see that the total energy of all such bonds in such glycan strands $\sim 10 \times 6 \times 6 \times 10^{-19}$ J $\approx 3 \times 10^{-17}$ J which approximates $\mathcal{E}_t$ in this case.

Here we use the energy balance criterion to calculate the critical crack length, which is accurately applicable for very thin cracks. For the cell wall, due to the cross-linked structure, the unstrained tip width is approximately the length between two adjacent cross-links, so the length to width ratio in our case will be $\sim 10 - 20$, which ensures a degree of accuracy. More accurately, this estimate is in fact a lower

Parameters	Values	References
Cell Wall Parameters		
Radius of Cell (R)	$\sim 0.5\mu$m	[144]
Thickness of the cell wall (h)	~ 5 nm	[126]
Turgor pressure (P)	1 atm	[122]
Elastic Modulus of Cell Wall (E)	30 MPa	[7]
Glycan Inter-strand Spacing (d)	2 nm	[9]
MreB Parameters		
Number of MreB molecules/cell (N)	$17000 - 40000$	[145]
Elastic Modulus of MreB (E_{MreB})	2 GPa (similar to actin)	[146]
MreB monomer diameter ($2r_0$)	5.1 nm	[8]

Table 2.1: Parameter values for *E.coli*.

bound for the critical crack length which well illustrates the reinforcing effect of the cross-linked structure of the cell wall in preventing failure due to cracking (more precise estimates can be obtained by taking the exact geometry into consideration). Interestingly, critical crack total length for the Gram positive bacteria *S.aureus* has been suggested to be around 40 nm [118], which is commensurate to these estimates. Though *S.aureus* has a spherical geometry and its cell wall has a multi-layered structure, the composition of the Gram positive and Gram negative cell walls remain conserved [143], which suggests that the critical crack length in both cases can be comparable.

A natural question now is whether the role of cross-linking in maintaining the integrity of the cell can be supplanted by other design components of the cell, for instance the cytoskeleton MreB. In the next section, we explore the role of the cytoskeleton in strengthening the cell wall against failure from crack propagation. In particular, we probe if the cytoskeleton can effectively reinforce the cell against crack propagation, even when the effect of cross-linking is discounted.

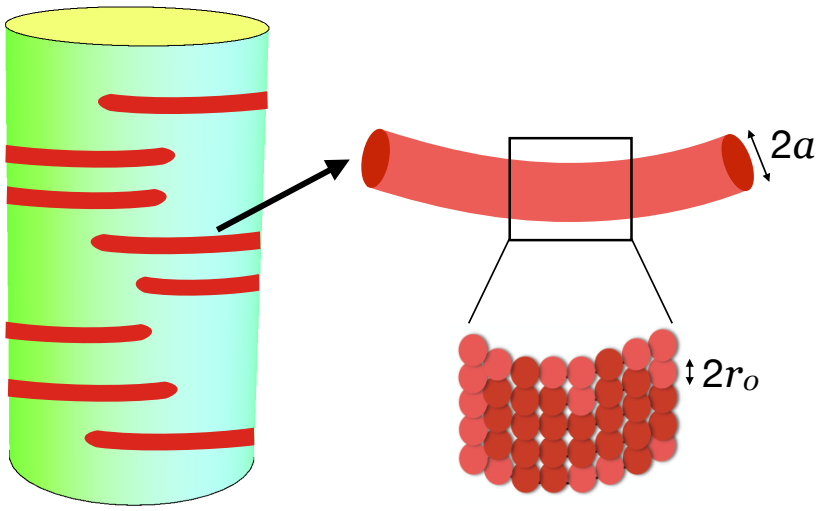

Figure 2.5: MreB cytoskeleton modelled as disconnected filament assemblies aligned in the hoop direction, with filament bundle having bundle radius a and preferred radius r. The filament bundle consists of monomers modelled as spheres of radius r_0.

2.4 Cytoskeletal Reinforcement

In this section, we study the effect of actin-homologue MreB on the toughness of the cell wall, in particular examining the reinforcement of the cell wall by MreB and its effects on the critical crack length. While early work had suggested that MreB formed as a cell spanning helix [47, 51], more recent works have established that MreB forms disconnected assemblies in the cell that move processively in the hoop direction [52, 53, 54] (Fig. 2.5). Here, we model MreB as a collection of disconnected bent cylindrical rods oriented in the hoop direction of the cell.

MreB binds directly to the cytoplasmic side of the inner membrane [147]. While the *in vivo* ultrastructure of MreB remains to be elucidated, it has been observed *in vitro* that MreB forms bundles in solutions [55] and binds as filaments to membrane [56]. Biophysical modelling has shown that the orientation of MreB along the direction of maximal curvature is determined by the trade-off between the energetics of filament

bending, membrane deformation and the work done against the turgor pressure [148]. For the bacterial cell, the presence of high turgor pressure can ensure that the MreB filaments deform to the cell membrane. In this case, the configuration of MreB is distorted from its preferred shape. In vitro studies have shown that MreB filaments are highly curved (with width $>$ 200 nm), so the preferred curvature is greater than the typical curvature of the bacterial cell [56]. Therefore, with the preferred radius being smaller than the cell radius, an inward directed pressure is exerted, which we calculate below. It should be noted that for high values of the cross-sectional radius, the energy cost of filament bending increases and it is possible that it becomes energetically favourable for the membrane to deform to the filament[148]. Here, since we are interested in only calculating the inward pressure exerted, we take as an input a configuration of the MreB modelled as bent cylindrical rods of given cross-sectional radius, denoted a, which is deformed from its preferred orientation onto a given orientation determined by the cell radius. We then calculate the pressure exerted for a wide range of values of a, ranging from 3.2 nm [56] to 40 nm [149]. We also note that although MreB has been observed to move persistently around the long axis of the cell over long time scales [52, 54], since we are estimating the average pressure exerted, we will assume that it is localized. To calculate the average pressure exerted by MreB, we first calculate the total energy of the MreB filament bundles constrained onto the cell wall, for which we need to express the energy functional as an integral over their center line. Before that, we briefly recall the Darboux frame. Let $\mathcal{S} = S(x, y)$ be a surface in $\mathbb{R}^3$. We denote the tangent vectors S_x and S_y, which span the tangent plane to the surface at the $S(x, y)$. Suppose now that we have a curve on the surface, given by the mapping

$$\phi : t \mapsto S(x(t), y(t))$$

The tangent to the curve at the point $S(x(t), y(t))$ is then given by $\mathcal{T} = x'S_x + y'S_y$.

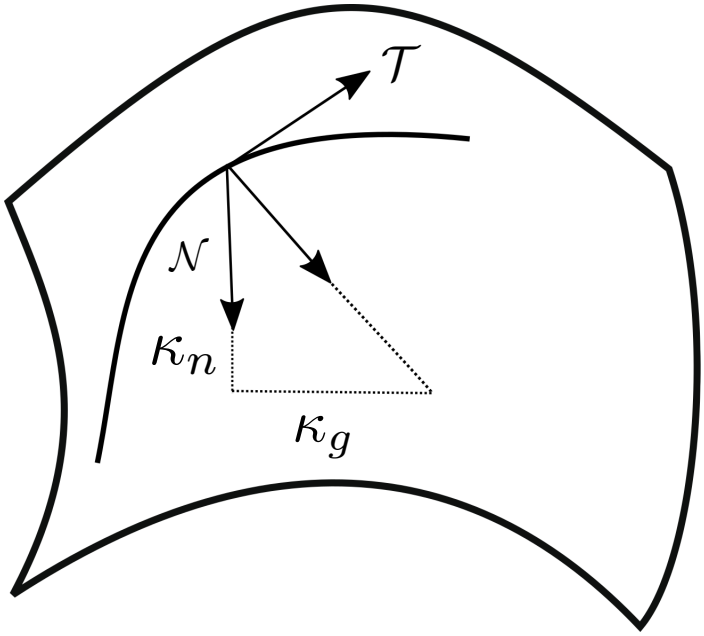

Figure 2.6: The Darboux frame describing curves on surfaces, with $\mathcal{T}$ being the tangent to the curve, $\mathcal{N}$ the surface normal. The Darboux frame is $(\mathcal{T}, \mathcal{N}, \mathcal{B})$, where $\mathcal{B} = \mathcal{T} \times \mathcal{N}$.

We now define a frame for the curve ϕ (which is thought of as the centerline of the filament bundles under consideration in this work). In this case, we want to use frame to incorporate the information that the curve lies on a surface, thus we will be using the Darboux frame and not the usual Frenet-Serret frame.

Let $\mathcal{T}$ denote the tangent to the curve at $S(x(t), y(t))$ as before. Let $\mathcal{N}$ denote the normal to the surface at $S(x(t), y(t))$. We also further define another unit vector $\mathcal{B}$ as $\mathcal{B} = \mathcal{T} \times \mathcal{N}$. Together, the vectors $(\mathcal{T}, \mathcal{N}, \mathcal{B})$ define the darboux frame for the curve ϕ, lying on the surface $\mathcal{S}$.

It is easy to see, since $\mathcal{T}, \mathcal{N}, \mathcal{B}$ are orthonormal, we have that $\mathcal{T}' \cdot \mathcal{T} = \mathcal{N}' \cdot \mathcal{N} = \mathcal{B}' \cdot \mathcal{B} = 0$ and further

$$(\mathcal{T} \cdot \mathcal{N})' = (\mathcal{B} \cdot \mathcal{N})' = (\mathcal{T} \cdot \mathcal{B})' = 0 \tag{2.27}$$

This implies the existence of scalar functions κ_n, κ_g and τ such that we have

$$\mathcal{T}' = \kappa_n \mathcal{N} + \kappa_g \mathcal{B} \tag{2.28a}$$

$$\mathcal{N}' = -\kappa_n \mathcal{T} + \tau \mathcal{B} \tag{2.28b}$$

$$\mathcal{B}' = -\kappa_g \mathcal{T} - \tau \mathcal{N} \tag{2.28c}$$

Here, κ_n is the normal curvature of the curve, κ_g is the geodesic curvature of the curve and τ is the twist of the curve.

We can now define the Darboux vector

$$\Omega = \tau \mathcal{T} - \kappa_g \mathcal{N} + \kappa_n \mathcal{B}$$

and thus, we will have

$$\mathcal{T}' = \Omega \times \mathcal{T}, \ \mathcal{N}' = \Omega \times \mathcal{N}, \ \mathcal{B}' = \Omega \times \mathcal{B} \tag{2.29}$$

Now, for such a curve constrained to a surface, given the Darboux frame, the general energy functional reads [150]

$$\mathcal{E} = \frac{1}{2} \int_0^{L_{fil}} ds (I_{ij}(\kappa_i - c_i)(\kappa_j - c_j) + \beta(\tau - c_t)^2) \tag{2.30}$$

where κ_i and κ_j are from the set $\{\kappa_g, \kappa_n\}$ of geodesic and normal curvature, and the terms c_i, c_j belong to the set $\{c_g, c_n\}$ of preferred curvatures. The tensor I_{ij} is the inertia tensor. Finally, c_t denotes the preferred twist and β denotes the twist modulus.

For our case, we assume that the cross section of MreB is circular. The inertia tensor I is thus isotropic and can be written as $I = \alpha\delta_{ij}$, where $\alpha = E_{MreB}\pi a^4/4$, denotes the bending modulus, a denotes the cross-section radius and E_{MreB} the elastic modulus. We note that $\beta = \alpha/(1+\nu_m)$ [137], where ν_m denotes the Poisson ratio. We make the simplifying assumption that the Poisson ratio $\nu_m = 0$ for MreB, since this does not qualitatively change our results. So we have $\beta = \alpha$.

Also, it follows from the analysis below that for a wide range of values of the radius a, the elastic energy is several orders of magnitude greater than k_BT, hence we ignore the effect of thermal fluctuations.

2.4.1 MreB Model

MreB is modelled as several disconnected cylindrical rods, bent and oriented in the hoop direction of the cell, as shown schematically in Fig. 2.5. We will refer to these cylindrical rods as MreB bundles. We assume that the preferred shape of MreB is a bent cylindrical rod, whose centerline can be visualised as an arc of a circle of radius r. In the final configuration, this radius changes to R. Using Equation 2.30, together with $\kappa_g = c_g = \tau = c_t = 0, \kappa_n = 1/R$ and $c_n = 1/r$, we obtain the total energy for n_f bundles as

$$\mathcal{E}_f = \frac{n_f L_{fil}\alpha}{2}\left(\frac{1}{R} - \frac{1}{r}\right)^2 \tag{2.31}$$

As we shall see below, the inward pressure exerted by MreB bundles is independent of their length. We thus make the simplifying assumption that the length of all the bundles is the same.

Radius \ Length	250 nm	500 nm	1500 nm
3.2 nm	437-656	218-328	73-109
10 nm	45-67	22-33	7-11
20 nm	11-17	6-9	2-4
40 nm	3-5	1-2	~ 1

Table 2.2: Range of computed number of disconnected MreB filament bundles in the cell.

2.4.2 MreB filament bundles in the cell

In this section, we estimate the number of MreB filament bundles in a typical cell. The number of MreB monomers has been estimated to lie in the range $17000-40000$ (see Table 2.1). The number of filament bundles will depend on the number of MreB monomers in a single bundle, which in turn will depend on the radius of the bundle, its length and the packing of the monomers in the bundle. Since the bundle is modelled as a cylinder of length $L_{fil} = l_f$ and radius a, and monomers are modelled as balls of fixed radius r_0 (see Fig. 2.5), the number of monomers in the filament bundle will be a fraction of number $n_m \approx \frac{\pi a^2 l_f}{\frac{4}{3}\pi r_0^3}$. This is effectively a problem of packing of balls of uniform radius in a cylinder of given dimensions. It is obvious that not all the volume of the cylinder can be occupied by the balls. Following the resolution of Kepler's conjecture, it is now known that for sufficiently large containers, the volume fraction occupied by balls of a uniform small radius is bounded above by $\frac{\pi}{3\sqrt{2}} \approx 0.74$, which is achieved by cubic close packing or hexagonal close packing [151]. In other words, the densest packings occupy about 0.74 of the volume of the container.

Another possible configuration can be described as follows- we can think of each filament bundle as an aggregation of filaments with each filament having the same number of monomers $\sim l_f/2r_0$. Calculating the number of filaments will thus give us the total number of monomers in this configuration. This is given approximately by

dividing the area of cross-sectional circle of the cylindrical container by the area of the equatorial circle of the monomer, giving us the number $\rho_0 = \left(\frac{a}{r_0}\right)^2$. Here we are assuming that the arrangement is such that the equatorial circles of the monomers on the top cover almost the whole area of the cross-sectional circle of the cylinder and that the monomers are arranged in collection of straight lines, piled below the monomers on the top. Thus, the number of monomers in this arrangement is given by $\frac{l_f \rho_0}{2r_0}$ and it is straightforward to see that in this case, the monomer balls occupy $\sim 2/3$ of the volume of the cylinder.

Now, since the filaments have a robust elastic modulus of around 2 GPa, it is fair to assume to that the packing of the monomers has to be sufficiently dense. On the other hand, since the monomers are much smaller than the cylindrical filament, the upper bound for the volume has to be around 0.74, as explained above. So, we assume that the volume fraction of the monomers in the cylindrical container is $\sim 0.5 - 0.75$. So, with bundle radius denoted a and length denoted l_f, and with total number of MreB monomers denoted N, we have that the number of filaments n_f lies in the range $\frac{28N}{a^2 l_f}$ to $\frac{42N}{a^2 l_f}$, with a and l_f given in nanometers and where we have used the value $r_0 = 2.5$ nm (Table 2.1). We tabulate (Table 2.2) the number of filament bundles, where the length of such filament bundles taken as 250 nm, 500 nm and 1500 nm, and bundle radius taken as 3.2 nm, 10 nm, 20 nm and 40 nm. We have assumed here, for simplicity, that all the MreB monomers in the cell are part of some MreB bundle. However, there can be several MreB monomers in the cell cytoplasm, so that the values in Table 2.2 give us an upper bound for the number of MreB bundles present in the cell.

The radial force is then given by

$$F_f = \left.\frac{\partial \mathcal{E}_f}{\partial R}\right|_R \tag{2.32}$$

and the average pressure exerted is

$$P_f = \frac{n_f L_{fil} \alpha}{2\pi R^3 L} \left(\frac{1}{r} - \frac{1}{R} \right) \tag{2.33}$$

where L denotes the length of the cylinder. The effective turgor pressure acting on the cell wall is then given by

$$P_{eff} = P - P_f \tag{2.34}$$

Experiments have reported shorter length MreB assemblies ($\sim$ 250 nm) as well as long ones nearly covering half of the cell's circumference ($\sim$ 1500 nm) [148, 149, 152]. However, the pressure exerted by MreB is independent of the length of a bundle. This results from fixing the total number of MreB molecules in the cell, which effectively subsumes the role of the length of the bundles. This also holds when we choose the lengths of bundles to be variable in the cell, present with varying proportions. To illustrate this, we plot the pressure exerted by the MreB against the preferred radius for different values of bundle length and fixed value of bundle radius, taken as 20 nm in Fig. 2.7 (left). In Fig. 2.7 (right), we plot the pressure against preferred radius with fixed bundle length taken 250 nm and different values of bundle radius. We observe that for a wide range of preferred radius (0.2μm-0.4μm), the pressure exerted even for very large bundle radius is much less than the turgor pressure.

We next explore the variation of the pressure exerted by MreB assemblies as the radius of the cell varies, in particular to understand whether an appropriate change in the dimensions of the cell can result in a significant increase in the pressure exerted by MreB. Fixing h, we plot the pressure exerted against the radius of the cell (Fig. 2.8 (left)) in the case that length of the cell L is kept fixed and in the case that volume of the cell $V = \pi R^2 L$, is kept fixed. We infer that as R_{cell} increases, the

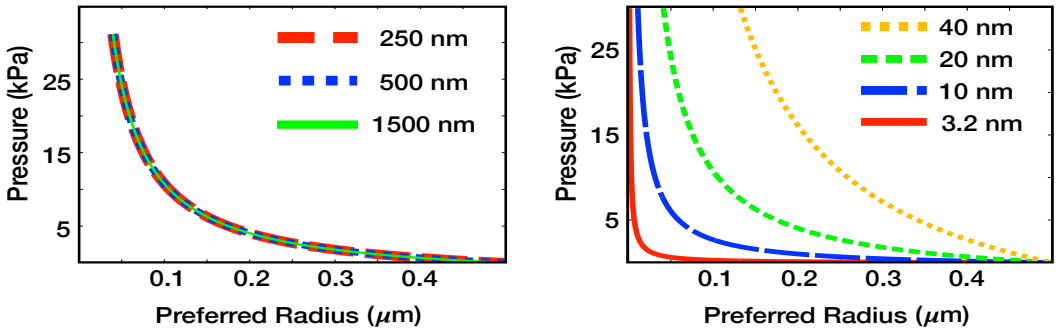

Figure 2.7: (Left) Average pressure P_f exerted by MreB vs preferred radius r, for different bundle lengths as given in the inset, with bundle radius fixed at 20 nm. The length independence of the pressure exerted can be observed here. (Right) The pressure exerted against the preferred radius, with fixed bundle length taken 250 nm for different values of bundle radius as in the inset.

inward pressure exerted by MreB will become negligible, though as we can deduce from Equation 2.33, the decay is much slower in the case when volume is fixed. We observe that interestingly, in both cases, with $r = 0.3\mu$m, the pressure exerted attains maxima when $R_{cell} \approx 0.5\mu$m, with similar maxima values, indicating that the pressure exerted will not be significant even if the cell radius is changed. In general, dimensions of the cell may be regulated by a combination of multiple factors, for instance cell width of *Bacillus subtilis* has been suggested to be determined by a delicate balance between the Rod system and class A penicillin binding proteins (aPBPs) [153]. In the following, we fix the preferred radius r of MreB to 0.3μm, noting that our results hold qualitatively over a wide range of values of r (0.2μm $-$ 0.4μm).

2.4.3 Effect on crack length

We now quantify the role of MreB as a determinant of the critical crack length and compare its effect to that of the cross-linked structure of the cell wall. As explained previously, pressure is exerted by MreB in the inward direction. This acts to counter the turgor pressure, resulting in a lowering of the effective pressure on the cell wall. We now examine the effect of this lowering of the pressure, on the critical crack

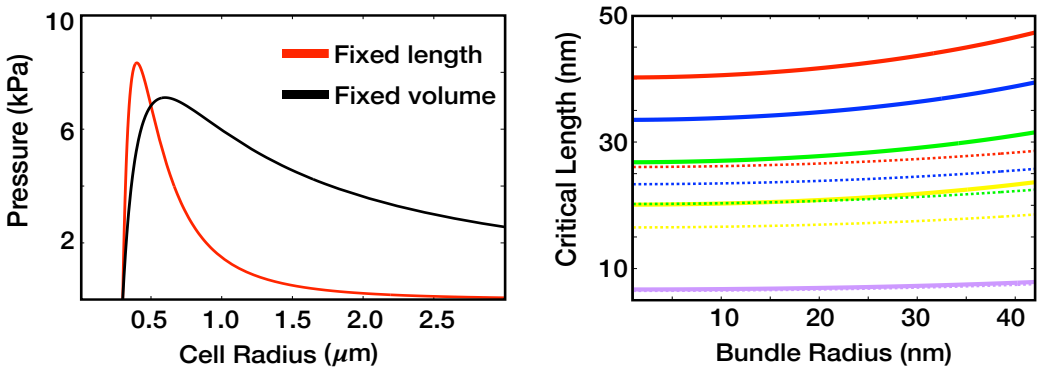

Figure 2.8: (Left) Average inward pressure P_f exerted by MreB with preferred radius $r = 0.3\mu$m and bundle radius $a = 40$ nm as the radius of the cell R_{cell} varies, in the case length of the cell is fixed (red) and in the case volume of the cell is fixed (black). (Right) Critical crack length vs Bundle radius for MreB. Lines indicate the planar case, while dotted lines indicate the cylindrical case. In both cases, the degree of effect of crosslinking is taken as indicated, from bottom to top, $n = 1$ and $n = 3, 4, 5, 6$, depending on the length of the glycan strand.

length of the cell wall. We plot the critical crack length against the bundle radius (Fig. 2.8 (right)). We take into account the planar case and the cylindrical case, besides incorporating the effect of the cross-linking (with n as in Section 2.3.2). We note that when the bundle radius is zero, the effect of MreB is negated. So, the critical crack length in this case, is the same as the critical crack length as calculated in the first part, where the effect of MreB was not under consideration. We observe that in all degrees of cross-linking, the critical crack length does not change much even for very large values of bundle radius. This underlines the significance of cross-linking in the protection of the cell wall against cracking.

Recent work has revealed that the outer membrane of *E.coli*, acting in tandem with the cell wall, is the primary mechanical unit of the cell, guarding it against various perturbations [154]. Since MreB, on the other hand, acts on the plasma membrane, this, in conjunction with our analysis, suggests that MreB is unlikely to have a significant direct mechanical contribution in affecting the tearing of the cell wall. It is however possible that MreB indirectly affects the toughness of the cell wall. For instance, a higher concentration of MreB might increase the cross-linking density

[6], which can be deleterious for the toughness of the cell wall even as the stiffness of the cell wall will increase.

2.5 Discussion

In this chapter, we studied the role of the cross-linked structure of the cell wall in ensuring sufficient resistance to crack propagation. We deduced that the tearing energy varies inversely with the degree of cross-linking. We also showed that terminally cross-linked short length glycan strands can dramatically enhance the tearing energy. In particular, we showed that for about 30% cross-linking of the cell wall, as has been observed for *E.coli* [10], the optimal length of the glycan strands for maximizing the tearing energy, are shorter length glycan strands with length $\sim 7-8$ disaccharides, cross-linked at the ends. This provides a possible explanation for surprising experimental observations, which have demonstrated an abundance of shorter length filaments in the peptidoglycan mesh [11] and of the strong preference of glycan strands to cross-link to each other at the termini [10, 12]. We estimated the critical crack length for different degrees of cross-linking. Finally, we investigated the effect of MreB reinforcement of the cell wall, modelling MreB as several disconnected bent cylinders and estimated the inward pressure exerted for a wide range of parameters. We concluded that the effect of the cross-linked structure of the cell wall plays the primary role in ensuring the integrity of the cell wall.

In this study, we have computed an average value of the tearing energy G_0 across the sacculus. However, the specific local geometry of the peptidoglycan mesh near the tip of a crack can play an important role in its propagation. Indeed, coarse grained simulations of the peptidoglycan sacculus have indicated the possibility of peptide bonds under stress, like those near the crack tip, ending up aligned even in the circumferential direction [119]. This, for instance, can lead to a local increase

in the value of the tearing energy, resulting in higher resistance to propagation of the crack. Detailed numerical simulations are required to delineate the effect of local geometry of the peptidoglycan mesh on the tearing energy, leading upto a more precise calculation of its value and will be undertaken in subsequent work. Nevertheless, since the tearing energy may vary for distinct local geometries near the tip of specific cracks, our study of the average tearing energy across the sacculus assumes significance and paves the way for more exhaustive investigation.

An interesting feature of our analysis is the illustration of a standard dilemma faced when engineering materials, which is to ensure optimal levels of stiffness and toughness, as the two requirements usually are at cross purposes [155] - in this case, we showed lower degrees of cross-linking result in higher tearing energies, thus offering better protection to the cell wall. On the other hand, a higher degree of cross-linking results in stiffer cell walls [6, 112], allowing the cell wall to bear turgor pressure and to preserve its shape. Similarly, longer glycan strands results in enhanced stiffness [9], while, shorter length glycan strands can amplify the toughness of the cell wall, as we exhibited. A natural question now is to understand how bacteria maintain an optimal degree of cross-linking, appropriate glycan strand length distribution and precise placing of the cross-links along the strand lengths, fine tuning their structure to ensure the right mix of mechanical properties under a variety of conditions. It will be particularly interesting here to probe the role of hydrolysis, which can affect both the degree of cross-linking and the glycan strand length distribution [44] and which, as we discussed, can mitigate the danger of failure due to crack propagation by cleaving appropriate peptide bridges. Interestingly, treatment of certain strains of *E.coli* with antibiotics like vancomycin [119], which acts by inhibiting formation of new cross-links, often results in bulging of the cell, leading to cell lysis. It has been hypothesised that a build-up of cross-linking defects in a small region under the effect of the antibiotic, leads to formation of a pore in the cell wall, which when it exceeds a critical size, results in irreversible bulging of the plasma membrane through

it. Intriguingly, bulge formation does not seem to lead to large scale cracking of the cell wall, which suggests that the geometry of the pore is such that the critical size for membrane bulging is attained before it becomes energetically favourable for cracking to occur. The precise geometry of such pores formed by the effect of antibiotics is unclear, however under the assumption of a circular pore, a critical pore radius of $\sim$ 20 nm has been calculated, beyond which irreversible membrane bulging will occur [156]. On the other hand, our calculation indicate critical crack length, denoted c_f, for the cell wall of $\gtrsim$ 20 nm for axially aligned narrow cracks, it is possible that criticality for membrane bulging is achieved before criticality for large scale cracking, particularly if the pores formed by the effect of antibiotics have a higher radius of curvature at the tips, resulting in lower stress concentrations [129].

The overarching theme of our study was to understand the molecular mechanistic underpinnings of the mechanical properties of the cell wall, in particular its toughness. More experiments are necessary to get a complete understanding of the problem, for instance analogous to those carried out for other biocomposites like nacre, which has an interesting sawtooth shaped force extension curve, explaining its remarkable toughness [62]. Further, experimental study of the behaviour of cracks on the cell wall under varying conditions can elucidate not just the mechanical properties of the cell, but also its growth process, as demostrated in recent experiments using laser nano-ablation, where cuts were introduced on *C.elegans* cell surfaces and were probed to study embryo elongation [133]. An outstanding question in this regard is to probe the self-repair mechanism of the bacterial cell and its ability to heal cracks on the cell wall. Computer simulation, based on the glycan strand length distribution, have indicated the presence of small cracks aligned in the axial direction [113]. Such small cracks, which can play an important role in ensuring passage of nutrients and waste products, can nonetheless develop into critical flaws eventually under the effect of turgor pressure. Hence, these must be regulated by a process of self-repair, a stand out feature of biological systems which is often key to the their

remarkable sustainability [157], allowing for design features which are not feasible in human-made structures. Experimentally inducing cuts on the cell wall and studying the healing process will undoubtedly shed more light on this. A plausible method for healing of cracks in this case is that initially, perhaps counter-intuitively, peptide cross-links in the vicinity of the crack tip are cleaved by hydrolysis, which as our model explained, can act to locally hike the tearing energy and arrest the progress of the crack. Then wall material is inserted to repair the crack or to apply a mechanical force to close the crack. Since MreB directs peptidoglycan insertion [49], it naturally will play an important role in the crack repair process. In fact, it has been proposed that the observed MreB patch propagation in the circumferential direction is due to stable circumferential propagation of small gaps in the anisotropic sacculus [158]. The model studied in this chapter paves the way for more detailed work, leading upto a precise study of the mechanism by which cracks on the cell surface are healed even as the cell is growing. Such a mechanism will be fundamental to the survival of the cell and an understanding of this will require a comprehensive blend of experimental, computational and theoretical techniques, which can then be leveraged to design new age antibacterials.

Chapter 3

Modelling heterogeneities in the cross-linked bacterial sacculus

3.1 Introduction

Biological structures are some of the most sophisticatedly engineered materials, whose design principles continue to lend ideas for solving common place as well as esoteric engineering riddles [57, 159, 160]. A pervasive feature of the design of several biological materials is the presence of disorder in their ultrastructural components [161, 162]. However, this cannot be termed as mere accident in light of the often pivotal role played by the disordered fine structure of several key biological materials. Numerous interesting examples of this phenomena can be given, including the role of non-identical molecular motors in actomyosin contractility [163] and the optimized hierarchical structure with highly irregular setup of bone resulting in remarkable orders of toughness and stiffness [161, 164]. The PG mesh also exhibits disorder that is evident in its ultrastructure- this includes the length distribution and orientation of glycan strands and location and degree of cross-linking across the cell wall [10, 11, 14, 42, 140]. Nonetheless, the relevance of these features of disorder

on the mechanical properties of the cell wall has not been well studied, even as it can shed light on a number of experimental observations of the cell wall. In Chapter 2, we explored the mechanical effect of length distribution of the glycan strands and had shown how terminally cross-linked smaller length glycan strands can enhance the toughness of the cell wall, giving an explanation of experimental observations of the presence of shorter length glycan strands and the preference for cross-linking to happen at the ends of the glycan strands [10, 11].

The remodelling process of the cell wall, with the cleaving of older cross-links under the action of hydrolases, incorporation of new cell wall material into it and the consequent formation of cross-links, results in the presence of newer cross-links as well as hydrolase degraded older cross-links in the cell wall. While the exact mechanical effect of hydrolases on the peptide cross-linkers is unclear, this effect can result in the lowering of rupture strength of the bond or lowering of the stiffness of the bond or both. The presence of heterogeneities in the mechanical properties of the cross-linkers is further evidenced by experimental observations in Ref. [14], where isolated cell wall fragments subjected to sonication showed an immediate drop in the degree of cross-linking that persisted even as the structure remained intact, before becoming relatively constant after a period of time. This suggests that the cross-linkers in the cell wall act in a heterogeneous manner under loading, due to differences in their elasticity and rupture strengths. A very natural question then is to understand effect of the variability in the mechanical properties of the cross-linkers, specifically their strength and elasticity, on the bulk mechanical response of the cell wall. Motivated by this and as a first step, here we explore a spring system, in which we incorporate variability in both the spring constant of the constituent springs as well as their rupture strengths and study the response of the system to shear loading. Using analytical methods and computer simulations, we derive the force extension relation and show that in general wider variability in the elasticity of springs can ensure more robust resistance to failure but it also lowers the load

capacity whereas lower variability results in a more brittle response to loading even as the load capacity increases. Our analysis suggests that a possible mechanism for hydrolytic action to act on the cross-linkers in a safe manner while ensuring sufficient load bearing ability is by maintaining high order of variability in the spring constants while limiting the variability in the rupture strengths. We then examine a step wise loading regime which allows us to exhibit a quasi-brittle to brittle transition as the load per step increases. This transition, which is a feature that seems universal in systems which have inhomogeneities built into their ultrastructure, has been observed in other natural materials, e.g. snow [15] and can be useful tool to experimentally detect such inhomogeneities present in the system. This chapter is based on work published in reference [108].

3.2 Model Description

Drawing inspiration from the cross-linked mesh like structure of peptidoglycan in the bacterial cell wall, we study an appropriate spring system. Indeed, the cell wall in general and the peptide cross-linkers in the PG network have been modelled as springs in several works and have proved to a very useful tool to gain insight into the mechanical structure of the cell wall. For instance, Boulbitch et al. [132] used a spring model of the cell wall to estimate the elastic modulus of the PG network. Belgrave and Wolgemuth [165] considered a mechanochemical model to explain the dependence of cell length and cross-linking on the replication rate in case of *E.coli*, in which the peptide cross-linkers were modelled as linear springs. In Misra et al. [166], the multi-layered structure of the Gram positive bacteria *B.subtilis* was modelled as a spring network, which was then used to analyse the mechanical consequences of cell wall turnover in such cells and in particular, highlighted the importance of hydrolysis in driving cell elongation. In Ojkic et al. [167] the forespore engulfment process was studied in case of *B.subtilis* with a biophysical model of the cell wall

in which the peptide cross-linkers were modelled as linear springs and a biophysical mechanism for the creation of a force for engulfment was established.

Here, inspired by the PG network of *E.coli*, we study a system of springs placed in the $X-Z$ plane, consisting of two rigid surfaces, aligned in the X direction and linear springs connecting them, aligned in the Z direction. The rigid surfaces correspond to two adjacent circumferential cross-sections of the peptidoglycan mesh, consisting of axially adjacent, long length glycan strands, while the springs correspond to the cross-linkers joining the two glycan strands (Fig. 3.1). The number of springs connecting the upper and lower surface, denoted N, is determined by the degree of cross-linking present in the peptidoglycan mesh, which we estimate to be around 1000, in accordance with observed degree of cross-linking of $\sim 30\%$ for *E.coli* [10]. Therefore, we take $N = 1000$ in all the simulations. Further, since glycan strands are an order of magnitude more stiff than the peptide bonds [9], for simplicity we assume that upper and lower surfaces are rigid with no local deformations caused by exerted forces. The springs in the system are taken to be linear, with finite rupture strength, which limits the force that a spring can endure before rupturing. We encode variability in the system by taking values of the spring constants and the rupture strengths of the springs from an appropriate joint probability distribution over the region $[k_1, k_2] \times [f_1, f_2]$ with the upper limits f_2 and k_2, which for illustrative purposes we fix to be equal to 1. Our aim is to tune the range of variability by altering the values of f_1 and k_1 and to see the possible effect on the response of system to loading. In our model, the newly formed cross-links correspond to springs which are stiffer and have higher rupture strengths while older cross-links under effect of hydrolases and mechanical stress, are taken to be relatively weaker and less stiff. Therefore, to tune the range of variability in our model, we vary the values of f_1 and k_1 while keeping f_2 and k_2 fixed. We note that our theoretical setup is independent of the values of the upper limit and our results will not change qualitatively when a change is effected in the values of the upper limit.

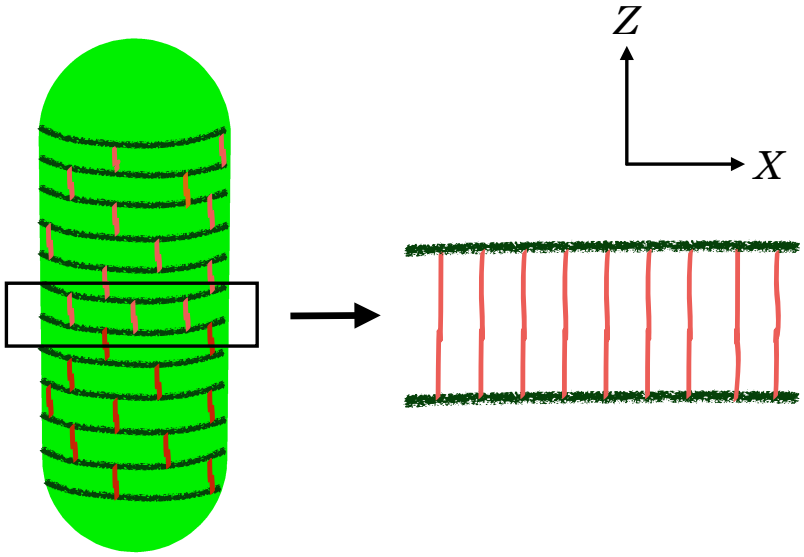

Figure 3.1: The peptidoglycan (PG) mesh in *E.coli* cell wall has stiff glycan strands aligned roughly in the circumferential direction, crosslinked by short peptide bonds. This mesh can be visualised as an ensemble of stiff interfaces and linear springs.

In this chapter, we study shear loading of the spring system. As mentioned before, purified cell wall fragments of *E.coli* have been subjected to sonication [14], a method of cell disruption acting by shear deformation [168] (in general, shearing is a standard and successful method for performing cell disruption experiments [169]). In our case, the upper surface is displaced by application of force while the lower surface is kept fixed (Fig. 3.2). For simplicity, we assume that adjacent springs maintain the position of their link with the upper and lower surfaces, upto their rupture, ensuring that no sliding motion of the springs occurs. In this case, the elongation is the same for every spring, since the displacement of the point of contact of each spring on the upper surface due to the application of the force, will be the same (equal to displacement of the upper surface). We also take all springs in the system to have the same rest length, equal to the distance between the upper and lower surface (corresponding to the inter-glycan spacing and denoted as l, see Fig. 3.2). In general, though, it is possible that the peptide cross-linkers in the peptidoglycan sacculus have variable rest lengths, which can potentially induce interesting phenomena, for

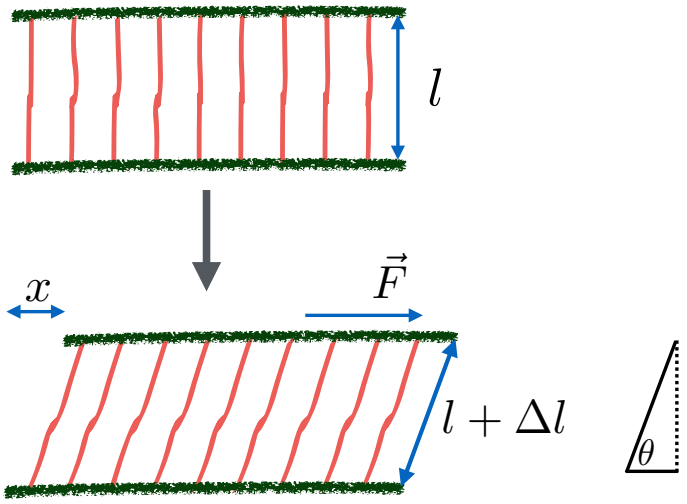

Figure 3.2: Schematic representation of spring system considered. Two adjacent surfaces at distance l from each other joined by N linear springs subjected to shear displacement x. This results in an extension Δl in each spring, with each spring at an angle θ to the lower surface, given by $\tan\theta = l/x$.

instance emergence of residual stress in the system due to mismatch of the rest lengths of the cross-linkers with inter-glycan spacing. This, and yet other modes of heterogeneity in the peptidoglycan sacculus, will be addressed in future work.

3.2.1 Single spring under shear load

We first write down the equations for a single spring with spring constant k and rupture strength f, under similar shear loading as described above. In general, the system can be loaded in two ways- force controlled loading and displacement controlled loading.

For force controlled loading, we assume that a force F is exerted on the upper surface, causing a displacement x of the upper surface and resulting in a stretching of the spring by Δl. The force in the direction of spring elongation is then given by $F_\theta = k\Delta l$. Noting that $\sin\theta = \frac{l}{l+\Delta l}$ and using force balance, we get

$$\frac{F}{kl} = \left[\frac{1}{\sin\theta} - 1\right]\cos\theta \tag{3.1}$$

which gives us a polynomial equation for $\sin\theta$ as

$$R^2 \sin^2\theta = (1 - \sin\theta)^2(1 - \sin^2\theta) \tag{3.2}$$

with $R = F/(kl)$. In our case, since $0 < \theta < \frac{\pi}{2}$, we have $0 < \sin\theta < 1$ and it is then easy to see that Equation 3.2 has a unique solution. So, solving for $\sin\theta$ using Equation 3.2, we can calculate the displacement x in the X-direction as,

$$x = \sqrt{\left(\frac{l}{\sin\theta}\right)^2 - l^2} \tag{3.3}$$

and the shear strain in then given by $\epsilon = x/l$. In case of displacement controlled loading, a displacement x is given to the upper surface keeping the lower surface intact. The extension Δl of the spring is given by

$$\Delta l = \sqrt{l^2 + x^2} - l \tag{3.4}$$

The force F inducing the extension x on the upper surface is given as

$$F = F_\theta \cos\theta = k\Delta l \frac{x}{l + \Delta l} \tag{3.5}$$

Here, we carry out a study of displacement controlled loading of the spring system since typically displacement can be measured in an easier and more precise manner.

3.2.2 Constitutive Behaviour of Spring System

We now consider the case of the spring system, undergoing displacement controlled shear loading (Fig. 3.2), having N springs, with spring constants k_i, for $i = 1, 2, .., N$, where N is the total number of peptides between two interfaces. The effective spring constant of the N parallel springs is -

$$k = k_{eff} = \sum_{i=1}^{N} k_i \tag{3.6}$$

The rupture strength of the springs is denoted f_i, $i = 1, 2, ..., N$. Note that since the shear strain is the same for all (intact) springs, we can calculate the longitudinal elongation of each spring Δl as in Equation 3.4 and thus the force on the i^{th} spring is

$$\sigma_i = k_i \Delta l \tag{3.7}$$

For all springs i for which σ_i exceeds the rupture strength f_i, the spring breaks. The force being exerted in the X-direction on the system is then given by

$$F = \sum_{\text{intact springs}} \frac{\sigma_i x}{\sqrt{l^2 + x^2}} \tag{3.8}$$

which describes the constitutive behaviour of the bundle.

Consider now the special case where the springs all have same spring constant k, the force on all springs is the same, $\sigma = k\Delta l$, when a displacement x is given to the upper surface with Δl as in Equation 3.4. Further assuming that all the springs have the same rupture strength f, the force on the system is given by $F_x = N\sigma x/\sqrt{l^2 + x^2}$, when $\sigma < f$ and the system collapses when σ exceeds f. However, as mentioned above, it has been observed that cell wall fragments of *E.coli* when subjected to

sonication, show an immediate drop in the degree of cross-linking, during which the cell wall structure remains intact [14]. This is however at odds with the behaviour that a system of springs with all springs having same spring constant and rupture strengths exhibits under shear deformation, so we rule out this case and assume that the values of the spring constants and the rupture strengths displays some measure of variability.

To probe the effect of statistical variability in the elasticity and rupture strengths of the springs, we assume that the springs in the system are assigned the values of their respective spring constants and rupture strengths from a joint probability distribution, denoted p. So, in particular, the fraction of springs with spring constant in the interval $[a, b]$ and rupture strength in the interval $[c, d]$ is

$$\int_a^b \int_c^d p(k, f) dk df \tag{3.9}$$

Suppose now that a displacement x is imposed on the upper surface keeping the lower surface fixed. The extension in any spring is given by Δl, as given in Equation 3.4. Since only those springs will survive whose spring constant k and rupture strength f satisfy $k\Delta l < f$ (Fig. 3.3), in other words springs whose rupture strength is more than the current load, so the fraction of surviving springs at given extension x is

$$\frac{N_s}{N} = \iint_{\{(k,f)\,:\,k\Delta l<f\}} p(k, f) dk df \tag{3.10}$$

where N_S denotes the number of surviving springs. So, we have

$$F_\theta = N\Delta l \iint_{\{(k,f)\,:\,k\Delta l<f\}} kp(k, f) dk df \tag{3.11}$$

and then the force extension relation is given by $F = F_\theta \cos\theta = F_\theta x/(l + \Delta l)$ as in Equation 3.5. We note here that in our spring model, the springs, which

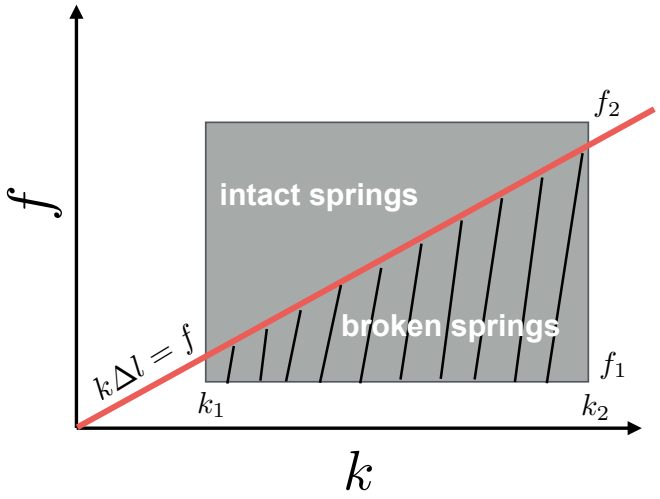

Figure 3.3: The joint probability distribution of the values of spring constants and rupture strengths of the constituent springs is distributed on $[k_1, k_2] \times [f_1, f_2]$. When a shear displacement x is applied to the system, resulting in spring extension Δl, the fraction of broken springs are those whose spring constant and rupture strength lie in the shaded region, below the line $k\Delta l = f$.

represent peptide cross-linkers, have been taken to be linear. However, one can study models in which the cross-linkers follow nonlinear force extension relations by suitably modifying our theoretical framework, though this complication is not studied here.

3.2.3 Simulation details

We carry out computer simulations to compare with and confirm the theoretical framework laid out in the previous section, for understanding the effect of variability in the material properties of the springs. Specifically, for a given spring system, consisting of N springs denoted by $i = 1, 2, .., N$, the i^{th} spring is assigned a tuple (k_i, f_i), where k_i is its spring constant and f_i denotes its rupture strength. To study the effect of variability on the mechanical properties of the system, values (k_i, f_i) are drawn randomly from appropriate joint probability distribution for every i. Given

shear displacement x, spring extension Δl is calculated using Equation 3.4 and the force σ_i on the i^{th} spring is then calculated using Equation 3.7. If $\sigma_i > f_i$, then the spring is considered ruptured and its spring constant k_i is assigned value 0. The force extension relation is then calculated using Equation 3.8. The force extension relation and other simulations in the text are obtained by averaging over 100 realizations in each case.

3.3 Results

We now study the effect that the variability in the spring constants and rupture strengths has on the constitutive behaviour of the bundle. We first consider the case where the distributions of the spring constants and rupture strengths of the springs in the system are taken to be independent.

3.3.1 Effect of Variability on Constitutive Behaviour

Since the distributions of the spring constants and rupture strengths are taken to be independent, so the joint probability distribution $p(k, f)$ (see Equation 3.9) will decompose as product of the marginal distributions p_1 and p_2, giving $p(k, f) = p_1(k)p_2(f)$. We analyse the case where the values of the spring constant and the rupture strength come from uniform distributions. So, with values of the spring constant and the rupture strength lying in $[k_1, k_2]$ and $[f_1, f_2]$ respectively, we get that

$$p(k, f) = p_1(k)p_2(f) = \frac{1}{(k_2 - k_1)(f_2 - f_1)} \tag{3.12}$$

To compute the force extension relation, we note that in this case, the integral in Equation 3.11 can be evaluated as follows- we define $\eta = \min(\max(k_1\Delta l, f_1), f_2)$.

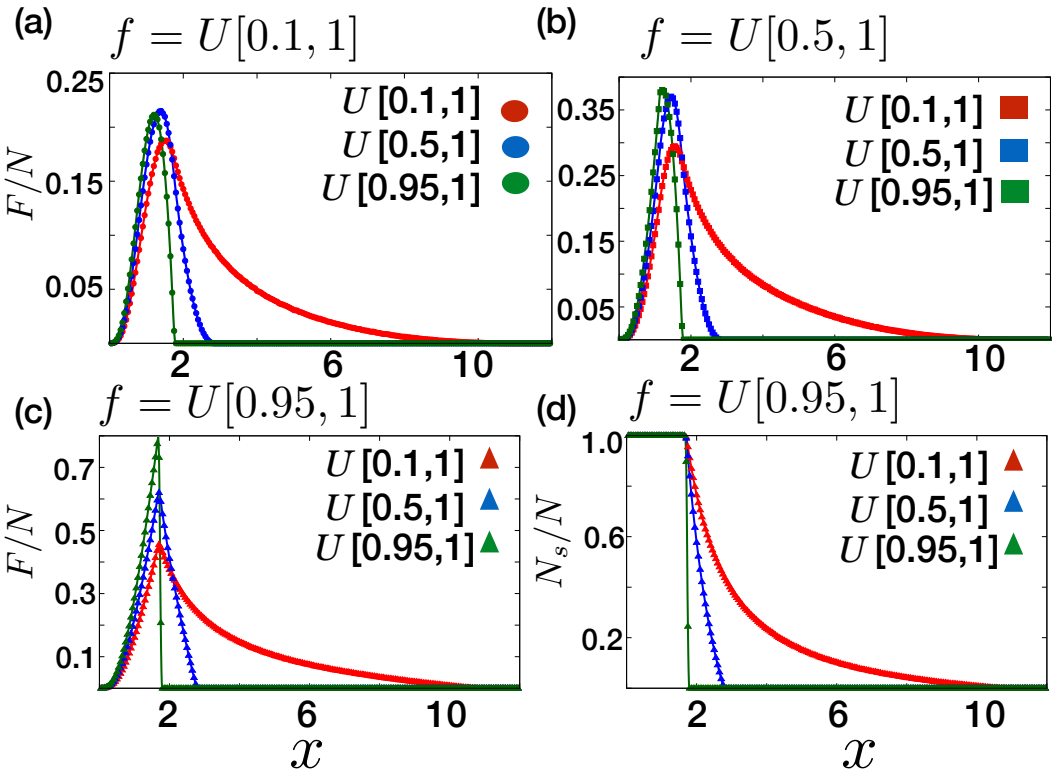

Figure 3.4: Force-extension curve with distribution of f taken in (a) $f = U[0.1, 1]$, in (b) $f = U[0.5, 1]$ and in (c) $f = U[0.95, 1]$. In each case, three plots are drawn with probability distribution of k taken as $U[0.1, 1]$, $U[0.5, 1]$ and $U[0.95, 1]$. (d) Fraction of surviving springs is drawn as a function of displacement for $f = U[0.95, 1]$. We compare the curve derived analytically from Equation 3.10 and Equation 3.15 (solid lines) and simulations (solid points) for all the cases. We have taken $N = 1000$ and $l = 1$. In all the graphs, we note that the system with k distribution $U[0.95, 1]$ collapses first while system with k distribution $U[0.1, 1]$ collapses last.

Then we have

$$\iint_{\{(k,f)\,:\,k\Delta l \le f\}} kp(k,f)dkdf = \int_{\eta}^{f_2} df \left(\int_{k_1}^{\min(k_2, f/\Delta l)} kp(k,f)dk \right) \tag{3.13}$$

which gives

$$F_\theta = N\Delta l \int_{\eta}^{f_2} df \left(\int_{k_1}^{\min(k_2, f/\Delta l)} kp(k,f)dk \right) \tag{3.14}$$

and the force extension relation is then

$$F = N\frac{x\Delta l}{l+\Delta l}\int_{\eta}^{f_2} df\left(\int_{k_1}^{\min(k_2, f/\Delta l)} kp(k,f)dk\right) \tag{3.15}$$

with Δl given as in Equation 3.4 as a function of the shear displacement x.

In Fig. 3.4, using Equation 3.15 and computer simulations, we compute the force extension curve and the surviving fraction of springs as a function of the shear extension x, acting on a fully intact bundle, with the values of spring constants and rupture strengths of the springs in the system drawn from uniform distributions over different intervals. In all cases, simulations show excellent agreement with the theoretical computations. We observe a very interesting contrast- in each case, the maximum load that the bundle takes, given by the maxima of the force-extension curve, is highest in the case when springs in the bundle are the stiffest, given in Fig. 3.4 when the spring constants are uniformly distributed on $[0.95, 1]$, while on the other hand, the extension at which the bundle fails, is maximized in the case when the values of the spring constants is distributed over a wider range, which in Fig. 3.4 is given by $[0.1, 1]$, while bundle with stiffest springs show a brittle response to the shear loading. This suggests that while the load bearing ability of the system is enhanced by the presence of stiff springs, the toughness of the system or the resistance of system to mechanical failure is enhanced by the presence of heterogeneities in the system. This also highlights the standard engineering problem of fabricating materials with high degrees of load bearing ability and toughness, something that nature seems to excel in, with biomaterials like bone and nacre exemplifying this property [62, 161]. Thus, an ideal scenario to ensure high load bearing ability and resistance to mechanical failure is to increase the variation in the value of spring constants while keeping the rupture strength high with very little variation. This suggests that a possible mechanism for hydrolytic action on the cross-linkers could result in ensuring wider variability in the elasticity of the cross-linkers while showing little effect on their rupture strengths, so as to secure

the viability of the structure which has to bear load even as it is being remodelled continually. We now estimate the shear displacement x_i at which spring breakage is initiated and x_f at which the system fails. We observe from Fig. 3.4(d) that x_i remains unchanged even as the variability in the values of spring constants is changed. This suggests that x_i is independent of k_1. Similarly, we also observe from Fig. 3.4(a), Fig. 3.4(b), Fig. 3.4(c) that x_f stays the same in all three cases once the distribution of spring constant is fixed, which suggests that it is independent of f_1. To understand this interesting phenomena, we estimate x_i and x_f as follows- note that the ratio of rupture strength and the spring constant f/k for springs in the system takes value in the range $[f_1/k_2, f_2/k_1]$, since the joint distribution p is supported on $[k_1, k_2] \times [f_1, f_2]$. Therefore, breaking of springs is initiated when the displacement ensures that the spring elongation $\Delta l \approx f_1/k_2$ and system failure occurs when $\Delta l \approx f_2/k_1$. We can then estimate the displacement x_i at which spring failure is initiated and the displacement x_f at which the system collapses using Equation 3.4 which gives

$$x_i \approx \sqrt{(l + (f_1/k_2))^2 - l^2} = \frac{\sqrt{(2lk_2 + f_1)f_1}}{k_2} \tag{3.16}$$

and similarly we have that the bundle fully breaks when $\Delta l = f_2/k_1$. So, then we have

$$x_f \approx \sqrt{(l + f_2/k_1)^2 - l^2} = \frac{\sqrt{(2lk_1 + f_2)f_2}}{k_1} \tag{3.17}$$

It follows from Equation 3.17 that x_f depends on the weaker springs that have very high rupture strength, with the extreme case given by springs having spring constant k_1 and rupture strength f_2. It is independent of the values f_1 and k_2, which represent the values for the stiffest springs which have the lowest rupture strength. These values however determine x_i (see Equation 3.16). Since the displacement is the same for all springs, springs with high stiffness and low rupture strength

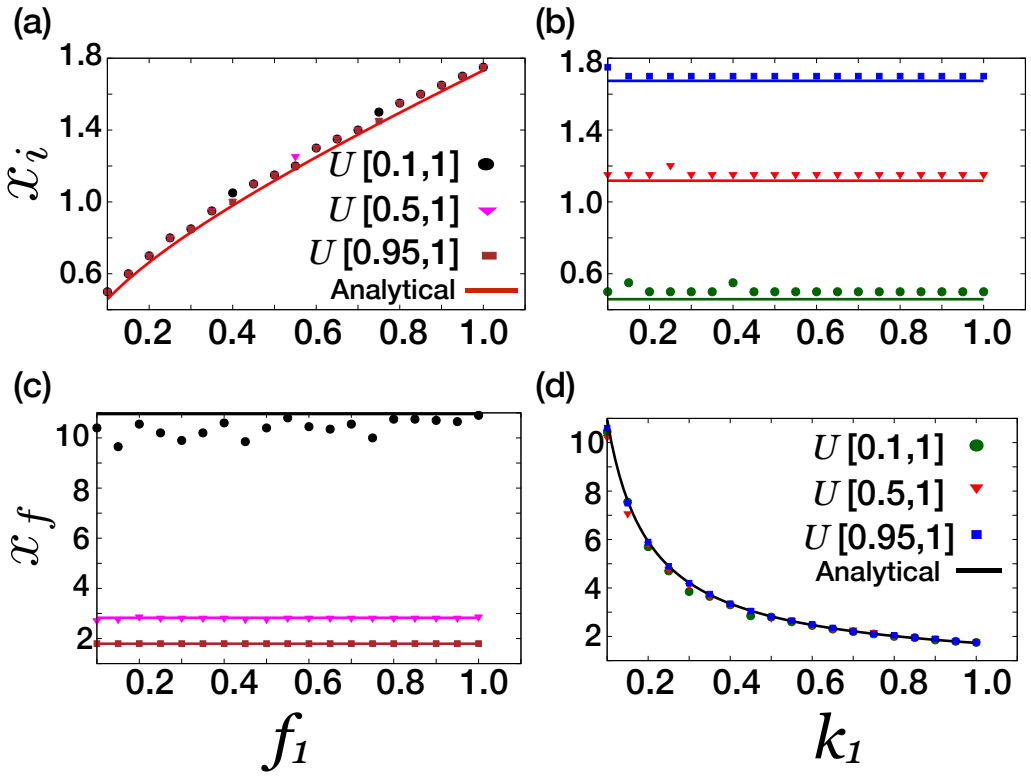

Figure 3.5: In (a) and (b), displacement at which spring rupturing is initiated, x_i, is plotted as a function of f_1, for different distributions of k_1 as labelled and as a function of k_1, for different distributions of f_1, respectively, using Equation 3.16 (solid line) and simulations (points). In (c) and (d), displacement at which system fails, x_f, is plotted as a function of f_1 for different distributions of k_1 and as a function of k_1, for different distributions of f_1 as labelled, respectively, using Equation 3.17 (solid line) and simulations (points).

are the first to rupture. To check this, we perform simulations of bundle of 1000 springs with values of spring constant derived from the distribution $U[k_1, 1]$, for varying k_1, while the rupture strength of the springs is derived from fixed uniform distribution, to compute the value of x_i (plotted in Fig. 3.5(b) as a function of k_1) and x_f (plotted in Fig. 3.5(d) as a function of k_1). We also perform simulations keeping the distribution of spring constants to be fixed and the rupture strength distribution to be $U[f_1, 1]$ with varying f_1 to compute the values of x_i (plotted in Fig. 3.5 (a) as a function of f_1) and x_f (plotted in Fig. 3.5(c) as a function of f_1). In all cases, the simulations results agrees well with the analytical results. We observe from Fig. 3.5(b) that the value of x_i is approximately constant in all three cases as

k_1 varies, in good agreement with Equation 3.16, while increasing with value of f_1 approximately linearly. On the other hand, the value of x_f remains constant in all three cases as f_1 varies, as in Fig. 3.5(c), while showing a power law dependence on k_1. This, in particular, reiterates that the ideal scenario to ensure high value of both x_f and load capacity arises when k_1 has a low value while the value of f_1 is high. This is because a low value of k_1 ensures that x_f has a high value. But the value of x_f remains relatively constant as f_1 changes. Therefore, a high value of f_1, while keeping x_f unchanged, limits the variability and hence, increases the load capacity. To understand this effect, we can make a rough estimation of the shear displacement at failure in case of the bacterial cell wall as the elasticity of the cross-linkers vary- with the spring constant of peptide cross-link estimated as $k_2 \sim 10^{-2} N/m$ [132] and estimating the rupture strength of the cross-link as $f_2 = \sqrt{2Ek_2}$ where $E \sim 300 kJ/mol$ is the dissociation energy of the covalent cross-linking bond, we get $x_f < 10nm$ when there is very little variation with $k_1 \approx k_2$ while $x_f \sim 10^2 nm$ when there is variation with $k_1/k_2 \approx 0.1$. This calculation, though only a very rough estimation, shows how effectively variation in the elasticity of the cross-linkers can offer high degree of protection from mechanical failure.

3.3.2 Loading Regimes

We now impose specific loading regimes on the spring system and study its response. Specifically, given displacement $x(t)$ imposed on the upper surface as a function of time t, we compute the fraction of surviving springs as a function of time, which we denote $u(t) = N_s(t)/N$. We explore two loading regimes- (a) where $x(t)$ increases linearly with time before becoming constant and (b) where $x(t)$ increases linearly and then drops to 0 and this cycle is continued, ensuring each time that the load peaks at a level higher than the previous cycle (Fig. 3.6(a) and Fig. 3.6(c)). We note that the response in the first case is an almost immediate drop in the fraction of surviving

springs $u(t)$, which then stabilizes when the loading itself stabilizes. We note the similarity in the response to this loading regime to experimental observations in Ref.[14] (see Fig. 6(a) therein), where it was observed that the degree of cross-linking of isolated *E.coli* sacculi subjected to sonication first decreases monotonically and then becomes constant as a function of time. In the second case, the response to the load results in a calibrated fall in the fraction of surviving springs. When $x(t)$ is increasing, $u(t)$ registers a fall but when $x(t)$ drops to 0 and subsequently increases, $u(t)$ remains constant till $x(t)$ goes beyond the previous peak whence $u(t)$ starts to drop again and this cycle continues.

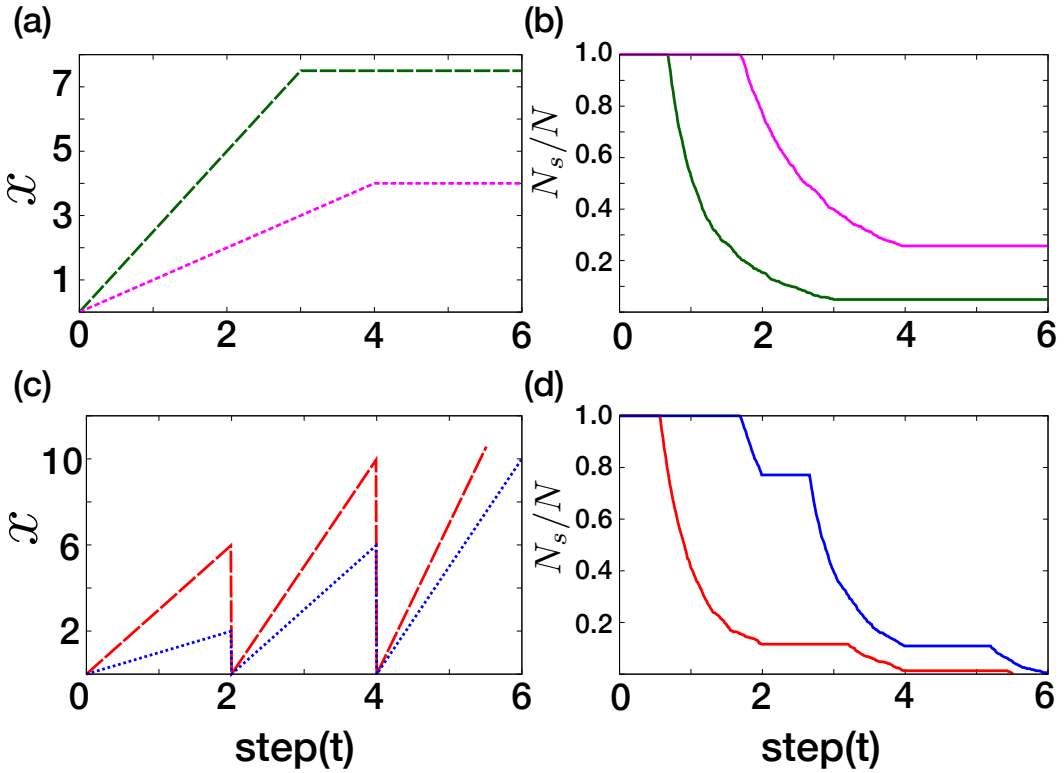

Figure 3.6: In (a) and (c), loading regimes $x(t)$ are plotted and the corresponding response of the system to these loading regimes in form of the fraction of surviving springs is plotted as a function of time in (b) and (d), respectively, with range of k values taken from $U[0.1, 1]$ and f values taken from $U[0.95, 1]$. We note that in each case, for loading regime with higher loads, spring breakage, that is $N_s/N < 1$, is initiated faster.

We now consider another loading regime of the spring system, by stepwise increase of the shear displacement. In other words, loading is provided in discrete steps of

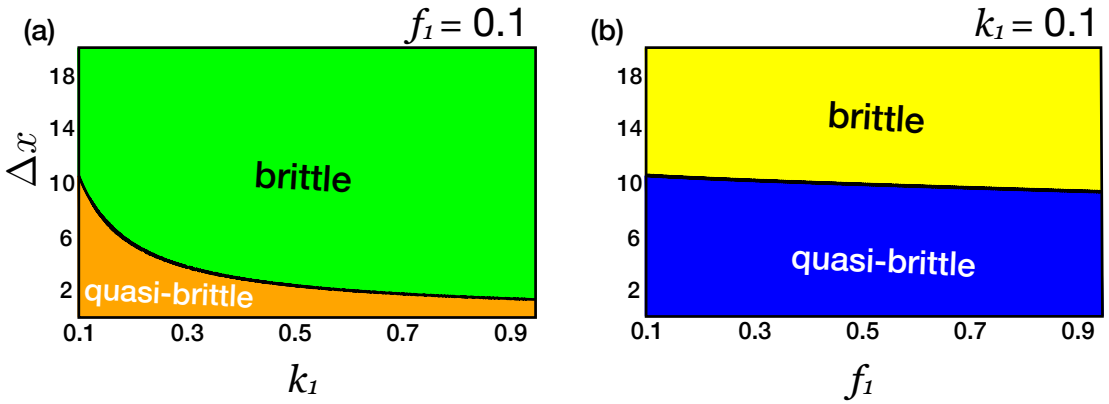

Figure 3.7: Phase diagram of the spring system with uniformly distributed rupture strength (f) and spring constant (k), showing a quasi-brittle to brittle transition. (a) Phase diagram in the $\Delta x - k_1$ plane for fixed $f_1 = 0.1$, (b) in $\Delta x - f_1$ plane for fixed $k_1 = 0.1$.

shear displacement, Δx in each step. We estimate the number of steps to failure in this case. As before, the spring constant and the rupture strength derive values from joint distribution $p(k, f)$ supported fully on $[k_1, k_2] \times [f_1, f_2]$. The number of steps to failure, denoted $n_f(x)$ is given by

$$n_f(\Delta x) = n_1(\Delta x) + n_b(\Delta x) \tag{3.18}$$

where n_1 denotes the number of steps needed for first failure to happen and n_b denotes the number of steps from first failure till complete failure.

We recall that failure of springs starts to happen when $\Delta l \approx f_1/k_2$ and all springs would have failed when $\Delta l \approx f_2/k_1$ (see Fig. 3.3). This gives us the equation

$$n_1^2(\Delta x)^2 \approx \left(\frac{f_1}{k_2} + l\right)^2 - l^2 \tag{3.19}$$

which gives

$$n_1 \approx \frac{\sqrt{\left(\frac{f_1}{k_2} + 2l\right)\frac{f_1}{k_2}}}{\Delta x} \tag{3.20}$$

and similarly, we have

$$n_f^2(\Delta x)^2 \approx \left(\frac{f_2}{k_1} + l\right)^2 - l^2 \Rightarrow n_f \approx \frac{\sqrt{\left(\frac{f_2}{k_1} + 2l\right)\frac{f_2}{k_1}}}{\Delta x} \tag{3.21}$$

We also define $n_b(\Delta x) = n_f(\Delta x) - n_1(\Delta x)$. The response of the system to shear loading is brittle if all springs break in a single step while the response is quasi-brittle in the case when the breaking process occurs over multiple steps. In other words, using notation of Equation 3.18, the response to shear loading is brittle if $n_b < 1$ and the response is quasi-brittle if $n_b \geq 1$. In Fig. 3.7, we plot the phase diagram of the system in various cases - in Fig. 3.7(a), the phase diagram is in the k_1-Δx plane while keeping f_1 fixed and in Fig. 3.7(b), the phase diagram is in the f_1-Δx plane while keeping k_1 fixed. We note that in each case, a quasi-brittle to brittle transition is evident- for sufficiently low values of Δx, the response is quasi-brittle while for high values of Δx, the response is brittle. Now, in case each Δx load is given in fixed Δt time, then the load rate $y = \Delta x/\Delta t$ can determine the material response- if y is high, then the response is brittle as Δx is high as well, similarly, if y is low, then Δx is low which results in a quasi-brittle response. This phenomena has been observed to happen in snow [15] and has been studied in [170] using an FBM model that is similar to our model but less general, in that all the springs in the system have a fixed spring constant k. In general, this type of quasi-brittle to brittle transition can be considered as a signature of the presence of heterogeneities in the system.

3.3.3 Correlated elasticity and rupture strength

We now study the spring system for which the values of the spring constant and the rupture strength of the constituent springs are correlated. For simplicity, we assume that the values of the spring constant and the rupture strength are derived from the

same interval $[a, b]$, though we note that our results will hold more generally. We consider first a system with positively correlated k and f values, with springs having high rupture strength having relatively higher spring constants as well. Fixing $\epsilon > 0$, we define the conditional probability distribution of spring constant conditional on the rupture strength $p_{k|f} = U[\xi_f, \kappa_f]$, where U denotes the uniform distribution on the interval $[\xi_f, \kappa_f]$ with $\xi_f = \max(a, f - \epsilon)$ and $\kappa_f = \min(f + \epsilon, b)$. Then, with p_0 denoting the probability distribution of the rupture strength and taken as $U[f_1, f_2]$, we have the joint distribution as

$$p(k, f) = p_{k|f}(k)p_0(f) = \frac{1}{(f_2 - f_1)(\kappa_f - \xi_f)} \tag{3.22}$$

Unlike the previous case, where the spring constants and the rupture strengths of the springs in the system were taken to be independent with the distribution spread fully on the rectangle $[k_1, k_2] \times [f_1, f_2]$, in this case, the probability distribution is supported on a strip of width $\sim 2\epsilon$ around the diagonal $(x, x), a \leq x \leq b$ of the box $[a, b] \times [a, b]$. We observe a markedly brittle response to displacement controlled shear loading, as shown in Fig. 3.8, with bundle failure occurring very sharply similar to the case where the spring constants show very little variability while contrasting acutely with the case where the spring constants are spread widely, as in Fig. 3.4(a).

However, the situation is different when we consider a negative correlation between the k and f values. We again fix an interval $[a, b]$ and $\epsilon > 0$. But we now take the distribution $p_{k|f} = U[\rho_f, \mu_f]$, with $\rho_f = \max(a, a+b-f-\epsilon)$ and $\mu_f = \min(a+b-f+\epsilon, b)$. We then have the joint distribution $p(k, f) = p_{k|f}(k)p_0(f)$, with $p_0 = U[a, b]$. In this case, the values of k and f are distributed in a region of width $\sim 2\epsilon$ around the diagonal $(x, a+b-x)$, $a \leq x \leq b$. In Fig. 3.8(b), we observe that the system displays a markedly quasi-brittle response, comparable to the independent case (Fig. 3.4(a)). In other words, the quasi-brittle response to loading of the system with independent

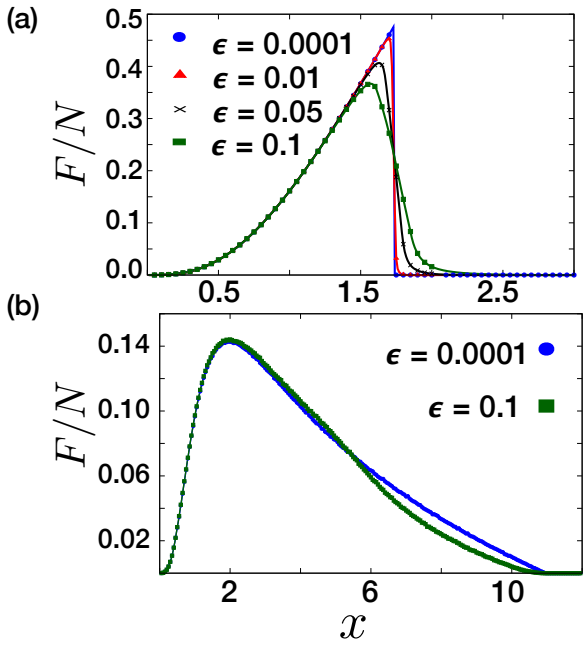

Figure 3.8: Force extension curve for systems with (a) positively correlated and (b) negatively correlated k and f values, ϵ as labelled in inset, distribution of f taken as $U[0.1, 1]$ in both cases, computed using Equation 3.15 (solid lines) and simulations (points).

k and f values can be effectively mimicked by systems with k and f appropriately negatively correlated, even though the support of the values of the spring constants and the rupture strengths of the springs are spread over a much narrower area. To understand this, we note that as the shear displacement is increased, the region $[a, b] \times [a, b]$ in the $k - f$ plane is swept in the anti-clockwise direction by lines of the form $f = k\Delta l$, with the area under the line determining the fraction of springs broken (see Fig. 3.3). In case the values of k and f are negatively correlated, the entire area of $[a, b] \times [a, b]$ has to be swept to cover all the springs. In the positively correlated case, the k and f values are distributed around the diagonal (x, x), so much lesser area has to swept to cover all springs in the system, hence it exhibits a decidedly brittle response. However, while in the positive correlation case the maximum load is greater than the independent case, in case of negative correlation, the maximum load is in fact lower than the independent case. Hence, our analysis suggests that, in general, for ensuring a sufficiently high load capacity and also high resistance to

failure, it can be important that the distributions of k and f of the springs in the system are independent and are supported over a wide region, essentially resulting in a multi-composite structure. For the particular case of the bacterial cell wall, it is therefore plausible that hydrolytic action effects independent distributions of the elastic properties of the peptide cross-linkers, with wide variability in the stiffness and limited variability in rupture strengths, since this has the effect of making the structure both more resistant to failure under to loading and enhances the load carrying capacity.

3.4 Non uniform distributions

So far, we have primarily considered the case with spring constants and rupture strengths of the springs in the system having uniform distribution over appropriate intervals. We now study systems for which the k and f values are independent and follow other distributions. First, we consider the case where the spring constants and the rupture strengths follow Gaussian distributions $N(\mu_0, \sigma_0)$ and $N(\mu_1, \sigma_1)$ respectively. For a random variable following the $N(\mu, \sigma)$ distribution with mean μ and standard deviation σ, it is easy to see that $\approx 99.7\%$ of values lie within a distance of 3σ of the mean μ. We therefore infer that the spring constants and rupture strengths of the constituent springs in the system are essentially distributed in the region $[k_1, k_2] \times [f_1, f_2]$ with $k_1 = \mu_0 - 3\sigma_0, k_2 = \mu_0 + 3\sigma_0, f_1 = \mu_1 - 3\sigma_1, f_2 = \mu_1 + 3\sigma_1$. Given k_1, k_2, f_1, f_2, we solve and get $\mu_0 = (k_1 + k_2)/2, \sigma_0 = (k_2 - k_1)/6, \mu_1 = (f_1 + f_2)/2, \sigma_1 = (f_2 - f_1)/6$. So, we have

$$p(k, f) = \frac{1}{2\pi\sigma_0\sigma_1} e^{-\left[\frac{(k-\mu_0)^2}{2\sigma_0^2} + \frac{(f-\mu_1)^2}{2\sigma_1^2}\right]} \tag{3.23}$$

The force extension relation is then computed using Equation 3.15 (noting that the integral in this case cannot in general be exactly solved, unlike the uniform case

and is therefore numerically approximated) and it is compared with computer simulations of the system as described in Section 3.2.3, in Fig. 3.9. Simulations show excellent agreement with theoretical computations, which demonstrates that our theoretical framework is applicable for spring systems irrespective of the distributions followed by k and f values.

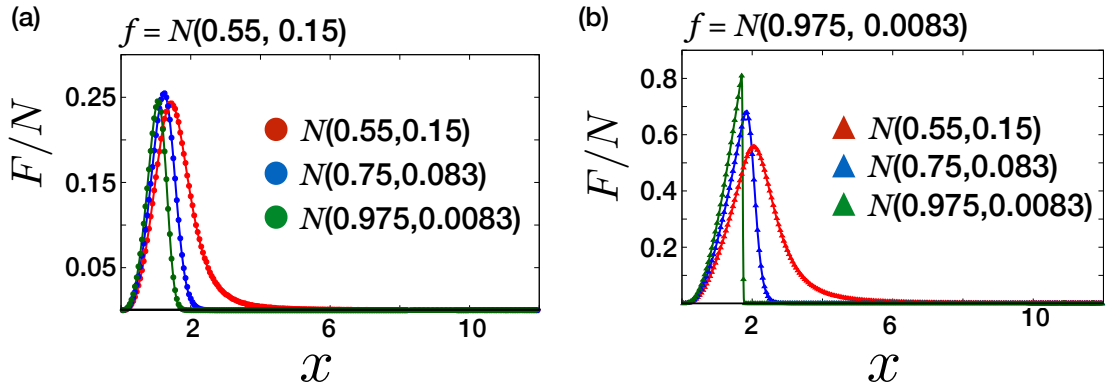

Figure 3.9: Force extension curve for systems with k and f values following independent Gaussian distributions. The f values follow (a) $N(0.55, 0.15)$ and (b) $N(0.975, 0.0083)$ distributions while the distributions of k values are labelled in inset. We compare the curves derived using Equation 3.15 (solid lines) and simulations (points). Note that in both cases, system with k distribution $N(0.975, 0.0083)$ collapses first and system with k distribution $N(0.55, 0.15)$ collapses last.

In this case, we note that 1- the maximum load is always higher in the Gaussian case as compared to the uniform case and 2- the system in this case collapses at a faster rate, with a significant number of the springs having ruptured at shear displacements much lower than x_f. This is because in the Gaussian case the k and f values are strongly concentrated around the mean but in the uniform case the values are spread more evenly. To further highlight this, we also consider systems for which the spring constants follow a left truncated and a right truncated normal distributions, essentially supported in $[k_1, k_2]$, with probability distributions given by

$$p(k) = \delta_{[k_1,\infty)} \frac{\sqrt{2}}{\sigma\sqrt{\pi}} e^{-\frac{(k-k_1)^2}{2\sigma^2}} \tag{3.24}$$

and

$$p(k) = \delta_{[-\infty,k_2)} \frac{\sqrt{2}}{\sigma\sqrt{\pi}} e^{-\frac{(k-k_2)^2}{2\sigma^2}} \tag{3.25}$$

respectively (see Fig. 3.10 (inset)). Here $\sigma = (k_2 - k_1)/3$ and the function $\delta_{[a,b]}(x)$ takes value 1 for $a \leq x \leq b$ and 0 otherwise. In both the uniform and Gaussian cases, wider variability in the k values and limited variability in the f values results in an ideal scenario with a high load carrying capacity and resistance to failure, so we fix this case with f values showing relatively much less variability and following the uniform distribution on a small interval. In Fig. 3.10, we compare the force extension curves with the spring constants having uniform, Gaussian, left truncated Gaussian and right truncated Gaussian distributions. We observe that the maximum load is highest for the right truncated case and is lowest in the left truncated case, implying that the load capacity is higher when the spring constants are concentrated around a higher value. However, while the systems finally fail at same shear displacement x_f for all distributions, the right truncated system fails at the fastest rate and the left truncated system displays a force extension curve that is the slowest to fall, exhibiting substantial quasi-brittle response to loading.

We note here that the main results and conclusions of this study are not dependent on the form of the distributions of the values of k and f, however, the precise shape of the force extension curve will depend on the distributions. In general, the distributions and the range of the k and f values in the peptidoglycan mesh will be influenced by the rate of incorporation of cell wall material (synthesis rate) and the rate at which hydrolases act to facilitate material removal in the cell wall, factors which modulate the growth rate of the cell as well [166, 165]. For instance, uniform distribution of the values of k and f will likely occur under conditions resulting in steady incorporation and removal of cell wall material. On the other hand, a concentration of the k and f values closer to the upper limit of the distribution is probably indicative of a higher rate of synthesis as compared to the rate of hydrolysis

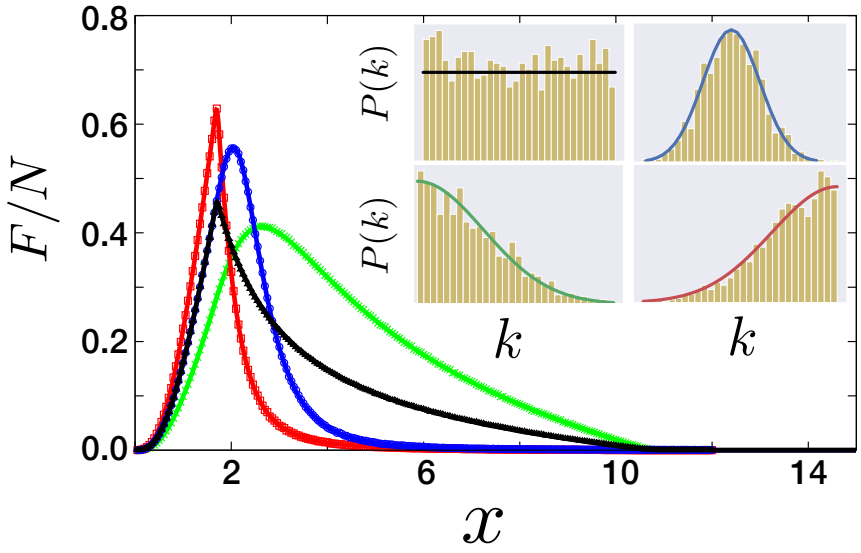

Figure 3.10: Force extension curves for systems with k and f values taken independent, with distribution of f fixed as $U[0.95, 1]$, computed using Equation 3.15 (solid lines) and simulations (points). The k values follow the uniform (black and triangles), Gaussian (blue and circles), left truncated Gaussian (green and lines), right truncated Gaussian (red and squares) distributions, supported on $[0.1, 1]$. The distributions are depicted in the inset.

while a faster rate of hydrolysis might result in a distribution of values concentrated near the lower limit. Since dissimilar growth conditions will likely result in elastic properties of the peptide cross-linkers being differently distributed, our analysis thus suggests that the cell wall adopts disparate constitutive behaviour under varying growth conditions. Another interesting direction in this regard is the possibility of carrying out a form of biological "forensics", to ascertain by carefully analysing constitutive behaviour of isolated cell wall fragments, the conditions undergone by the cell itself during its growth.

3.5 Discussion

In this chapter, inspired by the cross-linked structure of the bacterial cell wall and to understand the effect of variability in the mechanical properties of the peptide cross-

linkers on the structure of the cell wall, we studied the response of a spring system, consisting of several springs joining two adjacent rigid surfaces, to a displacement controlled shear loading. Variability in the mechanical properties of the cross-linkers has been indicated by experimental results on sonication of isolated *E.coli* sacculi [14] and can arise from action of hydrolases on the cell wall, resulting in a distribution of newly formed and degraded cross-links. To incorporate variability into the model, the spring constants and rupture strengths of the springs were taken from an appropriate probability distribution. Laying the condition that the distribution of spring constants and rupture strengths are independent, we computed the force extension curve and observed that higher variability in values of the spring constants resulted in a quasi-brittle response to loading with a higher value of the shear displacement at which the system collapses while lower variability resulted in a much more brittle response, highlighting the standard problem in engineering of ensuring high orders of stiffness and toughness in a material [57]. On the other hand, while the load capacity is enhanced for systems having limited variability in values of rupture strength, the failure displacement remained independent of the lower limit of its distribution. Thus our analysis reflected a viable way for providing a high load bearing capacity and resistance to failure to the system is by ensuring a composite structure with wide variability in value of spring constants and restricted variability in rupture strengths. Since the bacterial cell wall is key to bearing turgor pressure in the cell while being remodelled, with cleaving of cross-links and insertion of newer glycan strands happening continually, maintaining structural integrity under such conditions is critical to the survival of the cell. Our analysis suggests that the action of hydrolases, if resulting in good variability in the elasticity of cross-linkers while showing little effect on their rupture strength, can ensure that the structure remains robust enough to sustain high turgor pressure as well as resist mechanical failure. We also explored a stepwise loading regime which allowed us to obtain a quasi-brittle to brittle transition as the load increases. This transition is a signature

of the presence of heterogeneities in the system and hence, is of much importance for experimental detection of the same.

Here, we have modelled the peptide cross-linkers in the peptidoglycan sacculus as linear springs. Although peptide cross-linkers have often been modelled as linear springs in previous work [119, 132, 165], non-linearity in their force extension relation is plausible. Indeed, simulation work has suggested that their force extension curves may be approximated as a worm like chain (WLC) [121]. We note that our theoretical framework can be generalized to include spring models, in which the springs display a non-linear loading response of the type $F(x) = k_1x + k_2x^2 + ... + k_nx^n$, where each spring will then be parametrized by $(k_1, k_2, ..., k_n, f)$ where f denotes the rupture strength. The values of the parameter will need to be drawn from a multivariate distribution (generalizing the case of bivariate distributions as considered here) to incorporate variability. In this case, the parameter space will be a multidimensional space of the form $S = [k_1^1, k_1^2] \times [k_2^1, k_2^2] \times .... \times [f_1, f_2]$. For a shear loading x which extends any spring by Δl, we can define the space $B = \{(k_1, k_2, ..., f) : f = k_1\Delta l + k_2(\Delta l)^2 + ... + k_n(\Delta l)^2\}$ (analogous to the line $f = k\Delta l$ as depicted in Fig. 3.3) which intersects the space S, which can then be used to recognise the springs which are broken (i.e. springs whose respective parameters lie "below" B in S) and the springs which are intact (i.e. springs whose respective parameters lie "above" B in S). This highlights that even in this non-linear case, a quasi-brittle to brittle transition will occur under a stepwise loading regime as discussed in Section 3.3.2, which thus acts to discern the presence of heterogeneities in the system.

Several theoretical approaches to modelling the cell wall have taken a continuum theory approach [7, 120, 127], which however may not take into account the molecular level architecture and the inhomogeneities inherent in the structure of the cell wall. The peptidoglycan sacculus has a significantly complex structure and in our

simplified model, we have not considered and studied the full range of its design features and their role in ensuring the stability of the cell wall and survival of the cell. Nonetheless, our approach presents a possible first step towards including the inhomogeneities present in the peptidoglycan mesh and its molecular scale architecture in modelling of the cell wall structure and dynamics. In particular, this work anticipates a potentially paradigmatic shift in the coarse grained modelling of the peptidoglycan sacculus by considering variability in the elastic properties of the constituents, leading to a better understanding of the bulk material properties of the sacculus - previous coarse grained models of peptidoglycan have typically assumed uniformity in the elastic properties of glycan strands and peptide cross-linkers [119, 132, 165].

Chapter 4

Molecular Dynamics Simulations

Molecular dynamics (MD) is a computer simulation methodology used to study the time-dependent behaviour of a molecular system, by integrating equations of motion. MD simulations help to predict how constituents in molecular systems will move over time, allowing the derivation of kinetic and thermodynamic properties of interest. Application of molecular dynamics simulations to understand biologically important macromolecules and their complex environment is now extremely common [171]. MD simulations are frequently applied in tandem with experimental procedures such as X-ray crystallography and NMR spectroscopy [172]. MD simulations are also now being widely utilized in drug design by the pharmaceutical industry [173].

MD simulation have become a standard approach for performing many-body calculations on the biomolecular systems of interest. Indeed, with the advent of faster and more powerful computers, MD simulation studies have paved the way for probing the detailed structure and dynamics of such systems at spatial and temporal scales that are outside the scope of existing experimental techniques. However, for this, a good computational model which involves a complete description of the system under study, along with the knowledge of appropriate interaction potential, is necessary. The initial structure of the system could either be obtained from experimental stud-

ies or by molecular modelling techniques. Subsequently, simulations to study such systems can be carried out by utilizing MD methods, which are broadly classified based on the resolution of internal structure chosen to represent the physical system into two families- "atomistic" or "coarse-grained". In the atomistic approach to MD simulations, molecules are represented at the level of atoms, which leads to more realistic representation of the actual system. On the other hand, coarse-grained approaches provide reduced resolution, compared to atomistic models, but are becoming popular when large systems or long simulations are required, in which case atomistic models typically require prohibitively large computing resources [174]. In this thesis, we rely on the atomistic approach to study relevant molecules of interest.

The applicability and accuracy of MD simulations to large biomolecular systems depends on several crucial factors, in particular, system size, simulation times, initial conditions, choice of ensembles, interacting potentials and boundary conditions. As integration of dynamical equations is done numerically, a time step shorter than the fastest possible movement in the molecule has to be used for numerical stability. For atomistic simulations, one time-step is usually between $1-2$ fs (10^{-15}s) (generally, structural changes in biological processes occur at much larger timescales-nanoseconds (10^{-9}s), microseconds (10^{-6}s), milliseconds (10^{-3}s), or even longer). Algorithmic advances, parallelism or the use of graphical processing units (GPUs), along with the advancement of highly scalable simulation packages such as NAMD [175], AMBER [176], CHARMM [177], GROMACS [178] and availability of voluminous database [179] and molecular graphics programs, such as Visual Molecular Dynamics (VMD)[180], have greatly enhanced the performance of MD simulations. In this thesis, we use the NAMD simulation package, which is a parallel molecular dynamics code used extensively for high performance simulation of complex biomolecular systems [175].

We now give a concise description of the MD method and the interacting potential

fields. We also discuss the choice of boundary conditions and calculation of long range interactions, followed by the choice of ensembles in which MD simulations can be performed. We conclude the chapter by briefly describing the computational models of molecules relevant for the work presented in this thesis.

4.1 MD method

Molecular dynamics simulations calculate the time evolution of a molecular system by numerically integrating the system's classical equation of motion. Suppose the system consists of N particles, let m_i be the mass of each particle i, where $i = 1,....N$ and let F_i be the total force acting on particle i at time t. Newton's equation of motion for each particle i can then be written as

$$m_i \frac{d^2 r_i}{dt^2} = m_i \ddot{r}_i = F_i \tag{4.1}$$

The interaction law is specified by the potential $U(r_1, ...r_N)$, which represents the potential energy of the N interacting atoms as a function of positions $r_i = (x_i,y_i,z_i)$ for each particle i. Given the potential, the force acting upon the i^{th} atom is determined by the negative gradient of the potential energy function with respect to atomic positions

$$F_i = -\nabla_{r_i} U(r_1, ...r_N) \tag{4.2}$$

The potential energy is a function of the position of all the particles in the system, in other words U is defined on vectors in $\mathbb{R}^{3N}$. Due to the complicated nature of this function, it is hard to analytically solve the equations of motion.

4.1.1 Integration Algorithms

In molecular dynamics, numerically integration of the equations is frequently carried out using the Verlet algorithm [181]. In this algorithm, two Taylor series expansions are used for $r_i(t)$, denoting the position of each particle i at time t, one forward and one backward in time. Denoting $\dot{r}_i = v_i(t)$ and $\ddot{r}_i = a_i(t)$ to be the velocity and acceleration, we have

$$r_i(t+\delta t) = r_i(t) + v_i(t)\delta t + \frac{1}{2!}a_i(t)\delta t^2 + \frac{1}{3!}\dddot{r}_i\delta t^3 + \mathcal{O}(\delta t^4) \tag{4.3}$$

$$r_i(t-\delta t) = r_i(t) - v_i(t)\delta t + \frac{1}{2!}a_i(t)\delta t^2 - \frac{1}{3!}\dddot{r}_i\delta t^3 + \mathcal{O}(\delta t^4) \tag{4.4}$$

Adding Equations 4.3 and 4.4 and simplifying, we get

$$r_i(t+\delta t) = 2r_i(t) - r_i(t-\delta t) + a_i(t)\delta t^2 + \mathcal{O}(\delta t^4) \tag{4.5}$$

Note that we have from Equation 4.1 and 4.2 that $a_i(t) = \frac{F_i(t)}{m_i} = \frac{-\nabla_{r_i}U(r_1(t),....r_N(t))}{m_i}$, which therefore allows us to compute the position at time $(t+\delta t)$ as a function of the position at t and at $(t-\delta t)$ and the acceleration at t, with the truncation error being of the order of δt^4. This algorithm is indeed simple to implement, accurate and stable. However, an issue with it stems from the fact that velocities of the particles is not computable directly from this algoritm, for which we need to use the equation

$$v(t) = \frac{1}{2\delta t}[r(t+\delta t) - r(t-\delta t)] \tag{4.6}$$

However, we can immediately then note a major problem: the velocities that are calculated are for time step t for which we need to know the position one time step ahead at $t+\delta t$. To overcome this difficulty, a variant of Verlet algorithm is very

commonly used, known as velocity Verlet algorithm [182]. In this case, we have by Taylor series expansion, the following equations for each particle i

$$r_i(t+\delta t) = r_i(t) + v_i(t)\delta t + \frac{a_i(t)}{2!}\delta t^2 + \mathcal{O}(\delta t^3) \tag{4.7}$$

$$v_i(t+\delta t) = v_i(t) + a_i(t)\delta t + \frac{1}{2!}\ddot{v}_i(t)\delta t^2 + \mathcal{O}(\delta t^3) \tag{4.8}$$

$$\dot{v}_i(t+\delta t) = a_i(t) + \ddot{v}_i(t)\delta t + \mathcal{O}(\delta t^2) \tag{4.9}$$

On rearranging Equation 4.9, we get

$$\frac{1}{2}\ddot{v}_i(t)\delta t^2 = \frac{1}{2}[\dot{v}_i(t+\delta t) - \dot{v}_i(t)]\delta t + \mathcal{O}(\delta t^3)$$

The expression for $v(t+\delta t)$ in Equation 4.8 then becomes

$$v_i(t+\delta t) = v_i(t) + \frac{1}{2}[a_i(t)+a_i(t+\delta t)]\delta t + \mathcal{O}(\delta t^3) = v_i(t) + \frac{1}{2m_i}[F_i(t)+F_i(t+\delta t)]\delta t + \mathcal{O}(\delta t^3) \tag{4.10}$$

The velocity Verlet algorithm can then implemented by the following three equations

$$v_i(t+\frac{\delta t}{2}) = v_i(t) + \frac{F_i(t)\delta t}{2m_i} \tag{4.11a}$$

$$r_i(t+\delta t) = r_i(t) + v_i(t+\frac{\delta t}{2})\delta t \tag{4.11b}$$

$$v_i(t+\delta t) = v_i(t+\frac{\delta t}{2}) + \frac{F_i(t+\delta t)\delta t}{2m_i} \tag{4.11c}$$

The first Equation 4.11a computes the velocity at $(t+\frac{\delta t}{2})$, using force and velocity at step t. Using the half-step velocity $v_i(t+\frac{\delta t}{2})$ and Equation 4.11b , the position at time $(t+\delta t)$ is calculated. Finally, using the forces calculated from the new

position $r_i(t+\delta t)$, the full step velocity at time step $(t+\delta t)$ is computed using Equation 4.11c. The main advantage of this modification of the Verlet algorithm is that the atomic positions, velocities and forces are calculated at the same instant of time which lessens the requirement of computer memory as compared to the Verlet algorithm in which case to calculate the velocities, values at two different instances of time needs to be stored.

4.1.2 Potential energy function

As noted in the previous section and Equation 4.2, the potential energy function U is critical for calculating the force on the constituent particles of system and in general to carry out the numerical integration scheme. For biomolecular systems, the function U has contributions from both bonded and non-bonded interactions and are described by empirical force fields. Based on the mathematical formalism and interaction parameters, several highly optimized force fields have been proposed for biomolecular systems, including CHARMM [183, 184], AMBER [185] and GROMAS [186]. In the work presented in this thesis, we have used the CHARMM force field. We now describe the formalism of the potential energy function U in this case [183]. We have

$$\begin{aligned} U = & \sum_{bonds} K_{ij}(r_{ij}-r_0)^2 + \sum_{angles} K_{\theta_{ijk}}(\theta_{ijk}-\theta_0)^2 + \sum_{Urey-Bradley} K_{ik}^{ub}(r_{ik}-r_{ub})^2 + \\ & \sum_{dihedrals} K_{\phi_{ijkl}}[1+\cos(n_{ijkl}\phi_{ijkl}-\gamma)] + \sum_{impropers} K_{\omega_{ijkl}}(\omega_{ijkl}-\omega_0)^2 + \\ & \sum_{Non-bonded} (4\epsilon_{ij}[(\frac{\sigma_{ij}}{r_{ij}})^{12} - (\frac{\sigma_{ij}}{r_{ij}})^6] + \frac{1}{4\pi\epsilon_0\epsilon_r}\frac{q_i q_j}{r_{ij}}) \end{aligned} \tag{4.12}$$

Bonded interactions: The first term in the RHS of Equation 4.12 represents the harmonic vibrational motion, described as a two body spring bond potential between (i,j)-pair of covalently bonded atoms. r_{ij} denotes the instantaneous separation be-

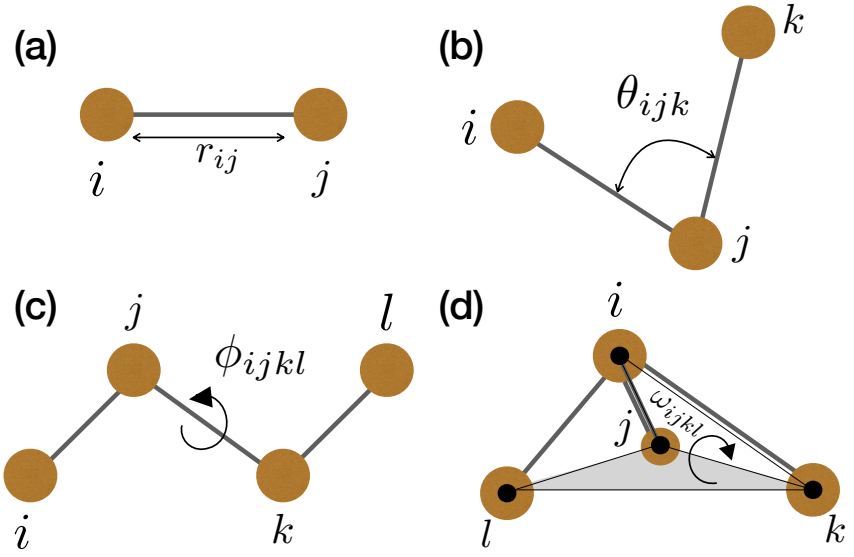

Figure 4.1: Description of bonded interactions: (a) bond-stretching, (b) angle-bending, (c) dihedral and (d) improper dihedral.

tween the i^{th} and j^{th} atoms, r_0 denotes equilibrium bond length and K_{ij} denotes the force constant associated with the bond (Fig. 4.1(a)). The second and third terms in the RHS of Equation 4.12 together constitute the 3-body angular bond potential that describe the angular vibrational motion occurring between (i,j,k)-triple of atoms with $i-j$ and $j-k$ denoting the consecutive bonds. In the second term, θ_{ijk} denotes the angle in radians between vectors $r_{ij} = r_j - r_i$ and $r_{kj} = r_j - r_k$, θ_0 denotes the equilibrium angle and $K_{\theta_{ijk}}$ denotes the angular force constant (Fig. 4.1(b)). The third term is the Urey-Bradley term which is an additional potential function that restrains the motions of the angle associated with the $i-j$ and $j-k$ bonds. In this case, K_{ik}^{ub} denotes the associated harmonic force constant, r_{ik} denotes the instantaneous separation between the pair of atoms (i,k) and r_{ub} denotes their reference separation. The fourth term represents the torsion angle potential function for four consecutive bonded atoms i,j,k,l which restrains the rotation around the middle bond. In this case, $K_{\phi_{ijkl}}$ denotes the dihedral force constant, n_{ijkl} denotes the non-zero positive integer given by the number of minima as the bond is rotated by 360°,

ϕ_{ijkl} denotes the angle in radians between the (i,j,k)-plane and (j,k,l)-plane and γ is the reference angle (Fig. 4.1(c)). The fifth term accounts for the improper torsional angle, in other words to constrain the out of plane bending of atoms i,j,k,l with i bonded to j,k and l. In this case, $K_{\omega_{ijkl}}$ denotes the force constant and ω_{ijkl} denotes the angle between (i,j,k) and (j,k,l) planes, ω_0 denotes the reference angle (Fig. 4.1(d)). We remark that formally the equilibrium values $r_0, \theta_0, r_{ub}, \gamma, \omega_0$ are functions of the sum indices.

Non-bonded interactions: The non-bonded interactions in Equation 4.12 is a combination of van der Waals (sixth term) and electrostatic (seventh term) interaction energies. Formally all (i,j) pair of atoms interact through non-bonded interactions. In practice though, pairs of atoms already involved in bonded interactions are either excluded (for pair of atoms separated by 1 or 2 covalent bonds) or the non-bonded interactions are scaled appropriately (for pair of atoms separated by 3 covalent bonds), with the scaling details depending on the specific force field being used [183]. The first non-bonded term represents the van der Waals interaction between two non-bonded atoms that arises from a combination of attractive and repulsive forces. In Equation 4.12, this is computed using a standard 6-12 Lennard-Jones (LJ) potential, with r_{ij} denoting the distance between the pair of atoms (Fig. 4.2). The repulsive force is dominant at short distances where the electron-electron interaction is strong, increasing sharply as the distance decreases, which prevents the overlap of sites. However, as the separation between the atoms increases, the interaction turns attractive due to the weak dipole attraction between distant atoms. This gives rise to a critical separation of atoms σ_{ij} at which the energy is zero, referred to as the collision diameter. Thus, as the separation increases from σ_{ij}, the interaction turns attractive, with the potential between the two atoms turning negative. As the distance keeps increasing, the potential attains its minimum value ϵ_{ij}, which is the depth of the potential well. The potential then starts increasing with increasing distance, tending to 0 as the distance between the atoms

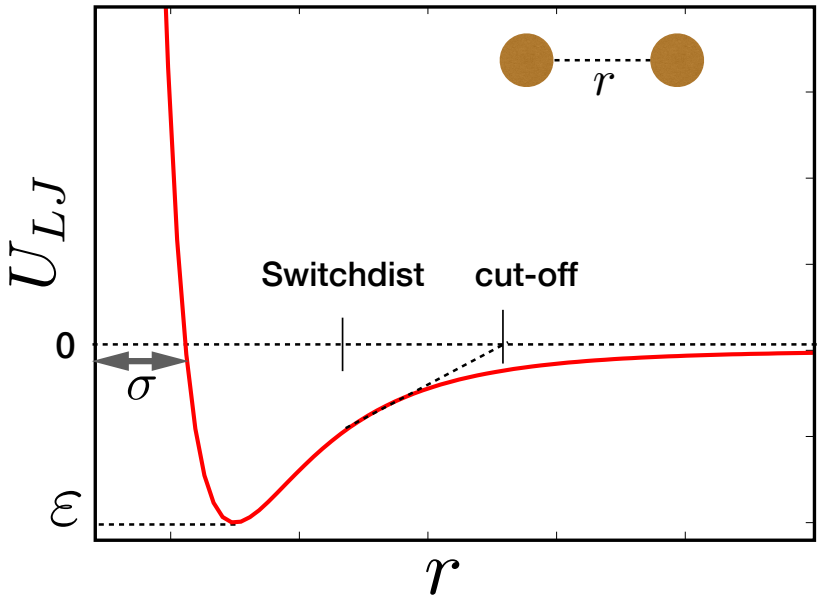

Figure 4.2: The standard 6-12 Lennard-Jones potential U_{LJ} is plotted as a function of distance r between the pair of atoms (red colour solid line). ϵ represents the depth of the energy well and σ is the critical separation at which potential energy becomes zero. With the application of switching function, the potential is smoothly reduced to zero past the cutoff distance, as illustrated by the black dotted line.

approaches infinity. However, it is usually truncated to zero past a cutoff radius. To avoid singularities in the first and higher derivatives of the potential, the truncation is done smoothly through an associated switch function, which takes the potential continuously to zero between switch and cut-off distances (note that the value of switch distance is always less than the cut-off distance). Generally, the parameters σ_{ij} and ϵ_{ij} are not given for specific pairs of atoms but are given as parameters of the atoms themselves, with the pair values being calculated using appropriate mixing rules. For instance, in CHARMM, the Lorentz-Berthelot mixing rules are used, which gives $\sigma_{ij} = (\sigma_i + \sigma_j)/2$ (arithmetic mean) and $\epsilon_{ij} = \sqrt{\epsilon_i \epsilon_j}$ (geometric mean) [187].

The last term in Equation 4.12 represents the second non-bonded term, which is the electrostatic (Coulomb) potential, where r_{ij} is the distance between the pair of atoms, q_i and q_j are the charges on the respective atoms, ϵ_0 and ϵ_r are the

permittivity of free space and relative permittivity of the medium, respectively. The Coulomb potential approaches 0 with r tending to infinity as $1/r$, which is much slower than the case of the LJ potential, which approaches 0 as $1/r^6$. Hence, truncation procedures such as switching leads to artifacts and significantly reduced accuracy in this case [188], underscoring the long-range nature of electrostatic interactions. Therefore, computation of the Coulomb potential is a challenging problem in MD simulations and requires special techniques, as discussed in Section 4.1.4.

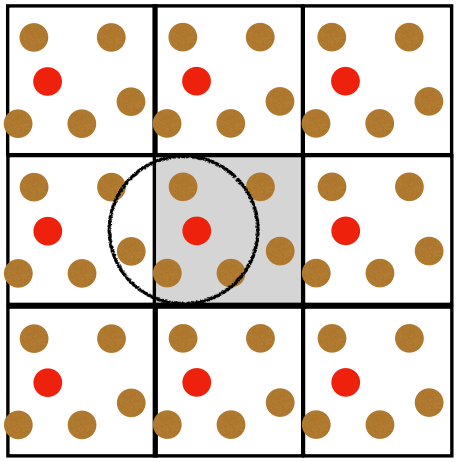

Figure 4.3: Schematic description of implementing periodic boundary conditions in two dimensions. Each atom in the central computational box is surrounded by image atoms residing in the periodic replicas. If an atom leaves the simulation box at one side, it enters the box through the opposite side of that box. The circle around the red atom depicts the minimum image convention, used for short range forces, with the radius of the circle being equal to the cut-off distance.

4.1.3 Boundary conditions

Computer simulations using atomistic potentials are generally performed in a finite system with boundaries. However, atoms lying near the boundaries of the system experience different forces that those lying in the bulk, which can seriously affect the

accuracy of measurements. Therefore, it is essential to chose appropriate boundary conditions in simulations to minimize effect of boundaries. For this, it is common to invoke periodic boundary conditions, thereby making the system pseudo-infinite. In this case, a given atom in the central computational box is surrounded by image atoms residing in each of its periodic replicas (Fig. 4.3). In simulations, the atom in the central computational box and all its image particles move in the same way, for instance, if a atom leaves the simulation box at one side, an identical atom enters the box at the opposite side. Further, each atom is subject to interactions with all other atoms in the system, including periodic images in the surrounding cells, thus eliminating boundary effects. However, this leads to an infinite number of terms in the interaction potential summation. To fix this issue, periodic boundary conditions are typically used with the minimum image convention for short range forces. In this case, we only consider, for a given atom, interactions with closest lying periodic image of its neighbours, as determined by a cut-off distance (Fig. 4.3). For consistency, the cut-off distance is always taken to be less than or equal to half the box length of the central computational box. While short range interactions can be computed effectively in this manner, computing the long-range Coulomb interactions remain computationally unfeasible and require special fast evaluation methods, as we briefly discuss in the next section.

4.1.4 Long-range interactions

For a system of N particles in a cubic box of side L with periodic boundary condition (PBC), the Coulomb potential as given by the last term in Equation 4.12 is modified as

$$U_{coul} = \frac{1}{4\pi\epsilon_0\epsilon_r} \sum_{\mathbf{n}} \sum_{(i,j)} \frac{q_i q_j}{|\mathbf{r}_{ij} + \mathbf{n}L|} \tag{4.13}$$

where $\mathbf{n} = \sum n_i \mathbf{c}_i$ with n_i are integers and $\mathbf{c}_i$ denote lattice vectors, incorporating the

periodic images. The expression can then be rewritten into sums over all particles, with a factor of 1/2 to cancel double counting,

$$U_{coul} = \frac{1}{2}\frac{1}{4\pi\epsilon_0\epsilon_r}\sum_{\mathbf{n}}\sum_{i=1}^{N}\sum_{j=1}^{N}{}' \frac{q_i q_j}{|\mathbf{r}_{ij} + \mathbf{n}L|} \tag{4.14}$$

where the prime(') symbol is introduced to denote that the sum excludes terms for which $j = i$ when $\mathbf{n} = \mathbf{0}$, thus excluding the self interaction. The infinite sum in Equation 4.14 not only converges poorly, but is also conditionally convergent [175]. The computation of Coulomb interactions in a periodic system thus requires special techniques like the Ewald method, in which the long range interaction is divided into two parts- a rapidly varying short range contribution and a slowly decaying long range contribution [189]. The short-range contribution is then computed in real space, while the long-range contribution is calculated in Fourier space, where it converges rapidly. The computational complexity of performing Ewald summuation is $\mathcal{O}(N^{3/2})$, where N denotes the system. In MD simulations, calculation of electrostatic interactions is done using the particle mesh Ewald (PME) method, which allows for even more efficient computation of such interactions [189, 190]. In PME, charges are assigned to a 3-D grid that fills up the simulation space and the long range contribution is computed using 3D-Fast Fourier transform (FFT) technique. This leads to a markedly better complexity of $\mathcal{O}(N \log N)$ of the PME method [191]. For more details on the implementation of the PME method in MD simulations, we refer to [189, 190, 191]. We note that for ensuring convergence of the PME method, it is essential to maintain charge neutrality in the simulation volume [192]. In simulations of biomolecular systems with a net charge, this can be done by addition of counter-ions to ensure charge neutrality, as discussed in Section 4.4.2.

4.2 Calculating Averages from MD simulations

A key objective of MD simulations is to compute observable macroscopic properties, like energies, pressure, etc from microscopic level information generated by simulations like atomic positions and interactions. Average values of such macroscopic properties are calculated in two ways- either as an "ensemble average" or as a "time average". In the first case of "ensemble average", averaging is done over a large number of replicas of the system considered simultaneously, and is given as

$$\{A\}_e = \iint dp^N dq^N A(p^N, r^N)\rho(p^N, r^N) \tag{4.15}$$

where A is the observable of interest, expressed as a function of the momenta p and the positions r of the system that consist of N atoms, $\rho(p^N, r^N)$ is the phase space density at the volume element $dp^N dr^N$ and the integration is over all possible values of r and p. Average values of observable and experimentally relevant macroscopic properties are typically taken to be ensemble averages since such a value is understood to be obtained by taking average over measurements done over multiple experiments. However, calculating ensemble average using MD simulations can have a computationally prohibitive cost since it requires repetition of several simulations done independently.

On the other hand, we can also determine a "time average" of A, which is expressed as

$$\{A\}_t = \lim_{\tau\to\infty} \frac{1}{\tau} \int_{t=0}^{\tau} A(p^N(t), r^N(t))dt \tag{4.16}$$

where t is the simulation time. However, time average of A can be well approximated as $(\sum_{i=1}^{K} A(p_i^N, r_i^N)/K$ for large enough K, where K denotes simulation time

steps and so, can be effectively used in MD simulations to calculate averages. The central dilemma is then to relate experimentally relevant ensemble averages, which are computationally inefficient to calculate using MD simulations and time averages, which can be easily calculated using MD simulations. This is resolved by assuming the *ergodic hypothesis*, which states

$$\{A\}_e = \{A\}_t \tag{4.17}$$

Thus, the ergodic hypothesis makes it possible to calculate average values of experimentally relevant macroscopic observable properties of large systems in a computationally feasible manner using MD simulations.

4.3 Choice of Ensembles

Molecular dynamics simulations can be performed in a variety of ensembles with different characteristics. These include microcanonical ensemble (constant NVE), canonical ensemble (constant NVT), isothermal-isobaric ensemble (constant NPT) and grand canonical ensemble (constant μVT), where N is the number of particles, V is the volume, E is the energy, T is the temperature, P is the pressure and μ is the chemical potential.

For a system with fixed number of particles N and volume V, it can be shown that solving Newton's equations of motion conserves the total energy, thus resulting in the simulations being performed in the microcanonical (NVE) ensemble. However, for modelling biological systems, it is more prudent to perform the simulations in isothermal-isobaric ensemble (NPT), particularly since these conditions more closely mimic real environmental conditions (e.g. in living cells) and further, since experimental data is usually measured under such conditions [193]. In NAMD,

temperature control is commonly carried out using Langevin dynamics, which uses stochastic disturbances to control the temperature. This involves adding an appropriate stochastic force term and subtracting a friction force term from each atom during each integration step [175]. For constant pressure and temperature simulations for which constant temperature condition is implemented by Langevin dynamics, pressure is controlled in NAMD by the Langevin piston Nosé-Hoover method, which uses Langevin dynamics to control fluctuations in the barostat. [175, 194, 195].

4.4 Computational models

In this section, we briefly describe the structure of some of the relevant computational models used in this thesis.

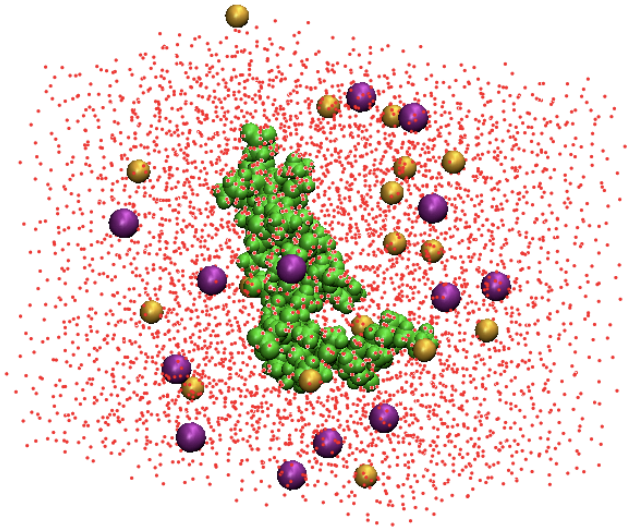

Figure 4.4: Illustrative diagram of an atomistic computational model of a biopolymer (shown in green colour) in a box of water (red colour) and counter-ions (cations and anions are coloured purple and golden, respectively).

4.4.1 Solvent effect:TIP3P water model

An important part of simulations is correctly modelling the appropriate environment for biomolecules of interest. In this regard, solvent environment is arguably the most important environment for biomolecular processes. Over the years, multiple computational models have been proposed for simulating water, a testament to the complexity in understanding the properties of real water [196, 197]. In this thesis, we use TIP3P (transferable intermolecular potential 3P) water model [198] for aqueous environment. This model, as implemented by CHARMM, specifies a three site rigid water molecule, representing one oxygen and two hydrogen atoms with mass, partial charges and Lennard-Jones parameters assigned to each of the three atoms. The chemical structure and atomistic model of TIP3P water are shown in Fig. 4.5.

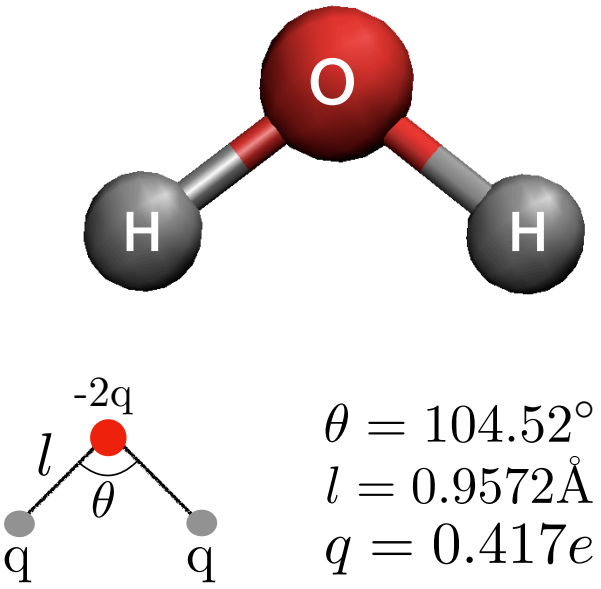

Figure 4.5: Atomistic TIP3P water model. The three sites with an oxygen atom (coloured red) and two hydrogen atoms (coloured silver) are shown. The corresponding parameter values of the model are also depicted.

4.4.2 Addition of explicit salt ions

As discussed earlier, in MD simulations with periodic boundary conditions, the long range electrostatic interactions are computed using particle mesh Ewald (PME) summation technique, for which it is essential to maintain charge neutrality in the simulation volume. For simulations of biomolecules with a net charge in solvent environment, addition of counter-ions to neutralize the system is thus necessitated. In MD simulations, the salt concentration also plays a major role in determining stability of biomolecules [199]. The physiological concentration of NaCl for biological systems is 0.15 mole per litre [200]. For the simulations studies presented in this thesis, addition of counter-ions with appropriate salt concentration, to ensure charge neutrality and physiological salt concentration, is carried out using the autoionize plugin of Visual Molecular Dynamics (VMD) software [180].

4.4.3 Model for bacterial membrane

The primary lipid species of the inner bacterial membrane are zwitterionic phosphatidyl ethanolamine (PE) and anionic phosphatidyl glycerol (PG), which differ by their head-group composition. A computer model for such a bilayer is built with palmitoyloleoyl PE (POPE) and palmitoyloleoyl PG (POPG) in the ratio 7:3, mimicking the inner membrane composition of Gram negative bacteria *E.coli*. The bacterial membrane patch is constructed using CHARMM-GUI membrane builder module [201]. For building the bilayer consisting of POPE-POPG lipid components, 90 POPE and 38 POPG lipid molecules per leaflet are taken. Further, 40 water molecules per lipid molecule is also taken to simulate a fully hydrated bilayer. 82 Na^+ and 6 Cl^- ions are added to neutralize the system and to attain 150 mM salt concentration for mimicking cellular environment. Temperature is maintained at 310 K, which is above the main-phase transition temperature for pure POPE

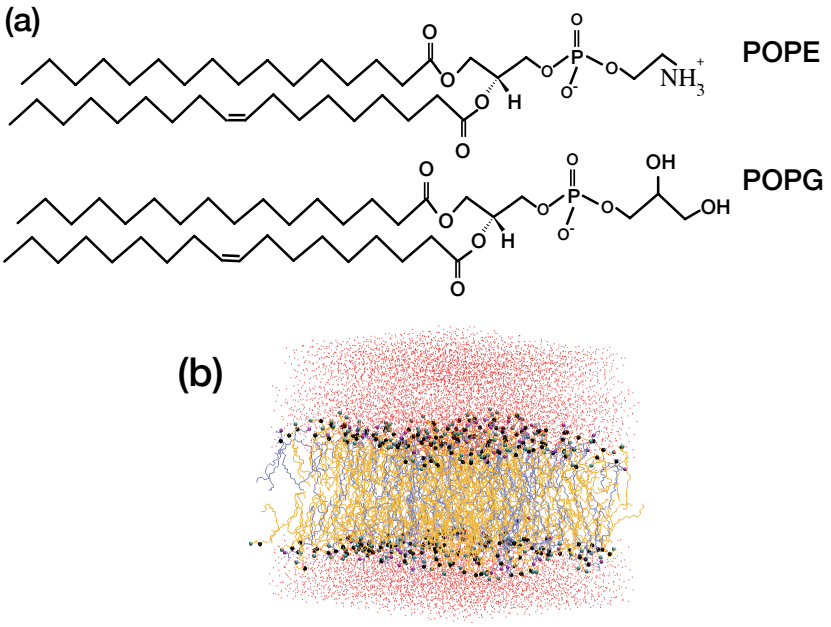

Figure 4.6: (a) Chemical structures of the zwitterionic POPE and anionic POPG lipid molecules are show. (b) Representative snapshot of the atomistic heterogeneous bilayer of the bacterial cell. The POPE lipids are coloured orange and POPG lipids are shown in ice-blue colour; the lipid head groups are oxygen (magenta), nitrogen (cyan) and Phosphate (black). Water oxygen is shown in red colour. Hydrogen atoms of lipid molecules and water are not shown for clarity.

and POPG bilayers [69]. The prepared bilayer is subjected to dihedral, positional and harmonic restraints, which are slowly reduced to zero over 0.8 ns. The bilayer system is equilibrated for 15 ns in isothermal-isobaric NPT (P = 1 atm and T = 310 K) ensemble, over which energy, temperature, pressure and area per lipid are nearly constant following initial fluctuations [202]. The chemical structure of the POPE-POPG lipids and the representative snapshot of the atomistic model bacterial membrane is shown in Fig. 4.6.

Chapter 5

Aggregation dynamics of methacrylate-based ternary biomimetic polymers in solution

5.1 Introduction

Biomimetic antimicrobial polymers or AMPolys have been a focus of research in recent times due to the possibility of their usage as novel therapeutic agents against infectious pathogens [16, 203]. An important first step in investigating the efficacy of the antimicrobial action of such polymers is examining their behaviour in solution phase and in particular, their aggregation dynamics, which can play a key role in determining their eventual interactions with bacterial membrane [96, 204, 205, 206].

Most of the studies on AMPolys have considered only polymers composed of charged cationic and hydrophobic functional groups [16, 18, 102, 103]. However, as discussed in Chapter 1, in such polymers it is very difficult to optimize the monomer composition appropriately for potent antibacterial activity and reasonable selectivity.

Indeed, highly hydrophobic polymers form strong aggregates in the solution which might lead to two undesirable consequences: (1) the strong solution aggregate may preclude partition of the individual AM polymers into the bacterial membrane, (2) such aggregates may bind to human cell membranes due to non-specific hydrophobic interactions, causing undesired toxicity to humans. On the other hand, low hydrophobic content in the AM polymer may lead to stabilising the structures in the solution and decrease their ability to penetrate into the bacterial membranes. Hence a requisite amount of hydrophobicity is needed to increase the local concentration of the AM polymers for efficient interaction and eventual partitioning of the AM polymers into the membrane which requires a fine tuning of not only the hydrophobic content of polymers, but spreading of the same along the polymer backbone. In this context, more recent works [23, 207, 208, 209, 210, 211] have been focusing on inclusion of additional functional groups like polar groups, in addition to cationic and hydrophobic groups, which also comes closer to the functional group distribution in naturally occurring AM peptides. For instance, it has been shown, using ternary nylon-3 copolymers, that replacing some of the hydrophobic or cationic groups or both by hydroxyl residues can significantly reduce the hemolytic activity of the copolymer compared to their binary counterpart with only hydrophobic and cationic subunits [209]. More recently, Mortazavian et al. used ternary copolymers to decouple the effects of cationic and hydrophobic functional groups on the antimicrobial and hemolytic activities of such polymers [23]. Their study demonstrated that the plausible role played by polar groups in the polymer is to reduce the formation of sequential domains of hydrophobic monomers, which can effectively modulate polymer chain insertion into bacterial and human cell membranes.

In this chapter, our aim is to understand the role played by inclusion of polar groups and specific sequence of functional groups along the polymer backbone in the aggregation dynamics of methacrylate polymers in solution phase using detailed atomistic simulations. In this context, multiple polymers with compositions of bi-

nary (only cationic and hydrophobic groups) and ternary (cationic, hydrophobic and polar groups) and with random and block arrangements of the functional groups are studied in solution phase to understand their aggregate morphologies. Our studies highlight the importance of inclusion of polar groups which act to redistribute the effective hydrophobicity along the polymer backbone resulting in weaker yet functionally relevant aggregate conformations, compared to aggregates of polymers with strong hydrophobic content, due to larger conformational fluctuations, particularly in the case when the functional groups are randomly distributed along the polymer backbone. Such loosely packed "weak aggregates" can play a crucial functional role in antibacterial action, by facilitating dissociation of polymers from the solution aggregate, which will likely lead to the favourable partitioning of the polymers into the bacterial membrane and consequently membrane disruption. This study is based on work in Ref. [109].

5.2 Models and methods

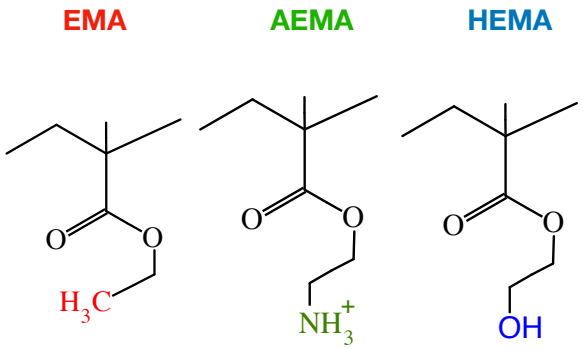

Figure 5.1: Chemical structures of EMA (hydrophobic), AEMA (charged cationic) and HEMA (uncharged polar) groups considered in the model polymers.

Atomistic MD simulations with explicit water and ions were performed on two classes of model biomimetic polymers- ternary and binary polymers. Ternary methacrylate random polymers ("model T"), consisting of cationic ammonium (amino-ethyl

Model Polymer	DP	AEMA No.	HEMA No.	EMA No.
Ternary (T, TB)	19	+6	5	8
Binary (B, BB)	19	+6	0	13

Table 5.1: Proportion of AEMA, HEMA and EMA groups in the model polymers.

methacrylate: AEMA), hydrophobic alkyl (ethyl methacrylate: EMA) and neutral hydroxyl (hydroxyl methacrylate: HEMA) groups as shown in Fig. 5.1, are modelled with degree of polymerization (DP) = 19. The chosen composition of ternary polymer (AEMA-6, EMA-8 and HEMA-5) has been shown to be optimal for antimicrobial activity and also shows significantly reduced hemolytic activity[23]. To understand the role played by sequence of functional groups, we performed simulations involving ternary polymers which have a block arrangement of functional groups, consisting of same % of groups as model T but having blocks of sequences 6(AEMA)-5(HEMA)-8(EMA) along the polymer backbone ("model TB"). Further, to highlight the role of inclusion of polar hydroxyl functional groups, control simulations without them involving only binary compositions of cationic (AEMA) and hydrophobic (EMA) monomer units in random ("model B") and block ("model BB") configurations, were also performed. The degree of polymerization was kept same as for ternary polymers and the number of groups per chain was taken to be 6 (AEMA) and 13 (EMA). Details of the composition of various subunits in the model polymers are summarized in Table 5.1 and the detailed chemical structures of all the four model polymers are shown in Fig. 5.2. It is important to note that for all the model polymers, the number of cationic functional groups are fixed to be 6 per polymer in agreement with Mortazavian et al [23], where it was found that despite differences in EMA composition, the minimum inhibitory concentration (MIC) values of all polymers start to level off at $\sim 30\%$ of AEMA and cationic groups above 30 % do not increase the antimicrobial activity of the polymer. This proportion of charged cationic groups is also comparable to net positive charge of most natural AMPs [73].

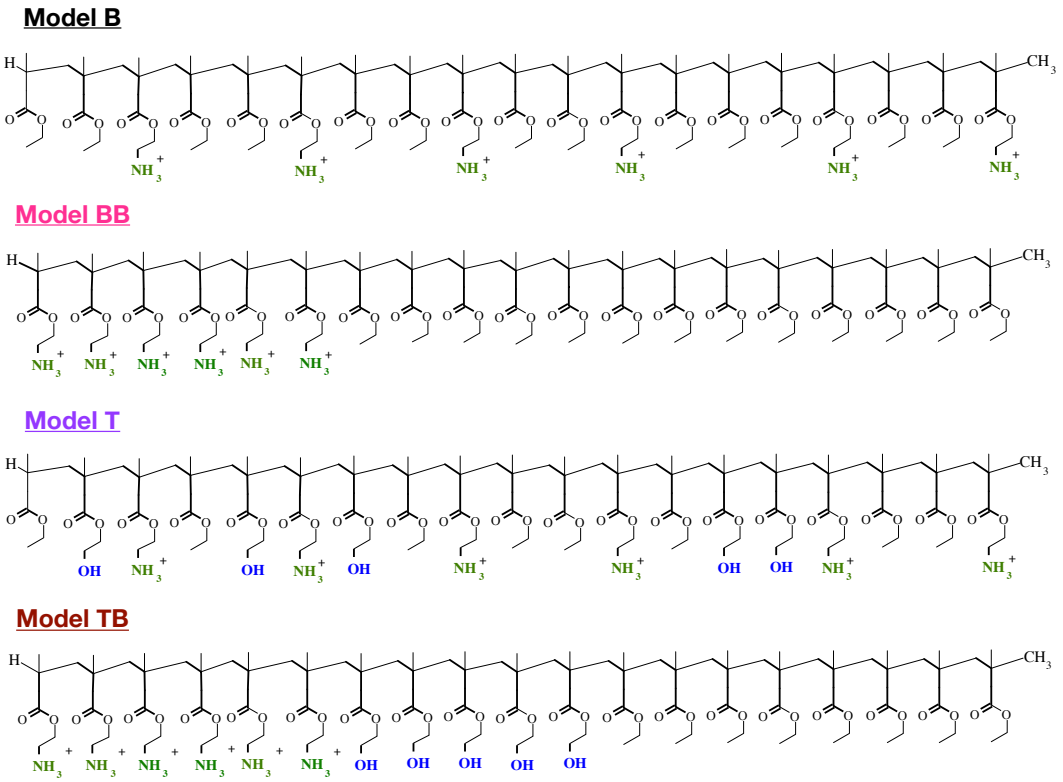

Figure 5.2: Chemical structures of binary polymers (models random B, block BB) and ternary polymers (models random T, block TB). In all the model polymers, degree of polymerization (DP) = 19 and the number of cationic groups is fixed to be 6 per polymer.

A single polymer chain for each system was built in an extended conformation and solvated with TIP3P [198] water. The total charge of a single polymer chain in each of the system was $+6e$, and requisite salt ions were added to both neutralize the systems and to maintain 150 mM salt concentration to mimic physiological conditions in each case. All simulations were performed with the NAMD 2.9 simulation package [175]. Each system of polymers was first energy minimized with the conjugate gradient method. Single polymer chain simulations were done with 2 fs timestep and performed in the (isothermal - isobaric) NPT ensemble for 2 ns. Next, systems of aggregated polymers were built by selecting 10 random conformations from the single polymer simulation trajectory. This group of 10 initially dispersed polymers for each model (T, TB, B and BB) were placed in TIP3P water, in a cubic box, with a minimum distance of 12 Å between any polymer atom and the box side,

under periodic boundary conditions. A concentration of 150 mM of NaCl salt was maintained to neutralize the system. Initially, the systems were energy minimized with conjugate gradient method and equilibrated with 2 fs timestep for 5 ns of NVT simulation to stabilize the system and all the subsequent runs for at least 150 ns were done in the NPT ensemble (All the polymer systems and simulation details are listed in Table 5.2). All the MD simulations were performed at constant temperature maintained at 305 K with Langevin dynamics at a collision frequency of 5 ps^{-1}, and a pressure of 1 atm was maintained through Langevin piston [194, 195]. Electrostatic interactions were calculated by the Particle Mesh Ewald method [212] and the cut-off for Lennard-Jones interactions was set to 12 Å, with smoothing starting from 10 Å. The parameter values for the polymers were adopted from the CHARMM force field [213] and previous simulations [100, 101, 202]. The largest aggregate, in other words the aggregate constituting of the largest number of polymers, in each run is extracted for further analysis to understand the properties of the aggregation dynamics of model polymers in solution. Three independent simulations were performed for each model polymer with different initial configurations of dispersed polymers. The visualization was done using software VMD [180] and the analysis for the polymer aggregates was done by taking average over multiple independent runs, unless otherwise stated, using TCL scripting language which is embedded with VMD.

5.3 Results

5.3.1 Morphology of the aggregates

In this section, we study the role of inclusion of polar functional group and also the importance of understanding how sequence of functional groups in the AM polymers affect the morphology of the aggregates in solution. All the polymers with

Model	Sequence	Aggr. run Time(ns)	Aggr. size, N_{agg} S1, S2, S3
Binary polymers	(AEMA-EMA)		
B	Random	150, 150, 150	4, 4, 5
BB	Block	150, 150, 170	6, 10, 8
Ternary polymers	(AEMA-HEMA-EMA)		
T	Random	150, 150, 150	4, 5, 4
TB	Block	150, 150, 150	5, 7, 4

Table 5.2: Summary of the model polymers and their largest aggregate size denoted N_{agg} at the end of at least 150 ns NPT simulation runs. In each case, initial configuration consists of 10 randomly dispersed polymers in a box of water and ions. Three independent NPT runs were performed for the aggregation of polymers. Note that model BB (S3) has $N_{agg} = 5$ till 160 ns, after which it fuses with an aggregate of size, $N_{agg} = 3$ to form bigger aggregate of size 8.

and without polar groups and with random and block arrangements of functional groups form aggregates in the solution, albeit with different morphologies and intra-aggregate interactions, as suggested by previous experimental results [204]. Illustrative snapshots of the aggregates in solution, at the end of one of the representative simulation for all the four models are shown in Fig. 5.3. Each model was independently simulated three times to confirm that the final aggregation morphology is independent of the starting state of the polymers and to ensure reproducibility of results. In Table 5.2, we present the sizes of the largest stable aggregate formed for each model polymer within the simulation time, with the number of polymers in the aggregate denoted as N_{agg}. Visual inspection of the trajectories indicate that the evolution of aggregates for different polymer models is markedly different- the aggregates formed from random binary (model B) polymers form relatively compact assemblies displaying significant entanglement of the constituent polymers while the random ternary polymer (model T), with partial replacement of hydrophobic EMA groups by hydroxyl HEMA groups, form somewhat more open and comparatively less entangled aggregates. The binary block polymer (model BB) form larger sized aggregates, showing a star-like micellar conformation with a dense hydrophobic core surrounded by cationic subunits, exposed to water solution. The ternary block

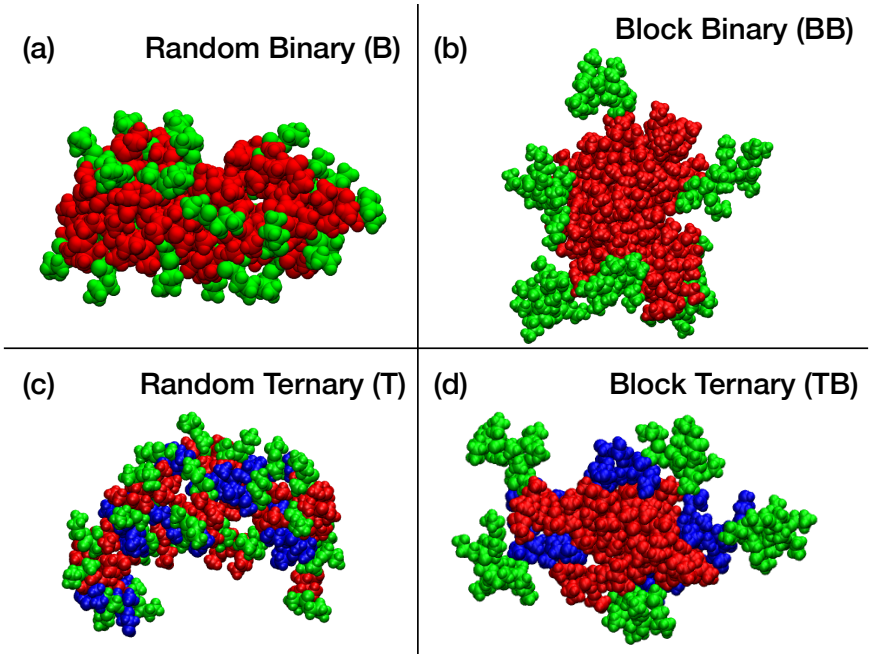

Figure 5.3: Representative conformation of the aggregates with different side chains, hydrophobic (EMA, red), cationic (AEMA, green), and polar (HEMA, blue), at the end of one of the 150 ns long simulation for binary polymers (a,b) and ternary polymers (c,d). The number of polymers in a typical aggregate, N_{agg} for the snapshots shown are 4 (model B), 6 (model BB), 4 (model T) and 5 (model TB) (see Table 5.2 for more details).

(model TB) also form large aggregates compared to its random counterpart, though in this case the HEMA group remains clustered between EMA and AEMA groups. Our aim now is twofold, to analyse (a) the effect of inclusion of polar groups (binary vs ternary) and (b) the effect of variation in the sequence of the AEMA, EMA and HEMA groups along polymer backbone (block vs random) on the shapes and sizes of the aggregates formed.

Shape Parameters - We consider two shape parameters [214, 215], eccentricity (ε) and prolateness (Δ) to describe the morphologies of aggregates for the four model polymer systems, both of which are calculated from the moment of inertia tensor (I) of the aggregate as:

$$\varepsilon = 1 - \frac{I_{min}}{I_{avg}},$$

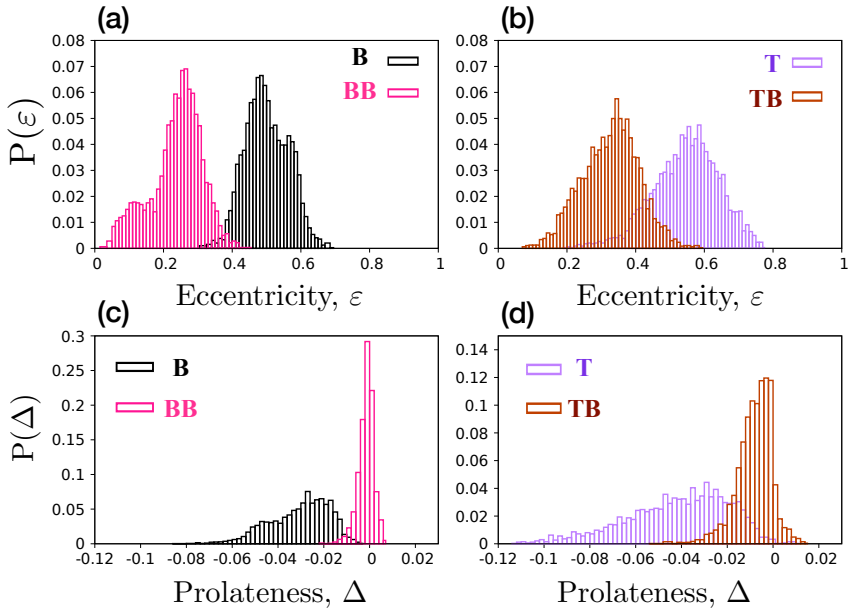

Figure 5.4: Distribution of the eccentricity, ε and prolateness, Δ measured for the aggregates formed from the models (B, BB, T and TB) from the start of aggregation formation till the end of the 150 ns simulation runs, averaged over all the initial conditions.

$$\Delta = \frac{\prod_{i=1}^{3}(I_i - I_{avg})}{I_{avg}^3}$$

where I_{min} and I_{avg} denote the minimum and the average values of the principal moments of inertia (I_1, I_2 and I_3). For perfectly spherical objects $\varepsilon, \Delta = 0$ and $\varepsilon = 1$ for linear objects while negative and positive values of Δ correspond to oblate and prolate ellipsoid shapes.

The results for probability distribution of these shape parameters of the aggregates formed from the model polymers over the time from the start of stable aggregation formation till the end of the simulation run are shown in Fig. 5.4. Data in Fig. 5.4(a) and Fig. 5.4(b) shows that the mean and width of the distribution of eccentricity (ε) values of ternary polymer aggregates are larger than those of binary polymer aggregates (B and BB models), suggesting a more extended structure and also the

fluctuating dynamic conformations in case of the model T and TB aggregates. The average value of ε is smaller for the aggregates formed from block polymers (BB, TB) compared to random polymers (B, T) and this strongly shows that aggregates formed from block polymers are more compact compared to the aggregates formed from random polymers. The probability distribution of the prolateness (Δ) for all the four models is shown in Fig. 5.4(c) and Fig. 5.4(d) and the data confirms that the block polymers indeed form more spherical and compact structures ($\Delta \approx 0$) but the random polymers with negative values of Δ quantify the oblate shape of their aggregates. The data also suggests that the conformational dynamics of the aggregates formed by the random ternary polymers is much higher than that of random binary polymers. The shape parameters (ε and Δ) thus demonstrate the following - the shape parameter values for aggregates in which the hydrophobic content is large and which have no additional polar groups (as in model B and model BB aggregates) are narrowly distributed, hence displaying less variability in their conformations. On the other hand, the aggregates of the polymers having polar HEMA groups (model T and model TB aggregates) show significantly larger variance in the values of the shape parameters. This underlines the role of the polar HEMA groups in inducing conformational fluctuations in these aggregates. However, the Δ and ε data does suggest that on the average, the block polymer aggregates (model BB and model TB) have a closer to spherical morphology as compared to their respective random polymer aggregates counterparts. This is likely due to the presence of hydrophobic groups distributed across the backbone of the random polymers, which then leads to the gluing of the polymer chains in a more bundle-like conformation.

Size measures - One of the measures of aggregate dimensions and stability is the radius of gyration [216], defined as the root mean square distance of the constituents of the aggregate from its center of mass. We compute the radius of gyration R_g of the aggregates as a function of time over the last 30 ns of the simulations for random

polymer aggregates with $N_{agg} = 4$ and block aggregates with $N_{agg} = 5$, as shown in Fig. 5.5(a) and Fig. 5.5(b).

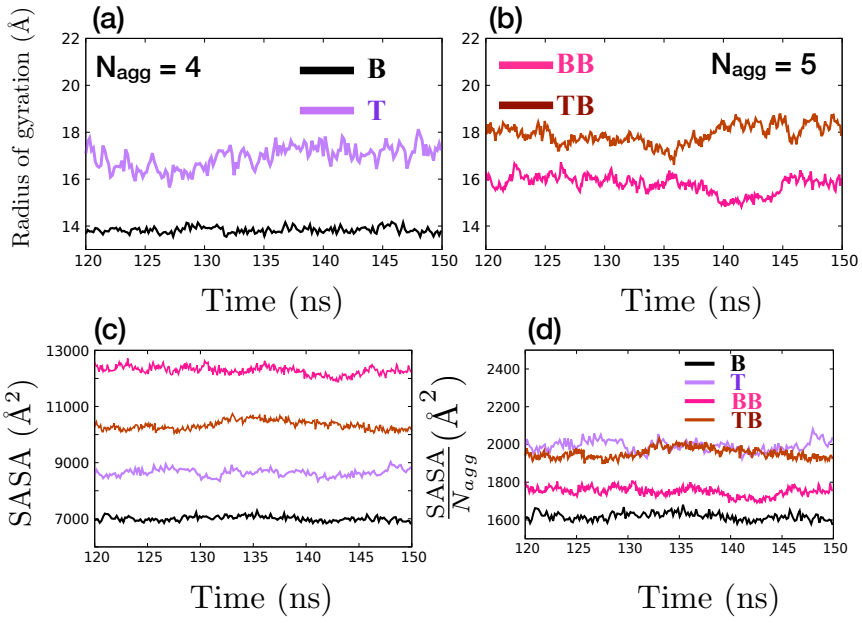

Figure 5.5: (a) Radius of gyration for random polymers (models B, T) having aggregate size $N_{agg} = 4$ and (b) block polymers (models BB, TB) having aggregate size $N_{agg} = 5$ is plotted as a function of time, (c) SASA values of the aggregate and (d) average SASA/N_{agg} is plotted as a function of time.

We observe that in both cases, the ternary aggregates exhibit a higher R_g value, highlighting the role of polar HEMA groups in inhibiting formation of strong, well packed compact aggregates. Interestingly, the R_g value of model T aggregate is comparable to the R_g value of model TB aggregate, even though the aggregate size N_{agg} is larger for model TB aggregate (4 vs 5). This in particular shows that the random ternary (model T) polymer aggregate has the least compact structure amongst the polymer aggregates considered here, forming a loose and open aggregate conformation.

Solvent Accessible Surface Area (SASA) and aggregate-water interaction - Structural properties of the aggregates can also be inferred by measuring the Solvent Accessible Surface Area (SASA) [217] of the aggregate. The total SASA values of the aggregates is calculated with a spherical probe of radius 1.4 Å. The higher

values of total SASA, as depicted in Fig. 5.5(c), for block polymer aggregates as compared to random polymer aggregates is partly due to micellar structure that are formed, particularly for the block binary case, with efficient sequestration of hydrophobic EMA groups at the core and predominant exposure of the other functional groups to solvent. The random arrangement of functional groups along the polymer backbone frustrates such efficient partitioning of the polymers in an aggregate resulting in lower SASA values, in particular for binary random polymer (model B) aggregate. However, block polymers form larger aggregates, which partly leads to higher SASA values. To discount the effect of aggregate size, we compute the average SASA of the aggregates per polymer (in other words, SASA values divided by N_{agg}), as shown in Fig. 5.5(d). For the ternary case, we see an interesting picture emerging, with the SASA per polymer values being highest for the random ternary (model T) aggregate, similar to the case of R_g values. This confirms the loosely packed, open structure of the model T aggregate. For model TB aggregate, the SASA per polymer value is comparatively less than that of model T aggregate, suggesting that though the presence of HEMA group seemingly weakens the model TB aggregate, its hydrophobic core nevertheless is fairly strong. Thus, the ordered placement of groups along the polymer backbone likely counters the propensity of polar HEMA groups to impede the formation of a compact, well packed aggregate.

To further probe this and to quantify the nature of interaction between the aggregates and bulk water in general and to estimate the exposure of hydrophobic core to water in particular, the radial density of water is calculated as a function of distance from the aggregate center of mass by counting water molecules in 0.1Å of shell width around the center of mass and compared with the radial density of the aggregate itself (Fig. 5.6). We observe that in case of model T aggregate (Fig. 5.6(a)), the density of water is already non-zero very close to the COM of the aggregate but it slowly increases to reach the maximum bulk density far from the center of mass. This underscores that the core of the model T aggregate is weak-

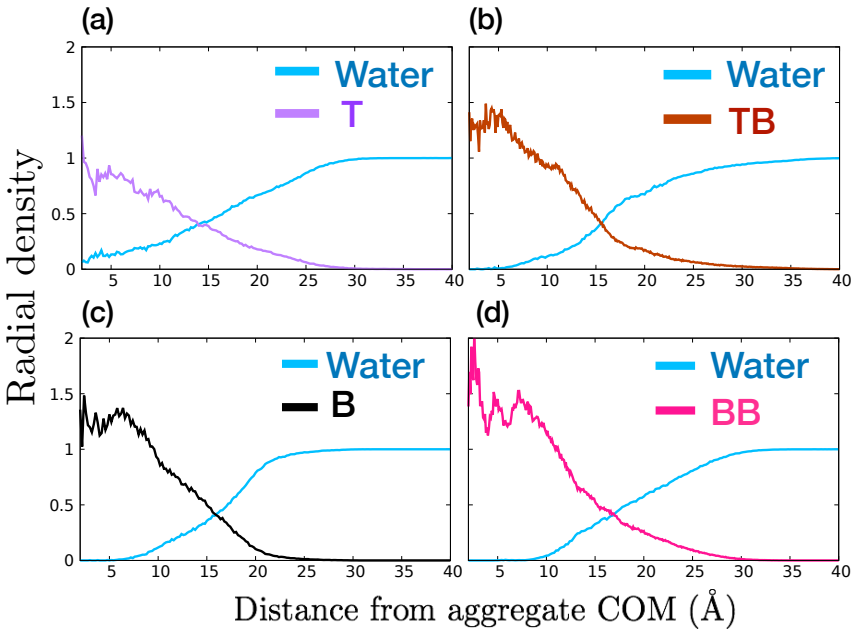

Figure 5.6: Radial density profiles of the aggregate and water molecules plotted as a function of distance from the COM of the aggregate for (a) model T, (b) model TB, (c) model B, (d) model BB. The analysis is done over the last 30 ns (120-150 ns) of one of the simulation runs (S1).

ened with significant exposure to water (a plausible consequence of the presence of hydrophilic HEMA groups which favour interactions with water) and further, that it has a loosely packed, somewhat open structure, as was also deduced by our previous analysis. On the other hand, in case of the model TB aggregate (Fig. 5.6(b)), non-zero water density only starts to appear at ~ 5 Å from the center of mass, indicating that it has a comparatively strong hydrophobic core. In general, we observe that non-zero water density starts earlier and shows a comparatively slower rise to reach bulk water density in case of ternary aggregates as compared to the binary aggregates. This suggests that the presence of HEMA groups results in formation of loosely packed aggregates which adopt more extended conformations. For model B polymer system (Fig. 5.6(c)), we observe that non-zero water density starts away from the center of mass and it increases sharply to reach the maximum bulk density, confirming its compact aggregate structure with relatively high hydrophobic density near the center of mass, again showing good agreement with our previous analysis.

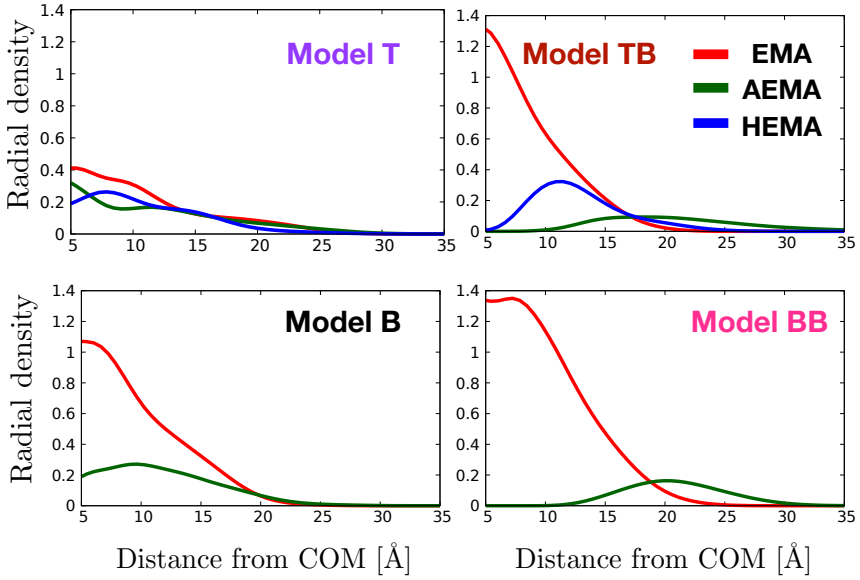

Figure 5.7: (a) Radial density profiles of various components of the aggregates (EMA, AEMA and HEMA) for all the models considered in this chapter, calculated along the radial direction from the center of mass of the aggregate.

In case of the block binary model BB (Fig. 5.6(d)), water density is zero for a long distance from the center the aggregate. This, in conjunction with the radial density profiles of EMA and AEMA groups (Fig. 5.7) and our previous analysis, clearly shows that in this case, large sized aggregates are formed whose hydrophobic core is densely packed with EMA residues, is relatively impermeable to water and is surrounded by cationic residues in a spherical micellar conformation. Note that in case of model TB aggregate as well, the radial density profiles (Fig. 5.7) exhibit that the core is primarily composed of EMA residues while the cationic residues largely lie at the boundary of the aggregate. In contrast, both random aggregates, model B and model T show display presence of the all the respective constituent functional groups in the aggregate core.

To summarise, our analysis allows us to make the following conclusions - block polymer systems tend to form larger aggregates, which display more compact structures with cores primarily composed of hydrophobic moeities as compared to their random counterparts, for both binary and ternary compositions. The block binary aggregate

displays a spherical micellar conformation with a strong hydrophobic core which is almost impermeable to water, surrounded by cationic groups, the random binary aggregate displays a more ellipsoidal shape. However, presence of polar HEMA groups in the ternary polymers leads to a marked change of behaviour- it induces conformational fluctuations and in general results in formation of loosely packed, open aggregates particularly in the case when the functional groups are randomly distributed along the polymer backbone. Such loosely packed "weak aggregates" can play a crucial role in antibacterial action. In these cases, polymer dissociation from the aggregate can occur, with polymer-lipid head groups of the bacterial membrane interactions becoming favourable over polymer-polymer interactions more easily, as compared to well packed, stable aggregates [86, 202]. This can lead to polymer insertion into the bacterial membrane and thus, membrane disruption and eventual cell death. The results also reiterate that a high hydrophobic content can result in a strong aggregate, which can result in two undesirable results: their interactions with bacterial membranes may be ineffective or they can be highly toxic to mammalian membranes [96, 204, 218]. A possible role of the polar HEMA groups can be to modulate the intra aggregate interactions and affecting polymer-membrane interactions. In the next section, we study how the inclusion of HEMA groups can affect the inter-polymer binding, to highlight its likely role in facilitating the partitioning of the polymers from aggregate to membrane phase.

5.3.2 Polar groups in aggregation dynamics - binary vs ternary

In this section, our aim is to understand the role of the polar HEMA groups on aggregation dynamics, in particular the effect of replacing hydrophobic EMA groups by polar HEMA groups on the stability of aggregates formed, particularly in case of random aggregates (models B and T). In this context, we first note that the total

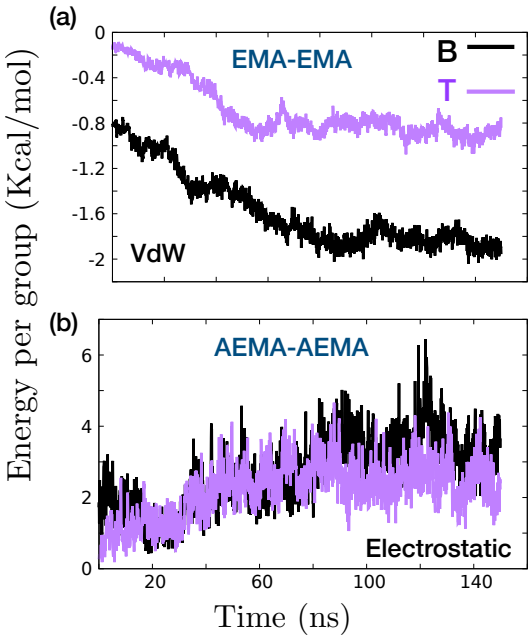

Figure 5.8: Pair interaction energy per unit group plotted as a function of time. Model B is shown in black colour and model T is shown in purple colour. (a) Van der Waals energy per EMA for hydrophobic groups and (b) electrostatic energy per AEMA for cationic side chain groups are shown for both the polymer aggregates.

van der Waals interaction energy is higher for the model B aggregate, as expected due to the presence of more hydrophobic EMA groups. However, the question then arises whether the same is true even after the effect of the presence of higher proportion of hydrophobic moieties is discounted. Our data in Fig. 5.8(a) shows that indeed this is the case, with the the total van der Waals energy per EMA group remaining appreciably more attractive for the model B aggregates. This indicates that on the average, EMA-EMA interactions are strongly attractive in this case and thus, contribute considerably to the stability of the aggregate. On the other hand, for the model T aggregate, the interactions are much weaker due to the presence of polar HEMA groups, which clearly impede the formation of a strong aggregate. However, the electrostatic interactions between models B and T are not significantly different due to the presence of same number of cationic AEMA groups in both the set of polymers (Fig. 5.8(b)). Therefore, the more attractive van der Waals interactions in the model B aggregate is a clear indication that the

hydrophobic EMA groups primarily drive the aggregation formation for model B polymers. This is further illustrated by considering the inter polymer and intra polymer contact probabilities of the EMA-EMA moieties, as shown in Fig. 5.9. A contact between two EMA groups is said to exist if the two are within 7 Å of each other and is classified as an intra-contact if the EMA groups belong to the same polymer or as an inter-contact, otherwise. We deduce from Fig. 5.9 that in case of the model B aggregate, as it evolves, the inter polymer contacts match the intra contacts, which strongly suggests that polymers in the aggregate are entangled with each other and consequently, it has a much more tightly interwoven structure, driven primarily by EMA-EMA interactions. However, this is manifestly not true for the model T aggregate, in which case the intra contacts always remain higher than the inter contacts, which indicates that the EMA-EMA interactions are not the primary driver of aggregation dynamics in this case. It also suggests that the individual polymers in the model T aggregate are most likely in a self-compact structure with more intra-polymer contacts and fewer inter polymer contacts. This is further proof that the partitioning of the polymers from the aggregate will be significantly easier in model T polymer aggregates than for model B polymer aggregate.

Role of HEMA groups in ternary aggregation - For the ternary polymer model T, the number of cationic AEMA groups remains the same with polar HEMA groups replacing $\sim$ 40% of the hydrophobic EMA groups as compared to binary model. With the reduction in number of EMA groups in the ternary polymers, it is important to probe the aggregation dynamics and the effective attractive interactions in the aggregate. The HEMA groups contribute to both electrostatic and van der Waals interactions in the aggregate and the results are shown in Fig. 5.10. In Fig. 5.10(a), the radial distribution function, $g(r)$, between HEMA-AEMA and HEMA-EMA groups strongly exhibits the robust attractive electrostatic interactions between the hydroxyl groups of HEMA and amide groups of AEMA in the

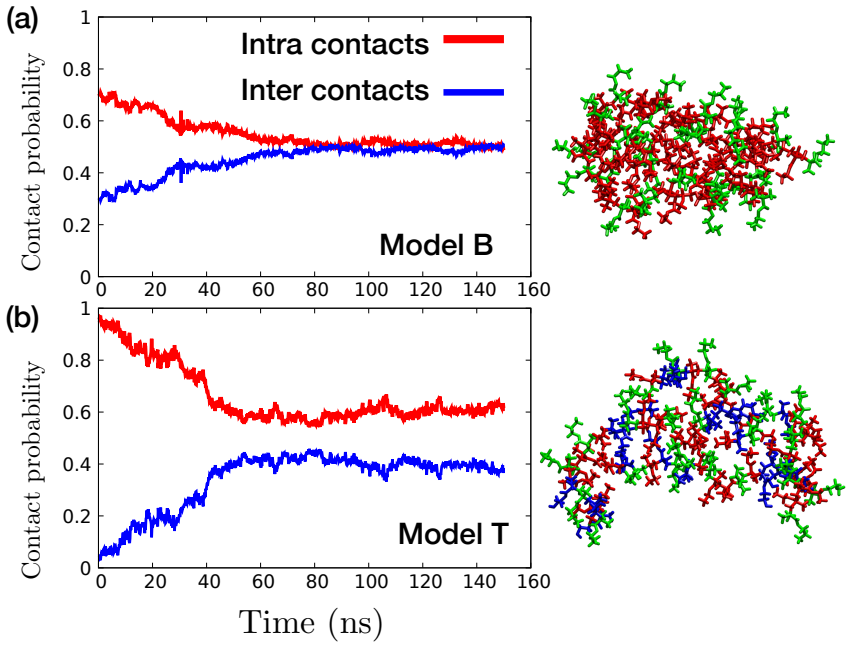

Figure 5.9: Average contact probability between hydrophobic EMA groups that belong to same polymer (intra-contacts) and different polymers (inter-contacts) plotted as a function of time for (a) model B, (b) model T. Representative snapshots for the binary and ternary random model aggregates are depicted to the right, with EMA, AEMA and HEMA groups represented in red, green and blue colour respectively.

aggregate. This underscores the role of effective attractive electrostatic interactions between the model T polymers in offsetting the repulsive interactions between the AEMA groups. This effect can be captured in the computation of electrostatic interactions between AEMA and HEMA groups, as shown in Fig. 5.10(b) plotted as interaction energy, which shows that the effective electrostatic interactions between HEMA-HEMA groups and HEMA-AEMA groups are attractive in nature. The repulsive electrostatic interactions between AEMA groups are also shown for reference.

Regarding the van der Waals interactions between EMA groups in model B and between (EMA+HEMA) groups in model T, Fig. 5.10(c) shows that even after replacing 40% of EMA groups with HEMA groups, the van der Waals interactions per non-charged functional groups are not affected significantly. As can be seen from Fig. 5.1, the polar HEMA groups have the same side group as hydrophobic

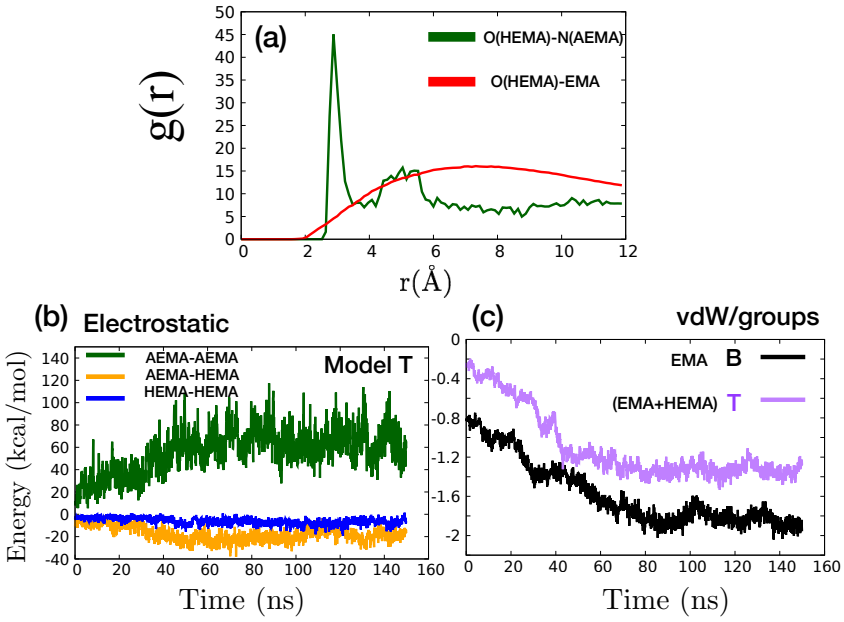

Figure 5.10: (a) Radial density function g(r) for model T, computed over the last 30 ns of one of the simulation run (S1). (b) Total electrostatic energy is plotted as a function of simulation time, computed between AEMA-HEMA, AEMA-AEMA and HEMA-HEMA groups of the model T aggregate. (c) van der Waals energy per group is plotted as a function of simulation time, computed between EMA-EMA groups of model B aggregate and (EMA+HEMA)-(EMA+HEMA) groups of model T aggregate are calculated.

EMA groups, albeit an addition of OH moiety, suggesting that HEMA groups also contribute to the overall hydrophobic content of the polymer. So, while there is significant difference in EMA-EMA group interaction energies in models B and T (as seen in Fig. 5.8(a)), if we compute the effective hydrophobic interaction energy by including HEMA groups as well (Fig. 5.10(c)), the difference between models B and T is significantly reduced. Given that the polymers considered here have 30% cationic functional groups, the interactions that drive the aggregation of the polymers in solution have to be van der Waals interactions, which should be able to efficiently overcome the repulsive electrostatic interactions. However, for the polymers like AM polymers, whose functional goal is to disrupt the bacterial membranes as well as be non-toxic to mammalian membranes, a subtle balance of hydrophobic content with effective weak intra-aggregate interaction is needed for efficient action as membrane

active agents. In this regard, the analysis presented here strongly supports the role of inclusion of polar HEMA groups as a tuning parameter for aggregate formation as well as for formation of weaker aggregates. By contributing to the overall hydrophobicity, though smeared along the polymer, the HEMA groups contribute effectively towards formation of aggregates, overcoming the cationic group repulsion. They also form attractive electrostatic interactions with the cationic groups, effectively neutralising them and contribute further to aggregate stability. However, due to their higher propensity to water and lowered individual hydrophobic content, the HEMA groups preclude the polymers from forming a strong hydrophobic core as can be seen in the binary model B polymers. The present simulations clearly depict that replacing the strongly hydrophobic EMA groups by polar HEMA groups helps in 'smearing' the overall hydrophobicity while retaining the overall non-bonded energy and rendering the aggregates of such polymers optimally weaker in solvent than those with a higher content of hydrophobic groups. This should be reflected in how the aggregates of model T and model B polymers effectively interact with bacterial membranes and consequent partitioning of the polymers from the aggregate into the membrane.

5.4 Discussion

In this chapter, we investigated the role played by inclusion of polar groups into methacrylate polymers on the aggregation dynamics in solution phase using atomistic molecular dynamics simulation. The four model polymers considered in this study have a flexible backbone and consist of charged cationic and hydrophobic (binary polymers) or charged cationic, polar and hydrophobic subunits (ternary polymers). The components of the polymers are either placed randomly (models B and T) or in block sequence of groups (models BB and TB) along the polymer backbone. The chosen composition of ternary polymers has been shown experimen-

tally to be optimal for antimicrobial activity and also shows significantly reduced hemolytic activity [23] and one of the main goals of the present study was to understand the role played by inclusion of polar HEMA groups on the pre-membrane interaction stage, which is the interactions of multiple ternary polymers and resulting aggregation dynamics in solution phase. Both binary and ternary polymers form aggregates in water while displaying markedly different aggregation dynamics. We analysed the morphology of the aggregates and discussed how the presence of polar groups and the role of sequence of various subunits along the polymer backbone affect the aggregation conformation in solution. Our data suggests that block polymers tend to form larger sized aggregates displaying more compact structures as compared to their random counterparts. The binary polymers, composed only cationic and hydrophobic functional groups, form relatively well packed, stable aggregates. However, there are differences in the aggregate morphologies arising due to differential sequencing of the constituent groups along the polymer backbone: while block binary (model BB) aggregates display a spherical conformation with a remarkably strong hydrophobic core which is almost impermeable to water surrounded by cationic groups, the random binary (model B) aggregates display a more ellipsoidal shape with relatively weaker core displaying higher permeability to water. This observation is in very good agreement with scattering experiments and fluorescence imaging of aqueous block and random polymers, which suggest that intermolecular critical aggregation concentration (CAC) of the random polymers is much higher than that for the aqueous block polymers, displaying weaker aggregation tendency of random polymer model [96].

We also analysed in detail the effect of presence of polar HEMA groups in ternary polymers in determining their aggregation dynamics, exhibiting that this induces conformational fluctuations and in general, results in the formation of loosely packed, somewhat extended aggregates, particularly in the case when the groups are randomly distributed along the polymer backbone. Analysing the effect of polar sub-

units on the binding energies of the inter-polymers in the aggregate showed that replacing some of the hydrophobic groups by polar groups disperses the overall hydrophobicity of the aggregates while retaining the total attractive van der Waals interactions and counteracting the strong repulsive electrostatic interactions between the cationic groups. The HEMA groups also form attractive electrostatic interactions with both charged AEMA and polar HEMA groups further contributing to aggregate formation. Nonetheless, the overall hydrophobicity which drives the aggregation binding and stability is significantly reduced in the ternary aggregates. Such polymers therefore make weaker aggregates in solution phase than those with a higher content of hydrophobic groups. This can have a profound effect on the interaction of the polymers with bacterial membranes as it has been shown that one of the driving forces for partitioning of the polymers from aggregates into the membrane is the relative interaction energy experienced by the polymer in the aggregate and the polymer-membrane interaction energy [86, 202]. The weak ternary aggregates, upon interacting with bacterial cell membrane, might therefore drive faster dissociation of polymers from the aggregate and consequent polymer insertion and membrane disruption, due to polymer-lipid head groups interactions becoming favourable over polymer-polymer interaction more easily, compared to the densely packed, stable binary aggregates. Therefore, such weak aggregates can positively impact the lysing action of synthetic antibacterial polymers on bacterial cell membranes. In Chapter 7, we probe in detail the interactions of such ternary biomimetic polymers with model bacterial membrane, to determine the role of polar HEMA groups in regulating the behaviour of such polymers in membrane phase.

Chapter 6

Role of anionic groups in the conformational landscape of biomimetic polymers in solution

6.1 Introduction

Antimicrobial polymers (AMPolys) have largely been designed as binary monomer system consisting of two key components: hydrophobic and cationic functional groups. The antimicrobial action and selectivity of such AMP-mimetic antimicrobial polymers is optimized by adjusting the ratio, identity and spatial arrangement of these two functionalities. However, naturally occuring AMPs typically contain a range of different functionalities in their design, with the design optimized evolutionarily to ensure potent antimicrobial action and selectivity [16, 18, 102, 103]. Binary AMPolys, by their very design, will generally fail to emulate such compositional optimization, which suggests the inclusion of additional functional moeities in the design of AMPolys [19, 104]. While naturally occurring AMPs generally display an overall charge of around +2 to +9, many AMPs such as defensin, magainin, LL-37,

contain anionic amino acids in their sequences [20, 105, 106]. For instance, human cathelicidin AMP LL-37 contains 11 cationic amino acid residues (Lys and Arg) and 5 anionic amino acid residues (Asp and Glu), giving net positive charge of +6 [105]. A natural question then arises - What is the role played by each of the charged moieties?

For AMPs interacting primarily with bacterial membranes which contain ample number of anionic lipids, it is important to understand the specific functional or structural role played by anionic residues, since such a design feature can potentially be mimicked to design effective AMPolys. In this context, the role of salt bridge formation in protein structure and function has long been explored- salt bridge interactions between anionic and cationic amino acids contribute to the structural stability of proteins and can play a significant role in determining the conformational landscape [219, 220, 221]. In case of de novo design of short helical peptides [222], it has been shown that the intra peptide salt bridges tend to stabilize the helical conformation and similar implications of stability via salt bridges has also been proposed for other cell-penetrating α-helical and β-sheet antimicrobial peptides [20, 106]. Interestingly, presence of salt bridges in AMPs such as α-defensin antimicrobial peptides has been shown to induce increased structural flexibility, which enhance peptide sensitivity to proteolysis, in addition to conferring stability [21].

In this chapter, we explore the structural effect of inclusion of negatively charged monomers in biomimetic polymers, in particular, investigating the formation and lifetime of salt bridges between pairs of oppositely charged groups and the effect of such interactions on specific conformations of the polymer in solution phase, using detailed atomistic molecular dynamics simulations. We show that salt bridge formation is consistently exhibited, which act as transient cross-linkers to affect the polymer conformation, leading to a dynamic switching between compact and extended conformations. This chapter is adapted from work done in Ref. [110],

which is a collaborative work with experimental group, in which experiments were performed to study the functional roles of anionic groups on their antimicrobial and hemolytic activities and the conformation of polymer chains in solution phase were studied using atomistic molecular dynamics simulations.

6.2 Models and methods

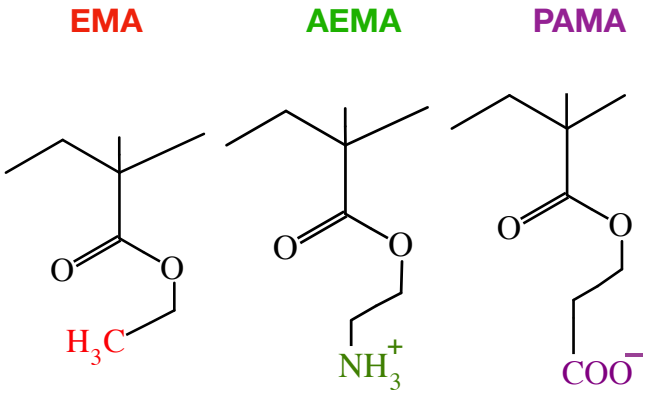

Figure 6.1: Chemical structure of EMA, AEMA and PAMA groups considered in the model polymers.

6.2.1 System set up

Atomistic MD simulations with explicit water and ions were performed on ternary biomimetic polymers, consisting of three monomer units - hydrophobic alkyl (EMA), cationic ammonium (AEMA), and anionic carboxylate (PAMA) moieties (their chemical structures are depicted in Fig. 6.1). We modelled two sequentially different polymer models, both of which have the same proportion of the three monomer units as each other. The two models are referred to as models P1 and P2. For both P1 and P2, we have degree of polymerization (DP) = 20. The number of monomers per polymer chain is taken as follows: 8 for AEMA group, 8 for EMA group and 4 for

Model polymers	DP	Group proportion (AEMA, EMA, PAMA)	Group Sequence
P1	20	+8,8,-4	A-E-A-A-P-E-A-E-P-E-A-A-E-E-P-E-A-P-E-A
P2	20	+8,8,-4	A-E-P-A-E-P-E-A-E-P-E-A-A-E-A-E-A-A-E-P

Table 6.1: Proportion and sequence of groups in the model polymers. Here, A(AEMA), E(EMA) and P(PAMA) are the three monomer subunits forming the polymer chain.

PAMA group. Thus, polymer has a net positive charge of +4, which lies in the range as naturally occurring antimicrobial peptides. The proportions of hydrophobicity and net positive charge have been chosen in accordance with minimum inhibitory concentration (MIC) values deduced from experiments, which suggest the optimality of such composition of monomers in the polymer for its antimicrobial activity [110]. Details of the chemical compositions and sequencing of the groups along the backbone of models P1 and P2 are summarised in Table 6.1.

6.2.2 Simulation protocols

Each polymer model (P1 and P2) was inserted in aqueous phase modelled by TIP3P water [198]. Since the net charge of a single polymer chain was +4, appropriate number of Na^+ and Cl^- ions were added to neutralise the system and maintain 150 mM salt concentration in both cases. All simulations were performed with the NAMD 2.9 simulation package [175]. Each polymer system was first energy minimised for 1000 steps with the conjugate gradient method and simulations were then performed with a 2 fs timestep in the NPT ensemble for 300 ns. Constant temperature was maintained at 305 K with Langevin dynamics at a collision frequency of 5 ps^{-1} and a pressure of 1 atm was maintained through Langevin piston [194, 195]. Electrostatic interactions were calculated by Particle Mesh Ewald method [212] and the cut-off for Lennard-Jones interactions was set to 12 Å, with smoothing starting from 10 Å. The parameter values for the polymers were adopted from the CHARMM force

fields [213] and previous simulations [100, 101, 202]. Visual Molecular Dynamics (VMD) with its embedded TCL scripting language was used for data visualisation and analysis [180].

6.3 Results

6.3.1 Shape measure

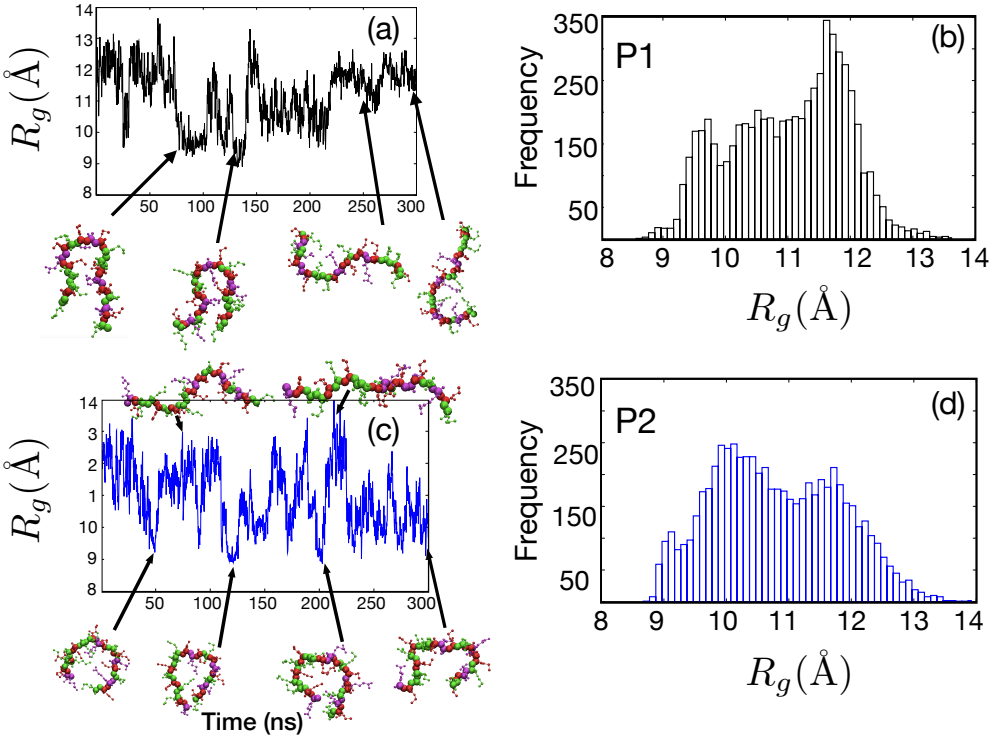

Figure 6.2: Time evolution of radius of gyration (R_g) and frequency distribution of the R_g values for both the model polymers (P1: black and P2: blue). Representative snapshots to illustrate the conformations of the polymers are also presented, with arrows indicating the corresponding simulation time and R_g values. The constituent functional groups of the polymers are illustrated as - hydrophobic (EMA, red); cationic (AEMA, green); anionic (PAMA, magenta).

Model polymers (P1 and P2), due to the dissimilar sequencing of the constituent functional groups (AEMA, EMA, PAMA) along the polymer backbone, show distinct variations of conformations and properties as a function of simulation time

in solution phase. A measure of the shape and stability of a polymer is given by its radius of gyration, R_g [216], defined as the root mean square distance of the constituents of the polymers from its center of mass. We plot R_g of the two model polymers (P1 and P2) as a function of simulation time in Fig. 6.2, with representative snapshots of the polymers shown at intervals. The R_g values and the representative snapshots show that both model P1 and P2 polymers dynamically switch between relatively compact and extended conformations, with the model P1 polymer showing a tendency to adopt a more extended conformation over the last 50 ns of simulation time whereas model P2 polymer showing a tendency to adopt a compact, ring-like structure in the last 50 ns of simulation time.

6.3.2 Electrostatic interaction strength

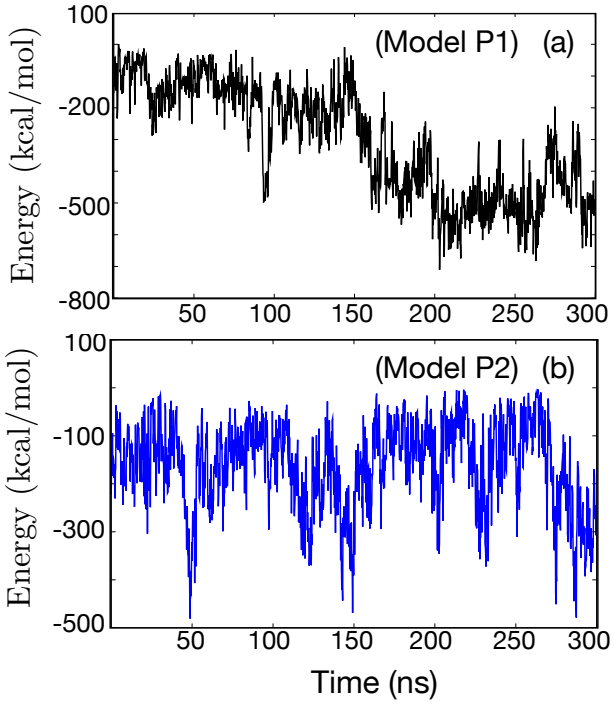

Figure 6.3: Total electrostatic energy between the anionic PAMA groups and cationic AEMA groups is plotted as a function of time, for (a) polymer model P1 and (b) polymer model P2.

Next, we examine the interaction between the oppositely charged carboxylate and

ammonium groups. For this, we first compute the total electrostatic energy between these two groups for both model polymers (P1 and P2), as shown in Fig. 6.3. Expectedly, the cationic (AEMA) and anionic (PAMA) groups show attractive interactions. Model P1 polymer, with two cationic groups at its termini, shows interactions which grow uniformly more attractive with time. The total attractive electrostatic energy in this case registers a steep rise between 150 ns - 200 ns of simulation time, before stabilising in the last 50 ns of simulation time, with the polymer adopting an extended conformation consistently, as deduced from the R_g values. On the other hand, model P2 polymer, which has an anionic group at one end and a cationic group at the other end, shows large fluctuations in the total electrostatic energy as a function of simulation time. In this case, the interactions generally stay less attractive but register steep increase in the attractive energy intermittently, before uniformly growing more attractive over the last 50 ns of simulation time as the polymer adopts a compact structure consistently.

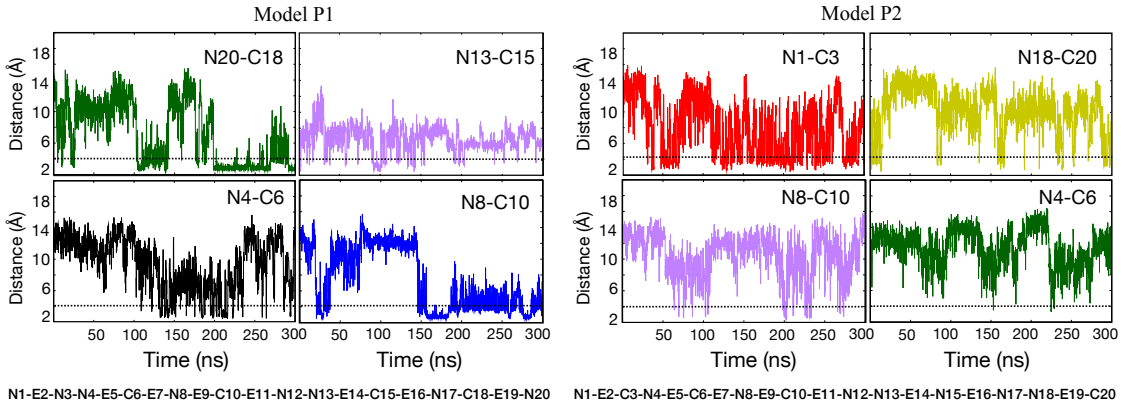

Figure 6.4: Time evolution of distance between the nitrogen atom of NH_3^+ in AEMA group and the two carboxyl oxygen atoms of COO^- in PAMA group is plotted to investigate the lifetime and stability of salt bridge formation between sequentially neighbouring cationic and anionic groups along the polymer backbone for polymer models P1 and P2. (a) For model P1, time evolution of distance between N20-C18, N13-C15, N4-C6 and N8-C10 is presented. (b) For model P2, time evolution of distance between N1-C3, N18-C20, N8-C10 and N4-C6 is presented. Bottom: we mention the sequencing of the various functional groups along the polymer backbone for polymer model P1 and P2, with N denoting cationic ammonium, E denoting hydrophobic and C denoting anionic carboxylate moieties. In all figures, black dotted line indicates the distance of 4Å.

6.3.3 Salt bridge formation and lifetime

To further probe the significance of the presence of the anionic groups, we investigated salt bridge formation between the pair of oppositely charged groups: the anionic carboxylate (PAMA) and the cationic ammonium (AEMA) moeities. Salt bridge formation is deduced for a pair of oppositely charged side chain groups if the distance between the nitrogen atom of (NH_3^+) and the two carboxyl oxygen atoms of (COO^-) is less than 4.0 Å [223]. A natural question in this context is to investigate the formation and stability of salt bridges between sequentially neighbouring groups and between groups that lie farther from each other along the polymer backbone. We first deduce that salt bridges are more commonly formed between sequentially neighbouring groups along the polymer backbone, though it is notable that not all neighbouring oppositely charged groups form salt bridge. In Fig. 6.4, we show the time evolution of the salt bridges formed between the cationic and anionic groups, for both the model polymers (P1 and P2), for some neighbouring groups. We note that salt bridge formation between neighbouring groups shows good stability, particularly in last 50 ns of simulation time, in case of the polymer P1 as compared to the case of polymer P2. This is indicative of the tendency of the P1 polymer to adopt an extended conformation, as compared to the P2 polymer which shows a tendency to adopt a compact conformation in the last 50 ns of simulation time. This is further reiterated when we probe the formation of salt bridges between groups that lie away from each other along the polymer backbone, as depicted in Fig. 6.5. In this case, the salt bridges formed are not as stable as the case of the salt bridges formed between neighbouring groups. However, we note that in case of the P1 model polymer, the salt bridges are formed for groups that lie relatively close to each other and are formed in a limited interval of simulation time before disintegrating. In contrast, in the P2 model polymer case, the salt bridges are formed between groups that lie near the termini of the polymer and these salt bridges undergo a cycle of

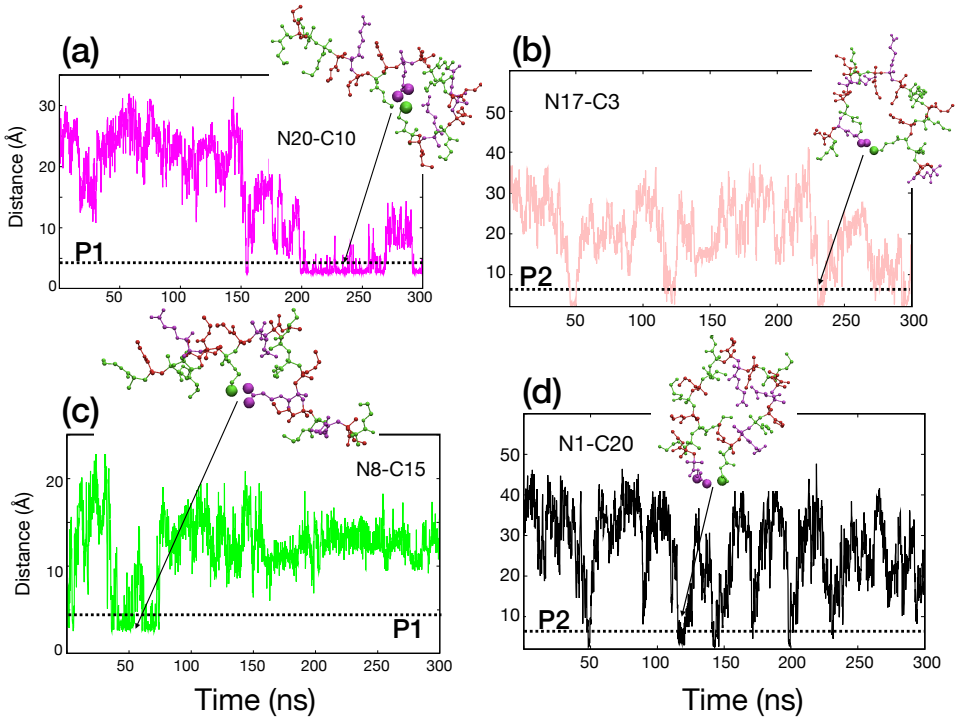

Figure 6.5: Time evolution of distance between the nitrogen atom of NH_3^+ in AEMA group and the two carboxyl oxygen atoms of COO^- in PAMA group is plotted to investigate the lifetime and stability of salt bridge formation between cationic and anionic groups placed far away from each other along the polymer backbone, for polymer models P1 and P2. For model P1, time evolution of distance between N20-C10 and N8-C15 is presented. For model P2, time evolution of distance between N17-C3 and N1-C20 is presented. Representative snapshots of the polymers are shown with arrows pointing to the corresponding distance between nitrogen (shown as green ball) and oxygen atoms (shown as magenta balls) and simulation time. Note that the sequencing scheme of the functional groups along polymer backbone for both the model polymers is shown in Fig. 6.4. In all figures, the black dotted line indicates the distance of 4Å.

formation and disintegration. Indeed, the groups N1 and C20, which lie at the ends of the polymer chain, form salt bridge (Fig. 6.5(d)) that undergoes a periodic cycle of formation and breaking, with concomitant adoption of a very characteristic ring-like compact conformation. It is notable that while both the polymers persistently switch between extended and relatively compact conformations, this characteristic ring-like conformation is specific to the P2 model polymer, highlighting the influence of the formation of salt bridge between the terminal groups in underpinning the adoption such ring-like conformations. Further, we also note that the salt bridge

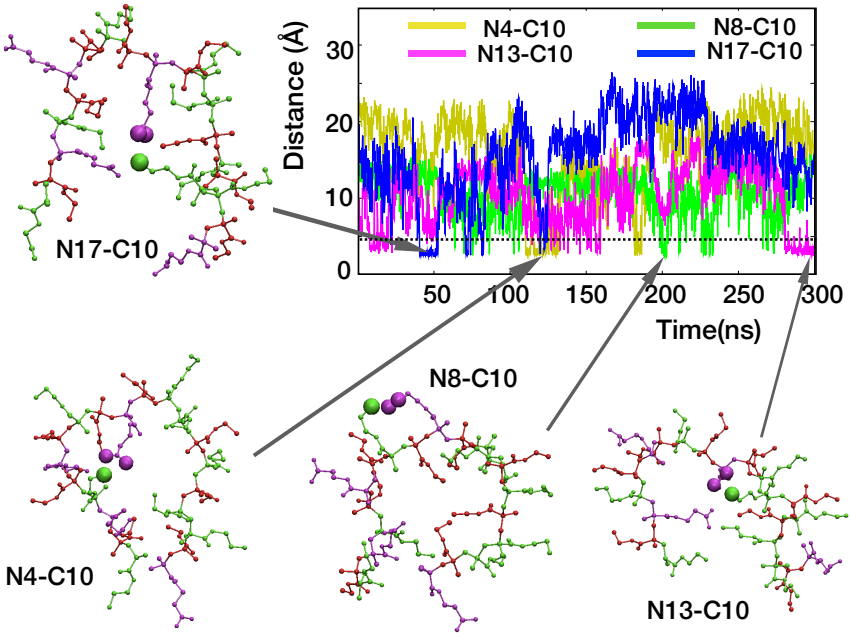

Figure 6.6: Time evolution of salt bridge formation between C10 and cationic ammonium groups of polymer model P2. Representative snapshots of the polymers are shown with arrows pointing to the corresponding distance between nitrogen (shown as green ball) and oxygen atoms (shown as magenta balls) and simulation time. The black dotted line indicates the distance of 4Å.

formed between N17-C3 shows a measure of stability in the last 30 ns of simulation time for the P2 model polymer, which also abets the tendency of the polymer to adopt a relatively stable compact conformation. This supports our conclusion on the effect of the salt bridge between distant lying oppositely charged groups on the ring-like conformation.

Next, we ask the question- Do the same pair of oppositely charged functional groups tend to form salt bridges between themselves or are they shuffled with other charged groups along the polymer backbone? To probe this, we consider carboxylic group C10, belonging to polymer model P2, as representative case. It is located in the center of the polymer chain, allowing it to plausibly interact with all cationic groups in the polymer chain. We then find that C10 forms salt bridges consistently with neighboring cationic groups N8 and N13, and with sequentially distant N4 and N18 for small pockets of time. This suggests that each salt bridge is intermittently formed,

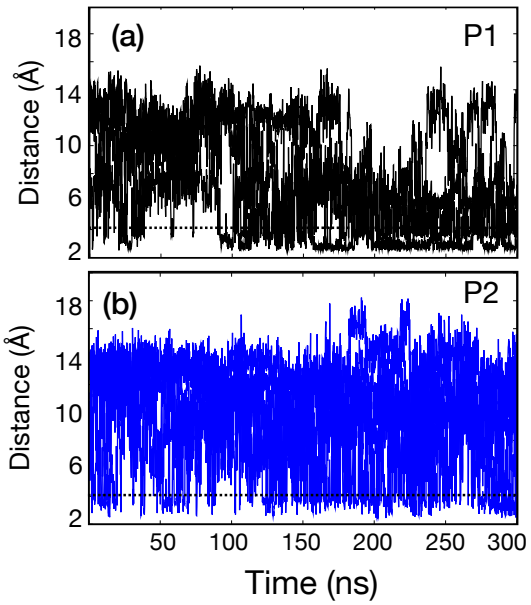

Figure 6.7: Time evolution of distance between nitrogen atom and carboxyl oxygen atoms for several pairs of AEMA and PAMA groups is depicted together for (a) model P1, and (b) model P2. The black dotted line indicates the distance of 4Å.

and the pairs are consistently changed, resulting in an effect of transient crosslinking of the polymer chain effected by the salt bridges (Fig. 6.6). The favourable formation of salt bridge between the neighbouring groups is reasonable because they are spatially close, and thus their formation does not require large changes in the polymer conformation. However, C10 also forms salt bridge with sequentially distant N4 and N18, likely due to the compact polymer conformation, which brings these groups close enough to C10. Alternatively, the salt bridge-mediated crosslinking of polymer chains also contributed to the formation of the compact polymer conformation.

Finally, we plot the distance between various possible ion-pairs for the two model polymers (P1 and P2), as shown in Fig. 6.7. We can then conclusively infer that salt bridge formation is consistently exhibited for both the model polymers, particularly after around 100 ns of simulation time. Further, it is interesting to note that multiple salt bridges can be formed simultaneously along the polymer chain, as shown in the representative snapshots of the polymer conformation in Fig. 6.8, which indicates that the polymer chain is crosslinked by multiple transient bridges, similar to natural

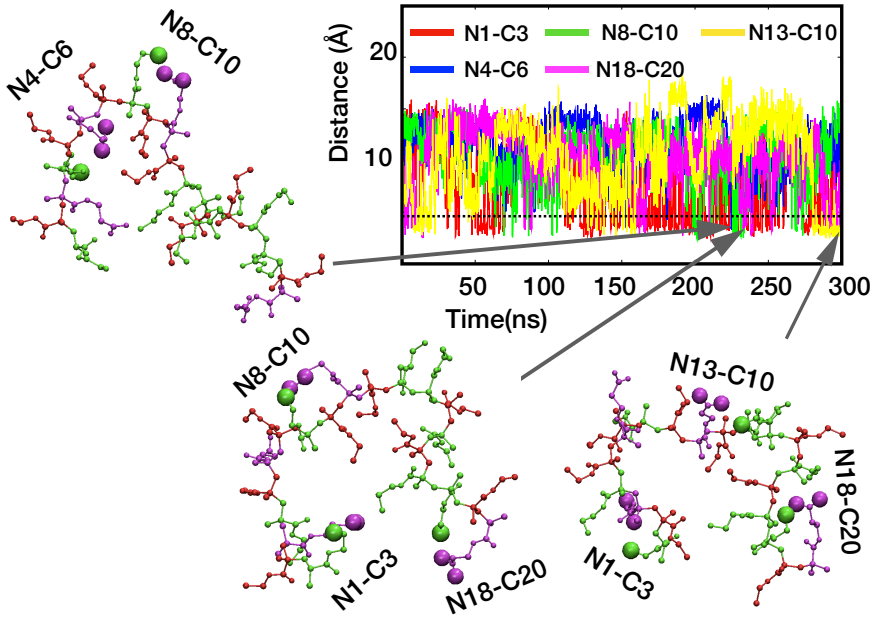

Figure 6.8: The plot of the distance between various possible ion-pairs of model P2, with arrow-head showing formation of multiple salt-bridges at the same time, nitrogen shown as green ball and oxygen atoms shown as magenta balls. The black dotted line indicates the distance of 4Å.

peptides and proteins [224]. Taken all together, our results show that salt bridges act as transient cross-linkers, which controls dynamics of compact and extended polymer conformations. However, the salt bridges do not exert the polymers to adopt specific conformations.

6.4 Discussion

In this chapter, we investigated the role of inclusion of negatively charged monomers in the biomimetic polymers, in formation of salt bridges with the positively charged monomers and conferring specific conformations to the polymers. Our analysis of the simulation data, including of the shape parameter values and electrostatic interactions between the anionic carboxylate and cationic ammonium groups, show that the model polymers dynamically switch between compacted and extended conformations, with the sequence of the functional groups along the polymer backbone

playing a role in influencing the conformational dynamics and indicating the formation of salt bridges between pairs of cationic and anionic groups, which is also borne out by pH titration experiments [110]. To understand the formation and stability of salt bridges, we analysed the distance between various possible ion-pairs for model polymers considered. We established that salt bridge formation is consistently exhibited, particularly after around 100 ns of simulation time. Indeed, our analysis shows that multiple salt bridges can also be formed at the same time, similar to natural peptides and proteins [224]. Our simulations thus provides direct evidence of the formation of salt bridges between various pairs of oppositely charged functional groups in the polymer. We established that the possible role of the salt bridge is to provide transient cross-linking of polymer chains, which can eventually control the dynamics of compact and extended polymer conformations. However, it is notable that the salt bridge do not facilitate adoption or stabilization of a specific conformation throughout simulation time scale. This in particular suggests that salt bridges do not directly determine the antimicrobial activity and selectivity of the AM polymers, through their structural roles. This is in agreement with the assay results which suggest that there was no distinctive effect of the anionic groups on the antimicrobial and hemolytic activities of the polymers [110].

Our results are in broad agreement with previous study which also indicated that salt bridge formation in α-defensins does not directly control the antimicrobial activity [21]. However, it has been demonstrated that such salt bridge formation in α-defensin facilitate the formation of correct disulfide pairs in the peptide, which are essential for the folding to the active peptide conformation [225]. Therefore, this suggests that salt bridge in polymer chains also likely work as a provisional "adhesive" which enable the polymer chains to adopt compact conformations but without locking, thus bringing all the constituent groups closer which can catalyse the interactions between the designed specific groups for covalent bond formation.

In this chapter, we investigated the conformations of single polymer chains in solution phase. However, it is possible to design and explore the role of the anionic groups of polymers in enhancing the interactions between polymer chains and the formation of polymer assembly for potent antimicrobial activity. For instance, it has been reported that the presence of anionic residues can promote oligomerization between antimicrobial peptides PGLa and magainin 2 on bacterial cell membranes [226], which leads to synergistic effects in their antimicrobial activity. Such explorations for antimicrobial polymers will be carried out in a future work.

Chapter 7

Role of polar groups in interaction of antimicrobial polymers with model bacterial membrane

7.1 Introduction

Molecular dynamics simulations have been used extensively to understand the interactions of methacrylate polymers and model cell membranes. Most of the previous simulation studies have focussed on binary methacrylate polymers consisting of cationic and hydrophobic side chains distributed along the polymer backbone [100, 101, 202, 227]. For instance, in an early simulation study of designed biomemetic polymers based on methacrylate moieties, it has been shown that design parameters such as polymer length, sequence (arrangement of different groups along the polymer backbone) and composition (ratio of hydrophobic to cationic units) can play crucial role in the AM polymers attaining configurations in aqueous solution and their interactions with equilibrated dioleoyl phosphatidylcholine (DOPC) bilayer patch [100]. More recent MD simulation studies have also investi-

gated the interaction of multiple methacrylate binary polymers with model bacterial membrane and their impact on bilayer properties [202, 227]. These polymers form an aggregate, micellar-like structure in solution phase, which upon reaching the membrane-water interface bind to the bacterial membrane surface. After insertion, the polymers dissociate from the aggregate and disperse into the bilayer, acquiring facially amphiphilic conformations with spatial segregation of groups, with the hydrophobic groups preferring deeper membrane core and the cationic ammonium groups staying closer to the lipid head groups.

The studies involving biomimetic methacrylate binary polymers capture some of the essential features, including the antimicrobial activity of the AMPs. However, as discussed, it is not easy to satisfactorily optimize this simple design for both antimicrobial activity and desired selectivity, necessitating the design of AMPolys which go beyond the traditional binary composition and include a variety of functional groups. Indeed, recent experimental studies have studied ternary biomimetic polymers and have studied their antimicrobial and hemolytic activity [23, 209, 210]. In Chapter 5, we studied the aggregation dynamics of ternary biomimetic methacrylate polymers, composed of hydrophobic, cationic and neutral polar groups, where we showed the effect of the inclusion polar groups in inducing conformational fluctuations and in weakening the polymer aggregate. It is notable that "weak aggregation" can be of crucial importance in the bactericidal activity of such polymers, since polymer chains can more easily dissociate from the aggregates, facilitating insertion and disruption of the cytoplasmic membrane to cause cell death [86, 202, 204]. Thus, a natural question is to examine the interaction of ternary polymers with bacterial membrane, since an effective antibacterial action of such polymers, combined with their propensity for forming weak aggregates and their low hemolytic activity [23], can result in design of potent antimicrobial agents.

In this chapter, we study the interaction of ternary polymers, composed of charged

cationic, hydrophobic and neutral polar groups, with model bacterial membrane using detailed atomistic molecular dynamics simulations and compare it with the action of binary polymers, composed only of charged cationic and hydrophobic groups, on model bacterial membrane. We also investigate the role played by sequence of polar groups in influencing the interaction of such polymers on the bacterial membrane, by considering polymer models having block as well as random arrangements of these groups along their backbones. Our simulation data shows that random ternary polymers can penetrate deep into the membrane interior, with even a single polymer having a pronounced affect on the structure of the membrane. To understand the effect of polymer binding on membrane configuration, we examine lipid reorganization in the vicinity of the model polymers in membrane phase and observe the strong affinity of the ternary polymer for POPG lipids, resulting in substantial lipid reorganization in polymer neighbourhood in this case. Membrane mode of insertion were also observed to be significantly different for binary and ternary polymers. Traditional binary polymer exhibits acquired amphiphilic conformation upon membrane insertion, with cationic ammonium groups localizing close to the interfacial lipid head groups and the hydrophobic moieties buried deeper within the hydrophobic tails of the bilayer. On the other hand, we show that a clear segregation of groups is absent in random ternary polymer case, as had been surmised in previous experimental work [23], with the polymer in this case assuming a more folded conformation, staying aligned in the direction of the membrane normal. Finally, we study interactions of aggregates of binary and ternary polymers with bacterial membrane, showing that the weaker ternary aggregate undergoes fairly rapid partitioning and subsequent membrane insertion while polymer partitioning is robustly obstructed in case of the strong binary aggregates.

7.2 Models and methods

7.2.1 System set up

We performed atomistic MD simulations with explicit water and ions on binary as well as ternary biomimetic polymers and studied their interactions with model bacterial membrane. Ternary methacrylate random polymers (referred to as "model T"), consisting of cationic ammonium (amino-ethyl methacrylate: AEMA), hydrophobic alkyl (ethyl methacrylate: EMA) and polar hydroxyl (hydroxyl methacrylate: HEMA) groups as shown in Fig. 5.1, are modelled with degree of polymerization (DP) = 19 [23]. The constituent functional groups are taken in the same proportion as that considered for ternary polymers in Chapter 5 (6 AEMA groups, 8 EMA groups and 5 HEMA groups). We also consider a second ternary polymer model (referred to as "model Tb"), which has the same proportion of groups, but is sequentially different from model T polymer. In this case, the AEMA groups and EMA groups are arranged randomly but the HEMA groups are arranged in a block sequence at one end of the polymer backbone. Further, to highlight the role of inclusion of neutral polar functional groups, we also perform control simulations without them, involving only binary compositions of cationic (AEMA) and hydrophobic (EMA) monomer units in random configuration and with same degree of polymerization as ternary polymers. The proportion of the constituent functional groups is the same as "model B" polymer in Chapter 5 (6 AEMA groups and 13 EMA groups). The proportion and sequence of the groups along the three model polymers is summarised in Table 7.1.

For bacterial membrane, the starting configuration was taken from a pre-equilibrated membrane patch consisting of 38 POPG and 90 POPE lipid molecules per leaflet, as described in Chapter 4. This is in similar ratio (3:7 POPG to POPE) as the inner membrane of the Gram negative bacteria *E.coli* [22].

Model polymers	DP	Group proportion (AEMA, HEMA, EMA)	Group Sequence
Ternary (T)	19	+6, 5, 8	E-H-A-E-H-A-H-E-A-E-E-A-E-H-H-A-E-E-A
Ternary (Tb)	19	+6, 5, 8	E-A-A-E-E-A-E-E-A-E-E-A-E-A-H-H-H-H-H
Binary (B)	19	+6, 0, 13	E-E-A-E-E-A-E-E-A-E-E-A-E-E-E-A-E-E-A

Table 7.1: Proportion and sequence of AEMA (A), HEMA (H) and EMA (E) monomers in the polymer models (T,Tb and B). In all the model polymers, degree of polymerization (DP) = 19 and the number of cationic side chain groups are fixed to be 6 per polymer. Model T and Tb are compositionally same, but differ in sequence of the three groups along the polymer backbone

7.2.2 Simulation protocols

Single polymers were simulated in a box ($\approx$ 50 Å $\times$ 50 Å $\times$ 50 Å) of TIP3P [198] water model before placing them near the membrane environment. Since the total charge of a single polymer in each of the system was $+6e$, an appropriate amount of NaCl salt was added to neutralize the systems and maintain 150 mM salt concentration to mimic physiological conditions in each case. The total number of atoms in this simulation system was $\sim$ 10500. All simulations were performed with the NAMD simulation package [175]. Each polymer system was first energy minimized for 1000 steps with the conjugate gradient method and simulations were then performed with 2 fs timestep in the NPT (T = 305 K and P = 1 atm) ensemble for 200 ns.

Single polymer-membrane systems

To construct the membrane-polymer system, a randomly chosen equilibrium configuration, from above solvent simulations, of each of the single model polymer (models T, B and Tb) was randomly placed in the vicinity of one of the bilayer (referred to as upper leaflet) along the membrane normal in the TIP3P water phase and required number of counterions of Na^+ and Cl^- were added to neutralize the system and maintain 150 mM salt concentration. These three different polymer-

membrane ensembles (consisting of membrane and polymer models T, B and Tb, respectively) were simulated with periodic boundary conditions in the isothermal - isobaric (NPT) ensemble. The latest CHARMM force fields CHARMM 36 were used for lipid molecules [184]. The parameter values for the polymers were adopted from the CHARMM force field [213] and previous simulations [100, 101, 202]. The total number of atoms for the polymer-membrane systems simulated was $\sim$ 71000. Constant temperature was maintained at 310 K, which is above the main-phase transition temperature of both POPE and POPG lipid molecules [228] and a pressure of 1 atm was maintained through Langevin piston [194, 195]. Electrostatic interactions were calculated by the Particle Mesh Ewald method [212] and the cut-off for Lennard-Jones interactions interactions was set to 12 Å, with smoothing starting from 10 Å. The polymer-membrane systems were first energy minimized using conjugate gradient method and simulations were conducted with a 2 fs timestep. Polymer in each case was initially subjected to harmonic restraint which was gradually reduced to zero over 2 ns. Systems with binary model B-membrane and ternary model Tb-membrane were simulated for 700 ns, whereas the random ternary model T-membrane system was simulated for 900 ns. Simulation details for the single polymer-membrane systems are summarised in Table 7.2.

Polymer aggregate-membrane systems

To study membrane interactions of polymer aggregates, multiple binary and ternary polymers were dispersed in a box of TIP3P water and sufficient counterions to maintain 150 mM salt concentration. This system was simulated for 150 ns in NPT conditions, from which we then extracted the largest formed stable aggregates of binary and ternary polymers. Both these aggregates consisted of four polymers, four binary polymers (denoted B1, B2, B3, B4) in case of the binary aggregate and four ternary polymers (denoted T1, T2, T3, T4), in case of the ternary aggregate. These

Model	Time(ns)
Single polymer in TIP3P water, NPT emsemble (T = 305 K, P = 1 atm)	
1. Model B	200 ns
2. Model T	200 ns
3. Model Tb	200 ns
Interaction of single polymer with model membrane, NPT ensemble (T = 310 K, P = 1 atm)	
1. Model B	700 ns
2. Model T	900 ns
3. Model Tb	700 ns
Interaction of aggregate with model membrane, NPT ensemble (T = 310 K, P = 1 atm)	
1. Model B aggregate	350 ns
2. Model T aggregate	300 ns

Table 7.2: Simulation times in each case for the single polymer-water solution, single polymer-membrane and polymer aggregate-membrane systems. The number of POPG and POPE lipids per leaflet are 38 and 90 respectively.

aggregates of binary and ternary random polymers were then randomly placed in the vicinity of the upper leaflet and simulated for atleast 300 ns in NPT ensemble. The total number of atoms for the aggregate-membrane simulations was $\sim$ 80000. All the parameters and conditions for the aggregate-membrane systems were kept the same as the single polymer-membrane systems. Simulation details for the polymer aggregate-membrane systems are summarised in Table 7.2.

For analysis and visualization, the VMD package [180] analysis tools was used. All the analysis for the membrane-polymer systems is performed using plugins and TCL scripting language embedded with VMD.

7.3 Results

Both binary and ternary polymers, owing to the presence of amino groups which are cationic in nature, get attracted towards PG lipid groups of the bacterial membrane

through electrostatic interactions [73]. In our case, for all three polymer - membrane systems that were simulated, single polymer placed in water quickly approached the membrane patch within a few nanoseconds and localized close to the nearest membrane leaflet (referred to as the upper leaflet). However, after contact with the leaflet, significant differences were observed in the conformation of the three polymers, which we delineate in this section. Our objective is to study the role of the presence of the HEMA groups and their arrangement along the polymer backbone in governing the polymer-membrane interaction.

In Fig. 7.1, the time evolution snapshots of the polymer - membrane systems is depicted over the entire simulation timescale. It is clear that different bacterial membrane-polymer models display remarkably different interaction mechanisms. For the polymer with no HEMA group (model B with AEMA and EMA groups randomly distributed, mimicking random binary polymer), the presence of charged cationic groups ensure that it rapidly comes into contact with the membrane surface and subsequently, penetrates completely into the membrane core around timescale $\sim$ 150 ns, due to the abundance of hydrophobic groups in the polymer. Visual inspection reveals that the polymer backbone becomes parallel to the membrane surface upon penetration, with the hydrophobic groups projected towards the membrane core and the cationic ammonium groups projected towards the water - membrane interface (Fig. 7.1(A)).

For the random ternary polymer with HEMA group (model T with AEMA, EMA and HEMA groups forming random ternary polymer), again the presence of cationic groups ensure that the polymer comes into contact with the membrane surface within first few nanoseconds, however in this case complete penetration of the polymer into the membrane interior is hampered. This is likely due to the presence of HEMA groups, since in this case the overall hydrophobicity of the polymer is low. Nonetheless, the trajectories show in this case, the polymer gradually enters

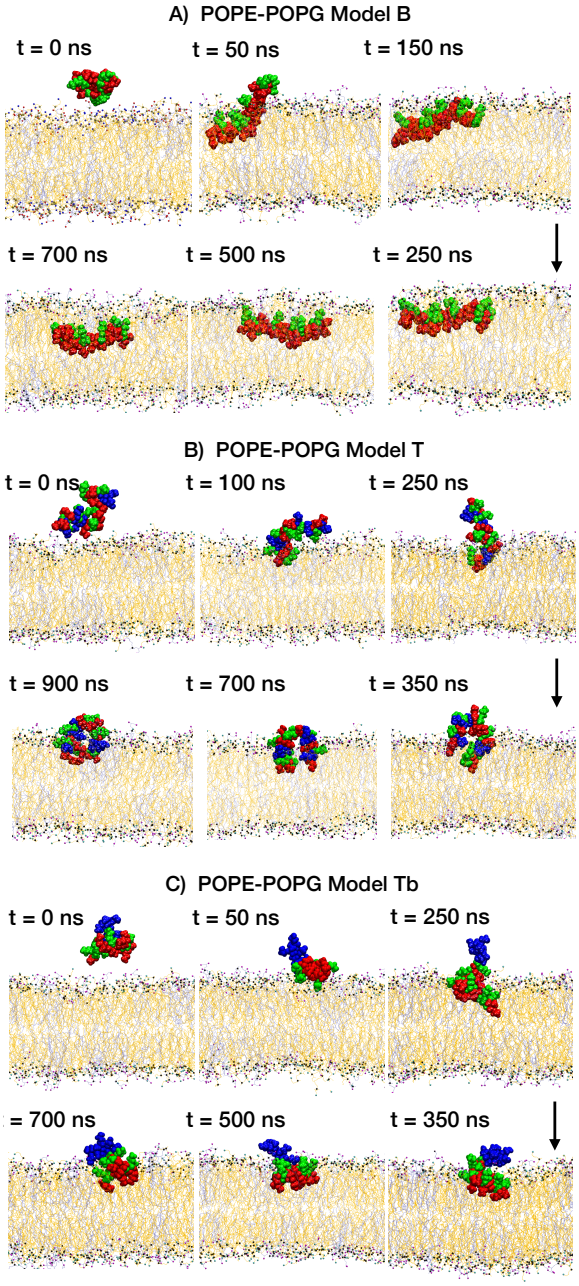

Figure 7.1: Representative snapshots of (A) model B, (B) model T and (C) model Tb, interacting with the bacterial bilayer. The POPE lipids are coloured orange and POPG lipids are shown in ice-blue colour; the lipid head groups are oxygen (magenta), nitrogen (cyan) and Phosphate (black). The cationic, hydrophobic and polar groups of the model polymers are shown in green, red and blue colour respectively.

inside the membrane, with a significant segment of the polymer having penetrated the membrane interior at $\sim$ 250 ns, staying perpendicular to the membrane surface (Fig. 7.1(B)). At around $\sim$ 350 ns, the polymer bends from the other end and eventually, penetrates the membrane from both of its ends, gripping the membrane akin to a holdfast. Subsequently, the polymer assumes an even more folded conformation in the membrane interior (Fig. 7.1(B)), with the EMA groups near both the inserted ends of the polymer coming in contact with each other, while projecting towards the membrane core.

To gain insight into the role played by sequence of polar functional groups in interactions with bacterial membrane, we also performed simulations involving ternary polymer model Tb, having random arrangements of EMA and AEMA groups, and a block of HEMA groups clustered at one end (Table 7.1). Expectedly, the presence of cationic groups ensures that the polymer comes into contact with the membrane surface, which then penetrates into the membrane interior. Interestingly, the block HEMA segment of the polymer consistently remains above the water-leaflet interface (Fig. 7.1(C)), clearly due to favourable polar interactions with water. On the other hand, the hydrophobic groups and the ammonium groups penetrate into the membrane, assuming a segregated conformation very much like the model B polymer, with the hydrophobic groups projecting towards the membrane core and the ammonium groups projecting towards the water-membrane interface. Our aim now is: (a) to quantify the strength of the polymer-membrane interactions for the ternary polymer models and compare it to the binary model, (b) to study the polymer conformation and its evolution in membrane environment and to compare it to their conformation in solution phase and (c) to assess the effect, if any, that the polymer has on the structural properties of the membrane, particularly in the ternary case.

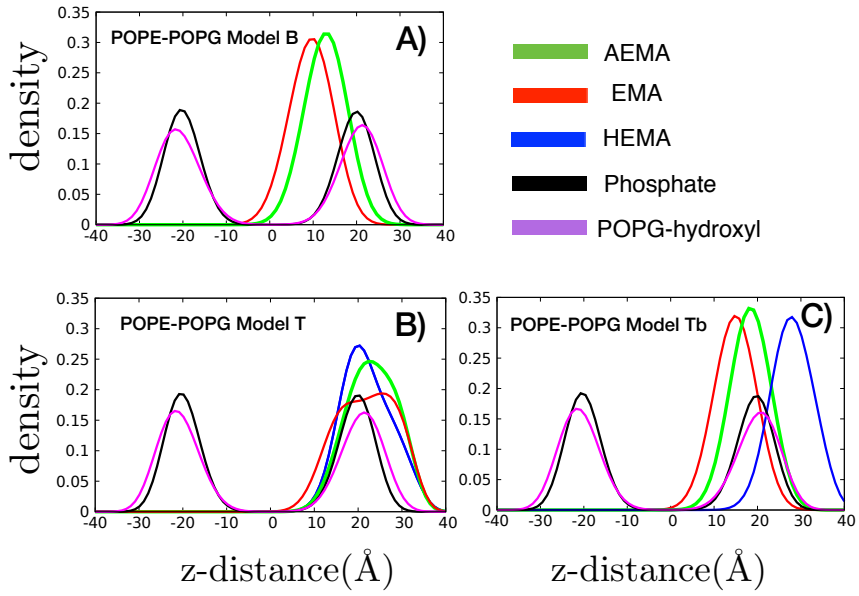

Figure 7.2: Density profiles of various components of lipid-polymer systems, (A) POPE-POPG model B, (B) POPE-POPG model T and (C) POPE-POPG model Tb, averaged over last 50 ns of MD simulations. The green line represents the polymer cationic group, red colour represents the polymer hydrophobic group and the blue colour marks the polymer polar group. The density profile of phosphate atoms, hydroxyl groups of POPG lipids are shown in black and magenta, respectively.

7.3.1 Polymer insertion modes in membrane phase

In this section, we probe in detail the polymer conformation and its evolution, as it interacts with the membrane. For this, we first map the spatial distribution of the various constituent moeities of the polymer models by computing their density profiles along the membrane normal. The z-density profiles averaged over last 50 ns for the three model polymer-membrane systems are shown in Fig. 7.2. We note that model B polymer is inserted into the bacterial membrane with well separated and least overlapping average peaks between AEMA and EMA groups, indicating the spatial segregation of the two groups. The cationic and hydrophobic groups are on opposite sides of the polymer backbone and have thus acquired amphiphilicity, confirming our visual inspection of Fig. 7.1(A). Indeed, previous simulation studies have demonstrated that binary AM polymers can adopt facial amphiphilicity upon

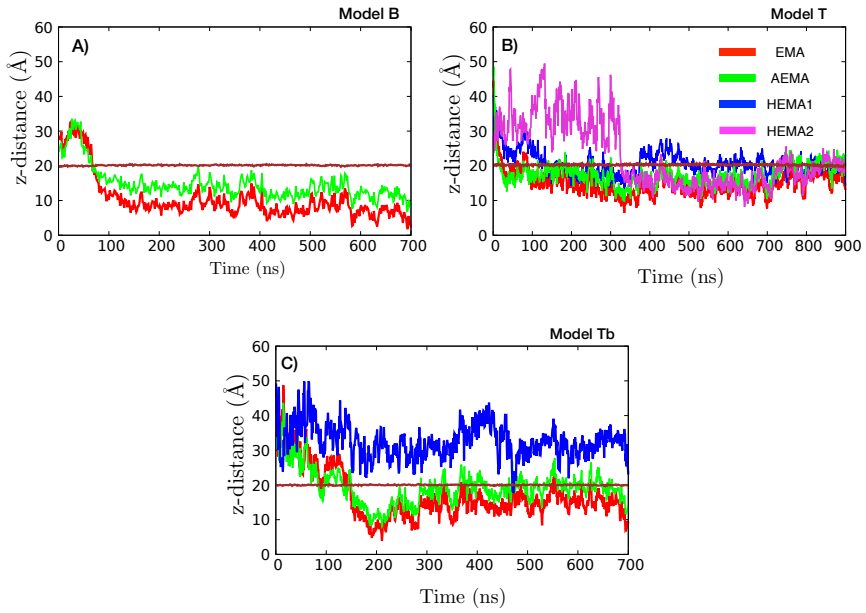

Figure 7.3: Time evolution of center of mass (z-component) of the hydrophobic EMA, cationic AEMA and polar HEMA groups that are lowermost with respect to the bilayer, at the end of simulation time. Note that for model T polymer, we plot the center of mass of two HEMA groups, denoted HEMA1 and HEMA2, placed at the two ends of the polymer. The HEMA2 group is placed at the end of the polymer which inserted into membrane at around $t \sim 350$ ns.

interacting with cell membranes, even though the polymers may themselves lack a secondary structural conformation [99, 101, 202, 229]. We also note that the cationic groups align well with the phosphate head groups of the lipids and the hydroxyl group of POPG lipid, highlighting their preference for interactions with the charged head groups of the bilayer. The average position of the hydrophobic groups clearly indicate insertion well into the membrane core in this case.

For the model T polymer however, the presence of hydroxyl side chain groups in a random configuration obstruct a clear division of the groups and more overlap between the peaks corresponding AEMA, EMA and HEMA groups is observed in the z-density profile as shown in Fig. 7.2(B). On the other hand, the z-density plot for model Tb-membrane system show a much lower overlap between AEMA and EMA groups remarkably similar to model B case, while the HEMA moeities remain outside the membrane interior. Thus, block arrangement of the HEMA groups

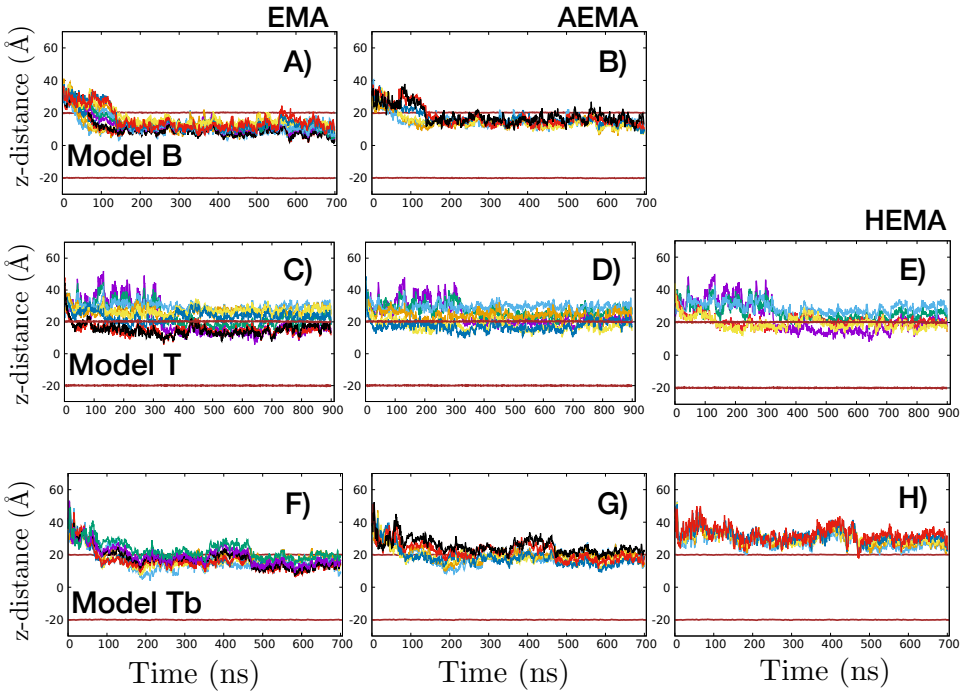

Figure 7.4: Evolution of center of mass (z-component) of hydrophobic, cationic and neutral polar groups for the three polymers - model B (A, B), model T (C, D, E) and model Tb (F, G ,H). Brown lines denote the bilayer phosphate atoms.

clearly facilitates spatial segregation of groups, with the EMA groups preferring the membrane interior, the AEMA groups staying closer to the lipid head groups and the polar HEMA groups preferring aqueous phase. The plots in Fig. 7.2 also show the depth at which the polymers are anchored within the membrane leaflet. Density data shows peak position of cationic AEMA group is deeper for model B and model Tb polymers as compared to the model T case, although further comparing the two ternary models reveals that the three groups (EMA, AEMA, HEMA) of the model T polymer have more average contacts inside the membrane, compared to model Tb polymer, since block HEMA moeities remain localized outside the membrane.

To characterize the onset of the facial amphiphilicity and the placement of the polymer groups with respect to lipid head groups along the membrane normal, we monitor the time evolution of the center of mass of the lowermost groups of the AEMA and EMA groups of models B, T and Tb polymer and HEMA group of

models T and Tb polymer, with respect to the bilayer in Fig. 7.3 (note that for the model T polymer, the two lowermost HEMA residues associated to the two ends of the polymer are plotted). We also compute the evolution of the center of mass of all the groups in the three model polymers with respect to the membrane lipid phosphate head groups in Fig. 7.4. We observe that in all the three cases, polymer placed in water phase quickly approached the membrane-water interface. This is due to the presence of similar proportions of cationic AEMA groups in all the three polymer models, which get attracted towards the anionic head groups of POPG lipids. Interestingly, the hydrophobic side chain and the cationic groups undergo a clear flip just upon entering the upper leaflet surface. This is in good agreement with the flipping observed in previous work [202]. The time evolution of the center of mass well displays the adopted amphiphilic conformation for model B polymer, this facial amphiphilicity being initiated once the polymer inserts into the membrane interior and persisting throughout the simulation time after this.

However, as noted above, a clear segregation of groups is absent for the model T polymer. The positional inclination of the HEMA groups is understood by examining the evolution of the center of mass for groups in the model Tb polymer, where these remain outside the membrane interior throughout the simulation time scale, showing a preference for interactions with water. Again, the evolution of the cationic and the hydrophobic groups in this case are very similar to the case of the model B polymer, with a flipping of the EMA and AEMA groups just upon membrane insertion following which the EMA groups consistently stay below the AEMA groups. However, model Tb moeities maintain a shallower depth in the membrane as compared to the model B case, likely influenced by the attractive electrostatic interactions between the HEMA and AEMA groups, as also outlined in our previous simulation study of aggregation dynamics of ternary polymers in Chapter 5. This indicates that while the cationic and hydrophobic subunits of the model Tb polymer mimic the cationic amphiphilicity of naturally occurring AMPs (Fig. 7.2(C)),

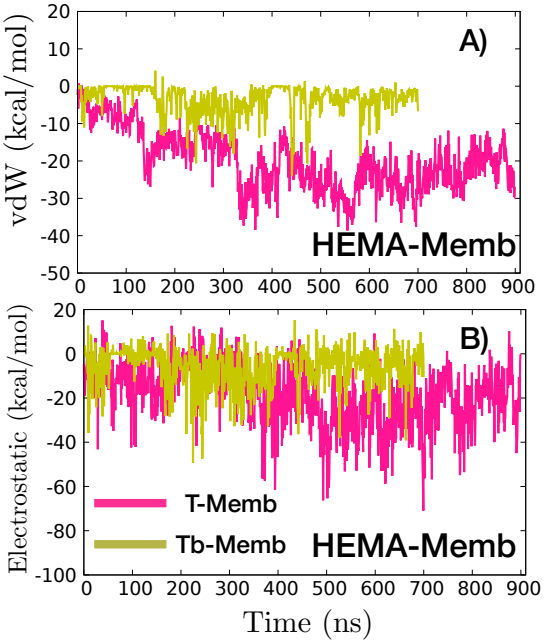

Figure 7.5: (A) Van der Waals and (B) electrostatic energy between the HEMA groups and the bacterial membrane for ternary polymer model T and ternary polymer model Tb. The van der waals energy is clearly more attractive for polymer model T, where HEMA groups are randomly distributed along the polymer backbone, while in model Tb, the block HEMA groups seem to collectively prefer not to penetrate the bacterial membrane surface and favour water environment.

the hydrophilic HEMA block acts as an inhibitor of the antimicrobial action of the polymer by blocking a deeper insertion of polymer into the membrane. To further confirm this, we specifically consider the non-bonded interactions between HEMA groups of the polymers and the bacterial membrane in Fig. 7.5(A) and Fig. 7.5(B). We observe that in the model T case, the HEMA group shows higher van der Waals attraction with the bacterial membrane compared to model Tb (block HEMA in ternary polymer). Even the electrostatic interaction is consistently more attractive in the model T case. From this we can conclude that polymer-membrane interaction is more robust in case of the random ternary polymer, with a block arrangement of polar HEMA groups clearly limiting effective interaction of the model Tb polymer with the bacterial membrane.

We next plot the radial density distributions $g(r)$, for the cationic ammonium groups and the hydroxyl groups of the polymers around the lipid head groups in Fig. 7.6.

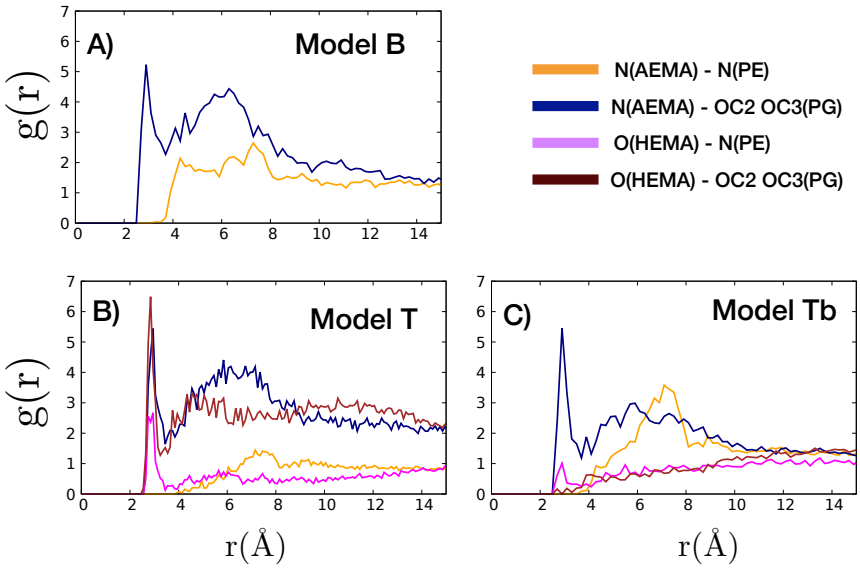

Figure 7.6: The radial density distribution functions for ammonium and hydroxyl groups of polymer models around the head groups of POPE and POPG lipids. Strong propensity of the cationic groups of the polymers to be around the negative head groups of POPG lipids is shown. Also, HEMA groups of the random ternary polymer prefer interactions with lipid head groups due to their polar nature.

Expectedly, this data depicts the strong propensity of the cationic groups (AEMA) of all the three polymer models to bind to overall negatively charged lipid head groups POPG. We further observe in Fig. 7.6(B) and Fig. 7.6(C), that the peak of the primary HEMA groups at $\sim$ 3Å of the lipid head groups show a much higher likelihood for the random ternary polymer model T compared to the model polymer Tb, which has HEMA groups placed in a block at the end of the polymer chain. This suggests that a block arrangement of the HEMA groups leads to their favoring interactions with water completely, while with a random arrangement of the HEMA groups, these groups show ample interactions with the membrane. In summary, we can then conclude that the lack of a clear segregation of groups in case of the random ternary polymer is underpinned by two competitive effects involving the HEMA groups, as demonstrated by the energy analysis and the radial density distribution data - preferable interactions with water, which constrain insertion into membrane and attractive interactions of HEMA group with membrane lipids. A

block arrangement of the HEMA groups, as in case of model Tb polymer, mitigates this effect by completely favouring interactions with water and thus remaining at and above the membrane-water interface.

7.3.2 Morphological changes of the polymers in solution and membrane environment

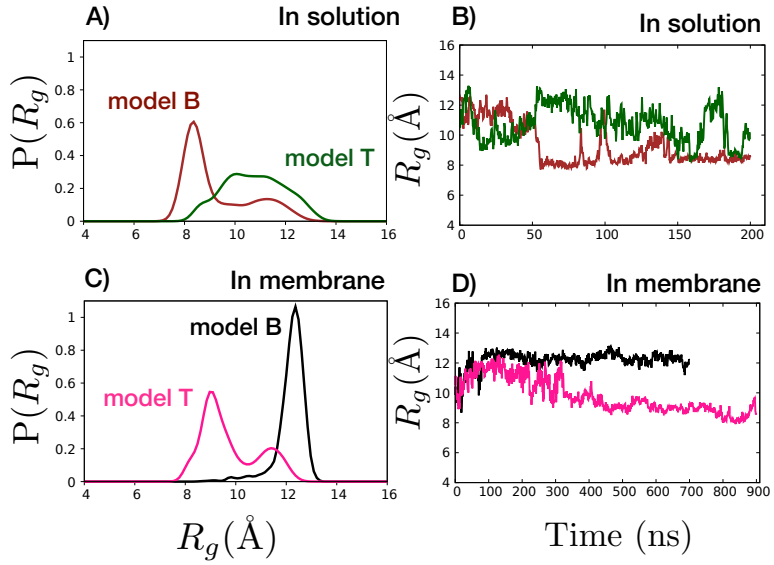

Figure 7.7: (A) Distribution of radius of gyration (R_g), with data sampled over the entire trajectory, for models B and T is shown in solution phase. (B) Time evolution of R_g is shown for both the polymers in solution phase. (C) Distribution of radius of gyration (R_g) for models B and T is shown in membrane phase. (D) Time evolution of R_g is shown for both the polymers in membrane phase.

In this section, we compare the stability and dimensions of the random polymers (models B and T) in solution phase and in lipid phase. The distribution and time evolution of the radius of gyration (R_g) values for models B and T polymers are shown in Fig. 7.7. We observe that the R_g values for binary polymer in solution phase are lower than the ternary polymer (Fig. 7.7(A)), due to the formation of micelle like structure with a hydrophobic (EMA) core enclosed by cationic (AEMA) groups, as shown in the representative snapshot of binary polymer in solution phase at the end of 200 ns (Fig. 7.8(B) (right)). On the other hand, for ternary polymer, the inclusion

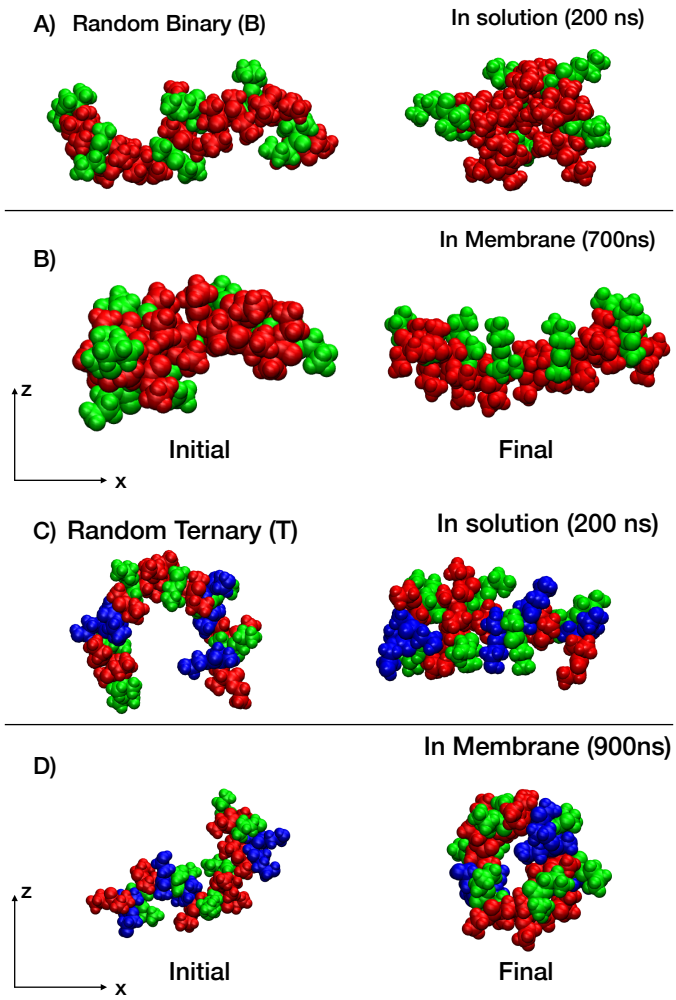

Figure 7.8: Snapshots of initial (left) and final (right) conformations of polymer model B, (A) in solution and (B) in bacterial membrane environment. Snapshots of initial (left) and final (right) conformations of polymer model T, (C) in solution and (D) in bacterial membrane environment. Cationic, hydrophobic and neutral polar groups are coloured green, red and blue, respectively.

of polar HEMA groups inhibit the formation of a well-packed compact conformation (Fig. 7.8(C) (right)). The initial conformations for binary and ternary random polymers in solution phase are shown in Fig. 7.8(A) (left) and Fig. 7.8(C) (left) respectively. In the membrane phase, the polymer conformations differ significantly with respect to their conformations in solution phase. The random polymer model B shows higher R_g values with little variance around the peak (Fig. 7.7(C)), indicating a stable, almost linear conformation, which is parallel to the membrane surface. In fact, this conformation is due to the acquired amphiphilicity of the polymer in the

membrane environment with cationic AEMA groups pointing towards the anionic PG head groups of the lipid bilayer, segregated from hydrophobic EMA groups that is projected towards the hydrophobic lipid tails (as discussed in section 7.3.1). This can be observed in Fig. 7.8(B) (right) in the x-z plane, with z being the direction of membrane normal.

In case of the Model T polymer however, we observe that there are two peaks in values of R_g (Fig. 7.7(C)) and the time evolution depicts that the R_g values initially stayed quite similar to the values of the model B polymer before undergoing a significant fall at $\sim$ 350 ns and then continuing a downward trend. This is due to its initial extended conformation, having penetrated the membrane from one end while staying perpendicular to the membrane surface, before the polymer folds itself to enter the membrane with its other end at $\sim$ 350 ns and gradually assuming increasingly folded conformations (Fig. 7.1(C)).

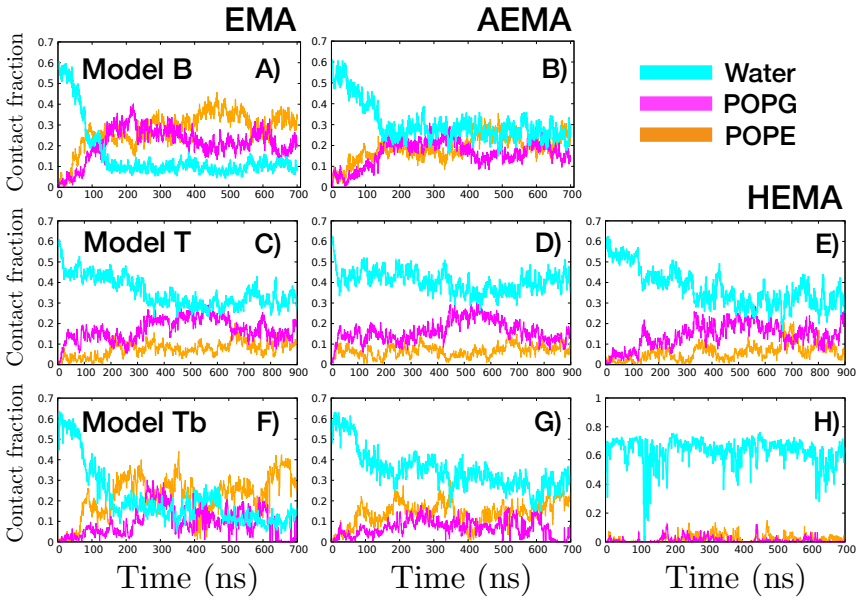

Figure 7.9: Time evolution of the fraction of contacts that are water and lipids (POPE/POPG) surrounding (A, C, F) EMA, (B, D, G) AEMA and (E, H) HEMA groups, for binary and ternary polymers. We calculated the fraction of contacts of the polymer that are with water, lipids and polymer particles within cut-off distance of 7Å. Remaining fraction in the figure are contacts of the polymer with itself.

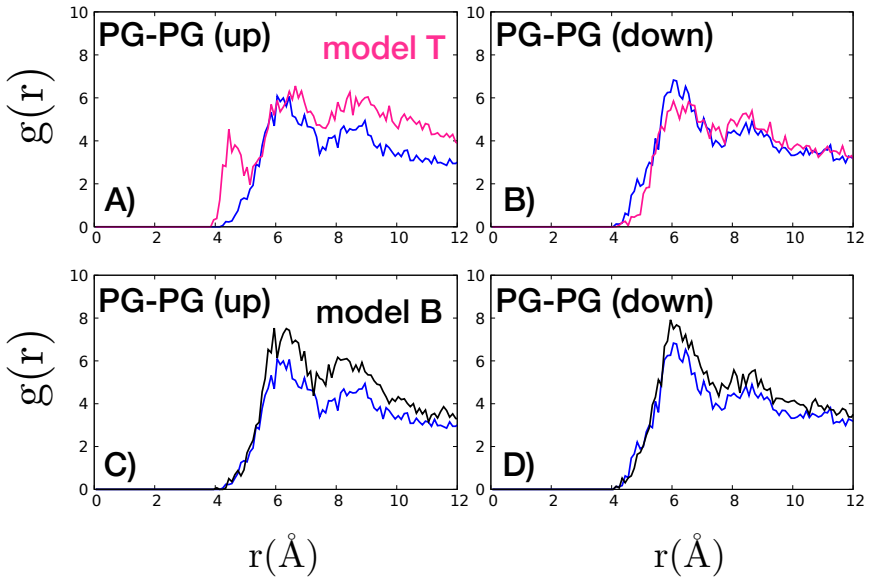

Figure 7.10: g(r) values measured between the phosphate groups of POPG-POPG lipids, averaged over 50 ns (650-700 ns) for the upper (denoted up) and lower leaflets (denoted down) of the model T and model B polymer-membrane systems. For comparison, g(r) for membrane only system is shown in blue colour.

7.3.3 Lipid reorganization in presence of polymer

Next, we explore the chemical composition of the immediate environment surrounding the model polymers. For this, we perform fractional contact analysis. Specifically, we calculate the fraction of water atoms, POPE and POPG lipid atoms as well as polymer atoms in the vicinity of the model polymers. The time series data of the fraction of water and lipids within cutoff of 7 Å around EMA and AEMA groups of the model polymer, is plotted in Fig. 7.9. Ions are not considered, since they form a very small fraction of the total atoms in the system. Fig. 7.9 highlights the evolution of the POPE and POPG lipid species around the groups of the polymer, as the random model polymers (models - B and T) bind and insert into the membrane leaflet. The polymers initiate their journey surrounded by water but within a few nanoseconds, water contacts start being replaced by contacts with lipids species. The data plotted for time evolution of fractional contact of EMA and AEMA groups with the bacterial lipid head groups shows that at $\sim$ 150 ns, stable bound state of

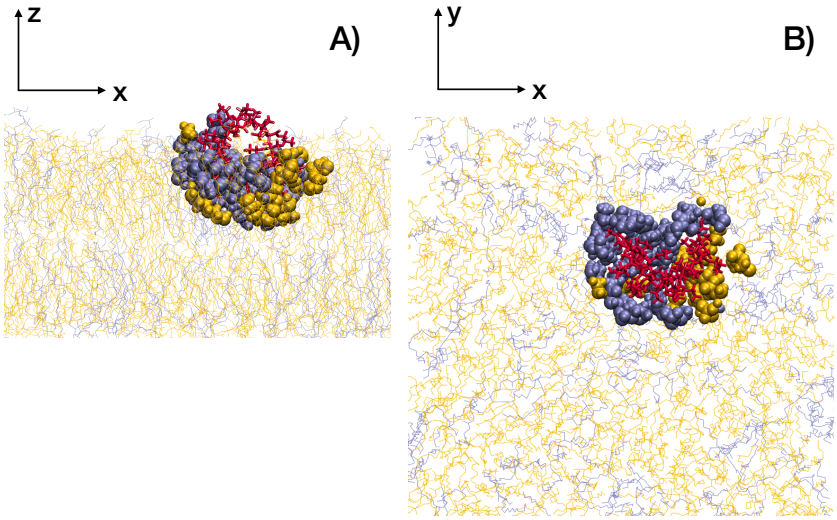

Figure 7.11: Snapshot of model T polymer inserted into the bacterial membrane at the end of 900 ns. The lipid molecules within 5 Å of the polymer are shown in vdW representation, rest of the lipids are in line representaion. POPE, POPG and polymer model T are coloured orange, iceblue and red respectively. POPG seemingly displays higher local concentration around the ternary polymer.

the binary Model B polymer with the bilayer is attained, which then facilitates deeper insertion polymer into the bilayer (Fig. 7.9(A)). Expectedly, water atoms have lowest contacts with the hydrophobic EMA groups. As the polymer is inserted progressively deeper into the leaflet, increasing number of contacts with POPG and POPE lipids are formed. Overall, contacts with POPE lipids dominate contacts with POPG lipids for both EMA and AEMA groups in this case, which is along expected lines since there are a higher proportion of POPE lipids in the membrane. However, for the model T polymer, the situation is strikingly different. One end of the ternary polymer makes quick contact with the bilayer lipids, initially remaining at the membrane-water interface before penetrating deeper. At $\sim$ 350ns, the other end of the polymer bends and starts penetrating the membrane interior, and the polymer grips the membrane from both ends. This is clearly driven by the EMA groups as evidenced by a steep fall in the water contacts around this timescale. Remarkably, we observe that in this case POPG contacts consistently dominate

POPE contacts for EMA, AEMA and HEMA groups, even though as we noted, the number of POPE lipids is more than twice the POPG lipids in the bacterial membrane system. Therefore, this indicates that extensive lipid remodelling occurs in the membrane upon polymer insertion, with a substantial clustering of POPG lipids around the polymer in this case. This is further reiterated by a 2D radial density plot, shown in Fig. 7.10, showing that for a given POPG lipid molecule belonging to the upper bilayer leaflet, the radial probability density of finding POPG - POPG lipid species within 4.5 Å of each other is significantly enhanced for the random ternary polymer (T), as compared to the membrane only system (Fig. 7.10(A)), for comparison, we note no such remodelling occurs in the lower leaflet in Fig. 7.10(B). In Fig. 7.11, a representative snapshot of the POPE (orange colour) and POPG (ice-blue colour) lipids that are within 5 Å around the polymer is given, showing that POPG lipids have a higher concentration around the polymer. Thus, our analysis highlights the considerable membrane remodelling that occurs upon insertion and binding of model T random ternary polymer. It is notable that this effect predominance of POPG contacts over POPE contacts in the neighbourhood of the polymer is not present in case of model Tb polymer. This underscores the role of the polar HEMA groups in effecting lipid reorganisation in membrane phase upon insertion- in model Tb case, the HEMA groups remain localised in aqueous environment and only EMA and AEMA groups penetrate into the membrane interior, so similar to case of model B polymer, in this case also POPE contacts are more numerous as compared to POPG contacts. However, in case of model T polymer, HEMA groups penetrate into the membrane interior alongwith EMA and AEMA groups, which leads to extensive lipid reorganisation, as observed. A natural question now is to examine the change in the physical configuration of the membrane induced by the random ternary polymer. For this, we first investigate the lateral inhomogeinities in the membrane thickness induced by the model T polymer, which we compare with the control system (with no polymer interaction). For this, we plot the thickness

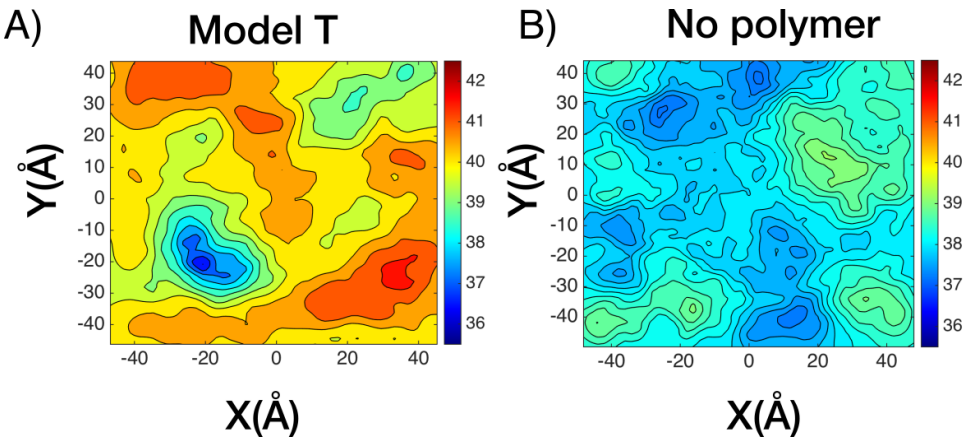

Figure 7.12: Contour plots showing the distributions of local membrane thickness in the X-Y plane for (A) membrane in the presence of ternary polymer (model T) and (B) only membrane (no polymer) system. Bilayer thickness is reported in Å.

profiles across the plane of the membrane, averaged over last 50 ns of simulations, as shown in Fig. 7.12. The 2-D thickness map is calculated using MEMBPLUGIN [230] extension in VMD by interpolating the distance between the phosphate groups of the upper and lower leaflet into the orthogonal grid in the X-Y plane of the bilayer with a grid spacing of 2Å. We observe that the thickness profile for the control system shows a fair amount of uniformity with average overall bilayer thickness around 38.37 ± 0.157 Å. On the other hand, in presence of the model T polymer, a clear upward shift in the average thickness of the bilayer is observed, with average bilayer thickness around 40.400 ± 0.162 Å. The bilayer thickness show considerable non-uniformity throughout the 2-D plane in the presence of ternary polymer, with local thickness value ranging from 35.5 to 42.5 Å, as shown in Fig. 7.12(A). Such lateral inhomogeneity in membrane thickness has been shown to be related to the coarsening of the bilayer leaflet, leading to clustering of anionic and zwitterionic lipids which promote antimicrobial activities [86, 231].

Further, in previous work [202], it has been exhibited that the presence of multiple E4 polymers with aminobutylene cationic side chains in the bilayer reduces the average area per lipid. Strikingly this phenomenon is also observed in our case, with a single random ternary polymer, as well, with the area per lipid for the

model T-membrane system (60.212 ± 0.076)Å^2 being smaller as compared to the control (bilayer with no polymer) system (64.4 ± 0.108)Å^2. Thus, our analysis shows that even a single random ternary polymer, upon membrane insertion, can induce extensive lipid reorganisation, which can then affect the physical configuration of the membrane.

7.3.4 Interaction of random polymer aggregates with bacterial membrane

In this section, we examine interactions of model B and model T polymer aggregates with the bacterial membrane. Both models B and T polymers form aggregates in solution phase, albeit with markedly different morphologies and inter-aggregate interactions, as detailed in Chapter 5. Illustrative configurations of the aggregates in solution, at the end of 150 ns of simulation runs, are shown in Fig. 7.13(A) and Fig. 7.13(B). The formation and stability of such aggregates crucially depends on the hydrophobic content of the individual polymers. Thus, strong aggregations are formed in case of binary polymers, driven primarily by attractive interactions between hydrophobic groups. However, replacing some of the hydrophobic groups with overall charge neutral polar groups weakens the aggregate considerably, leading to increased conformational fluctuations and formation of loose-packed aggregates, in the case of random ternary polymers.

After placing the aggregates of model B and model T polymers over model bacterial membrane, we observe that both the aggregates approach the membrane surface within a few nanoseconds of simulation time, due to the attractive electrostatic interactions between the cationic AEMA groups and the negatively charged head groups of POPG lipid molecules. However, subsequent membrane interaction is substantially different for the binary and ternary aggregates. We first probe the stability of the aggregates while interacting with the membrane by computing the van der Waals

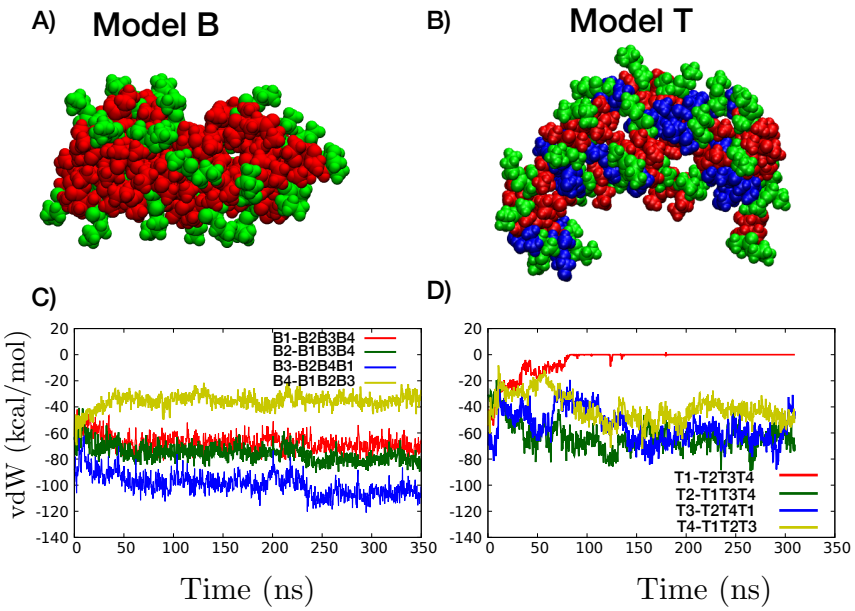

Figure 7.13: Representative configuration of an aggregate of $N_{agg} = 4$, in case of (A) model binary and (B) model ternary polymers in solution phase. The cationic, hydrophobic and polar groups are coloured green, red and blue respectively. Evolution of van der Waals interaction energy with simulation time between each polymer and all others, is plotted for (C) model B and (D) model T aggregates in lipid phase.

interaction energy as a function of simulation time (Fig. 7.13(C) and Fig. 7.13(D)), this data showing the interaction energy between each polymer with all others in the aggregate. Clearly, model B polymers are decidedly stable in the aggregate and show robust attractive interactions among each other. In Fig. 7.14(D), the final configuration of the model B aggregate at $t = 350$ ns of simulation time is shown, with the aggregate lying at the water-membrane interface with no polymer dissociation from aggregate and no penetration into membrane interior. On the other hand, model T polymers show much weaker attractions among themselves with fluctuating interactions. We note that one of the polymer in the ternary aggregate, T1, shows continuous decrease in interaction with other polymers in the aggregate and eventually dissociates at $\sim$ 85 ns from the aggregate. Around the same timescale, the polymer (T1)-lipid interactions become more favourable than the polymer (T1)-polymers (T2T3T4) interactions, as shown in Fig. 7.14(B). It is also notable that the ternary polymer T1 shows identical membrane insertion mode as in the case

of the single polymer simulations for the model T polymer (see Fig. 7.14(C) and Fig. 7.1(B)). Overall, this highlights the importance of the formation of "weak aggregates", as suggested in Chapter 5 in aiding polymer dissociation and partitioning into bacterial membrane, thus strongly indicating the efficacy of ternary polymers as antimicrobial agents.

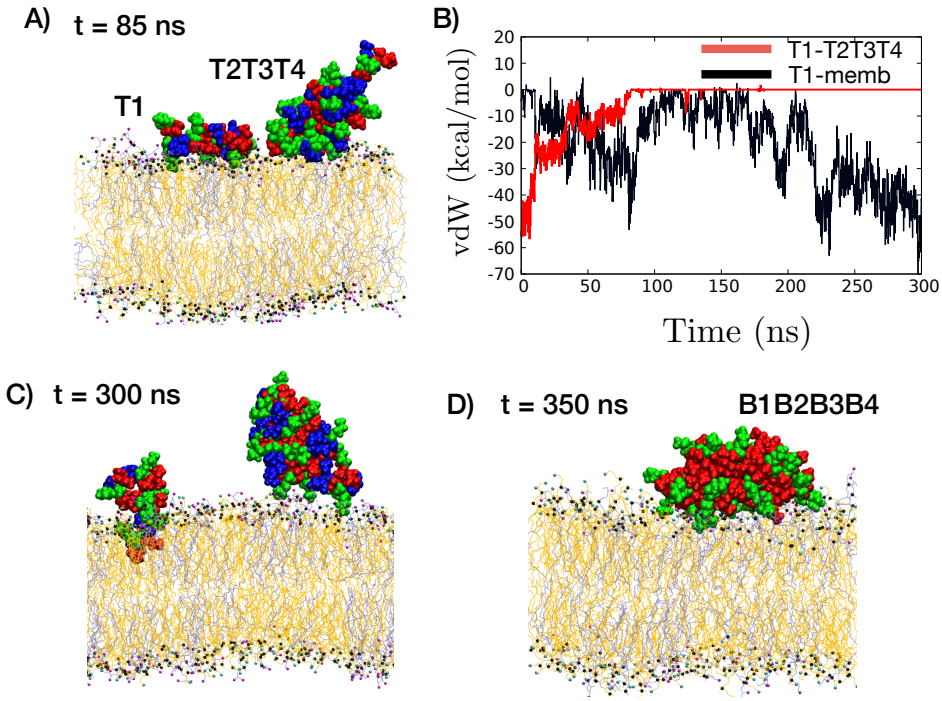

Figure 7.14: (A) Representative snapshot showing separation of polymer T1 from rest of the three polymer for random ternary polymer aggregate in lipid phase. The separation happens in the timescale of $\sim$ 85 ns. (B) van der Waals interaction energy between polymer T1 and all other polymers in the ternary polymer aggregate (red colour) and between polymer T1 and membrane lipids (black colour). (C) and (D) illustrate final snapshots for ternary and binary aggregate at the end of simulation runs. The cationic, hydrophobic and polar groups are coloured green, red and blue respectively. The POPE lipids are coloured orange and POPG lipids are shown in ice-blue colour; the lipid head group atoms are oxygen (magenta), nitrogen (cyan) and phosphate (black).

7.4 Discussion

In this chapter, we explored the interaction of ternary methacrylate biomimetic antimicrobial polymers, composed of hydrophobic, cationic and neutral polar functional groups, on model bacterial membrane. To understand the role played by the neutral polar groups in influencing the membrane interaction of such polymers, we compared it to the membrane interactions of traditional binary AM polymers, which are composed only of hydrophobic and cationic functional groups. Further, to probe the effect of sequence of the functional groups along the polymer chain, the ternary polymers were taken in two configurations, one in which the groups are randomly distributed along the backbone while other in which the polar groups were arranged in a block. Our results show that ternary polymers, specifically those in which the constituent functional groups are randomly distributed, can penetrate deep into the membrane interior while inducing significant lipid reorganisation in its vicinity and change the physical configuration of the membrane. Localization of anionic PG lipid head groups induced by presence of antibacterial agents, which is followed by coarsening of the bilayer and consequent phase boundary defects, adversely affects the integrity of the bacterial membranes leading to cell lysis [85, 231, 232]. Therefore, we can deduce that the presence of the ternary methacrylate antimicrobial polymer in membrane phase will likely result in disruption of membrane, fostering a robust antimicrobial response of such polymers.

It is also notable that the membrane insertion mode of the ternary polymer is markedly different from the binary polymer case. The binary polymer displays acquired amphiphilicity upon insertion into the bilayer, aligning parallel to the membrane surface with the cationic groups interacting with the lipid head groups and the hydrophobic groups interacting with the hydrophobic membrane core. On the other hand, in case of the ternary polymer, such a clear segregation of groups is absent, specifically in case of the random ternary polymer. In this case, the poly-

mer stays aligned in the direction of the membrane normal as it penetrates the bilayer while adopting a folded conformation. This effect is underpinned by two competitive effects involving the presence of the neutral polar groups- attractive interactions with water on one hand and attractive interactions with membrane lipids on the other. Such an effect is however specific to the random ternary polymer, with a block arrangement of the polar groups resulting in a decidedly strong preference for interactions with water, which leads to the positioning of the block of polar groups largely lying in the aqueous environment above the membrane-water interface, impeding a deeper penetration of the polymer into the bilayer. We note here that in general the wide variety of AMPs have varying modes of membrane insertion [71], with for instance, some AMPs adopting a parallel alignment on the membrane surface like LL-37 [233] and indolicidin [234], while some other AMPs inserting into the bilayer perpendicular to the membrane surface, e.g. magainin 2 and lacticin Q [235]. Such effects are likely a result of variations in the sequences of the AMPs due to the presence of different functional groups.

Finally, in view of our results in Chapter 5, where we exhibited the tendency of random ternary polymers to form weak aggregates, we also studied the interaction of aggregates of binary and ternary polymers with model bacterial membrane. We exhibited that in case of the ternary polymers, their weak aggregation behaviour results in fairly rapid disintegration of polymers from the aggregate in this case, with the polymer subsequently penetrating the membrane, following a similar pattern as the membrane interactions of single ternary polymer. On the other hand, the binary polymers, which form strong aggregates, failed to separate from the aggregate to interact with the membrane under similar conditions. It is notable that in previous work [202], interaction of aggregates of binary E4 polymers, having aminobutylene side chains, with bacterial membrane patch had been studied using MD simulations. It was shown in this case that polymers are released into the bilayer from the aggregate due to weak polymer-polymer interactions, which

are overcome by polymer-anionic lipid interactions. However, E4 polymer have 7 charged cationic groups and 3 hydrophobic groups in a polymer chain (with degree of polymerization = 10) [101]. The smaller hydrophobic content of the E4 polymers can explain the weaker aggregate formation, facilitating partitioning and membrane interactions. However, most natural AMPs have only 30% net positive charge [73] and experimental studies have also indicated that antimicrobial activity of polymers starts to level off when cationic groups are more than $\sim$ 30% of composition [23]. Therefore, some cationic groups in E4 polymer may be excessive and not necessarily required for potent antimicrobial activity. On the other hand, higher hydrophobic content clearly leads to formation of strong aggregate, as indicated by our results, obstructing efficient partitioning of the polymers and decreasing the efficacy of their antimicrobial action.

Therefore, in summary, our results indicate that ternary polymers, specifically those which have a random arrangement of functional groups, can effectively act as antibacterial agents due to their weak aggregation behaviour, which results in quick partitioning of polymers into the membrane, with these polymers then penetrating deep into the membrane while inducing significant lipid reorganisation in their vicinity as well changes in membrane physical configuration. It is pertinent to note that natural AMPs typically have several more functional residues other than only cationic, polar and hydrophobic units [78, 236, 237]. The design of polymers, mimicking AMPs in displaying optimised compositions of a multitude of subunits, is of particular significance since it can lead to the development of potent antibacterial agents that can act against a broad spectrum of bacteria. Our present work paves the way for the design of such polymers.

Chapter 8

Conclusion

8.1 Summary of the thesis

In this thesis, we employed biophysical methods to study the design principles of the bacterial cell wall and to study the efficacy of biomimetic methacrylate polymers as antimicrobial agents. In the first part (chapters 2-3), we explored the molecular scale architecture underpinning the viability of the cell wall of bacteria, which is a critical component of the bacterial cell and plays a number of crucial functions for the survival of the cell, including bearing the high internal pressure and ensuring that the cell maintains its characteristic shape. It is primarily composed of the peptidoglycan (PG) network, a sturdy mesh of relatively long and stiff glycan chains cross-linked by peptides. The molecular level architecture of PG mesh displays an array of design components, including length distribution of the glycan chains, degree and placement of peptide cross-linkers along the glycan backbone, whose relevance in the bulk mechanical response of the cell remains to be fully explored and understood. In Chapter 2, we studied the role of various design principles in maintaining integrity of the cell wall. We explained how the glycan strand length distribution, the degree of cross-linking and the placement of the cross-links on the glycan strands can act

in tandem to ensure that the cell wall offers sufficient resistance to propagation of cracks. Further, we suggested a possible mechanism by which peptide bond hydrolysis, via judicious cleaving of peptide cross-links, can act to mitigate this risk of failure. We also studied the reinforcing effect of MreB cytoskeleton, which can offer a degree of safety to the cell wall. However, our results showed that the cross-linked structure of the cell wall is its primary line of defence against mechanical failure. Chapter 3 was motivated by the question of understanding the effect of variability in the material properties of the peptide crosslinkers on the bulk mechanical properties of the cell wall structure of bacteria. Using analytical methods and computer simulations, we studied the response of an appropriately modelled spring system to shear loading and observed how heterogeneities inherent in the system can heighten the resistance to failure. We also studied a discrete step shear loading of the system, exhibiting a transition from quasi-brittle to brittle response controlled by the step size, providing a framework to experimentally quantify the disorder in such structures in general and the PG mesh in particular.

In the second part (chapters 4-7), our aim was to use detailed atomistic molecular dynamics simulations to design antimicrobial polymers that can more effectively mimic the evolutionary optimised design of natural AMPs. Specifically, we made an in-depth study of ternary antimicrobial polymers, constituting of additional functionalities, apart from cationic and hydrophobic moieties which comprise the design of traditional binary AM polymers. Chapter 4 described the technical aspects of molecular dynamics framework and computational models relevant to the thesis work. In Chapter 5, we explored the conformational characteristics of aggregates formed in solution phase by ternary biomimetic antimicrobial polymers, composed of hydrophobic, cationic and polar functional groups and compared it with aggregate morphologies of binary methacrylate polymers, composed only of hydrophobic and cationic functional groups. The results presented here showed that while binary polymers tend to form robust aggregates, replacing some of the hydrophobic groups

with overall charge neutral polar groups weakens the aggregate considerably, leading to increased conformational fluctuations and formation of loose-packed, open aggregates, particularly in the case of random ternary polymers, elucidating the functionally tunable role of inclusion of polar groups in the way antimicrobial agents interact with each other in the solution phase, which can eventually dictate their partitioning into bacterial and mammalian membrane. Chapter 6 discussed another class of ternary polymers, composed of cationic, hydrophobic and anionic functionalities and investigated the formation and lifetime of salt bridges between pairs of oppositely charged cationic and anionic moieties and the effect of such interactions on the conformations of the polymer in solution phase. In particular, we showed how salt bridges act like transient cross-linkers, leading to a dynamic switching between extended and compact conformations in such polymers. Finally, in Chapter 7, we examined the interaction of methacrylate ternary and binary polymers and their solution phase aggregates with model bacterial membranes. We showed that random ternary polymers can penetrate deep into the membrane interior and partitioning of even a single polymer has a pronounced effect on the membrane structure. While binary polymers exhibited strong propensity to adopt acquired amphiphilic conformations upon membrane insertion, the results presented here exhibited that such amphiphilic conformations are absent in the case of random ternary polymers, which adopt a more folded conformation, staying aligned in the direction of the membrane normal and subsequently penetrating deeper into the membrane interior suggesting a novel membrane partitioning mechanism without amphiphilic conformations. Finally, we also examined the interactions of ternary polymer aggregates with model bacterial membranes, which showed that replacing some of the hydrophobic groups by polar groups leads to weakly held ternary aggregates enabling them to undergo rapid partitioning and insertion into membrane interior.

8.2 Future directions

Now, we outline a few directions of research that stem from the work presented in this thesis. In the first part of the thesis, we studied the mechanical structure of the cell wall of Gram negative, rod shaped bacteria *E.coli*, probing the design components of the PG network of such bacteria and their role in ensuring cell viability. A natural direction then is to probe the structure of Gram positive bacteria of rod shaped (e.g., *B.subtilis*) and other geometries (e.g. *S.aureus*, which has a spherical geometry), which have been much less studied as compared to the mechanical structure of the Gram negative cell wall. Gram positive bacteria have a complex, interconnected, multi-layered PG network, which can span $\sim$ 20 layers or more [166] and is consequently, much thicker than the cell wall of Gram negative bacteria. The turgor pressure in the case of Gram positive bacteria is also higher ($\sim$ 20 atm for *B.subtilis*). It has been hypothesized that Gram positive PG network evolves obeying an inside-to-outside model, in which fully formed PG layers are deposited at the base of the cell wall and slowly progress outwards while getting hydrolysed and ultimately are ejected out of cell wall into the environment [238]. This provides an interesting perspective to study the PG network in this case as a "composite" material, due to the different layers of the PG network, being subjected to different levels of hydrolysis, will have differential elastic properties. The key questions will be to understand the role of such a composite structure in ensuring cell viability, in offering protection against crack propagation while retaining the ability to withstand high turgor pressure. Similarly, to build upon the work presented in Chapter 3 of this thesis, future work can involve incorporating the dynamics of the cell wall and the elasticity of the glycan strands into the model presented here along with local transfer of load when a cross-link ruptures, from which stress concentrations and pore size distributions can be computed and compared with experiments and simulations, which can lead to further insights on the structure of the cell wall and

shed light on its surprising viability against all odds. It is also natural to explore non linear spring models of the PG network, as recent work has suggested the likelihood of the peptide cross-linkers displaying a non-linear loading response [121], a deeper analysis of which, can shed light on the precise mechanical benefits that accrue to the cell if the peptide cross-linkers display a non-linear response to loading.

In the second part of the thesis, we studied the behaviour of ternary AM polymers in solution phase and their membrane interactions. The evolutionarily optimized design of naturally occurring AMPs consists of multiple functionalities, whose precise role in ensuring broad spectrum anti-microbial efficacy and selectivity remains to be elucidated [236, 237]. Thus, while in this thesis, ternary polymers were explored as a closer approximation to the design of anti-microbial peptides as compared to the traditional binary design of AM polymers, a lot of work remains to be done to understand the precise reason behind the presence of multiple functionalities in the design of AMPs and incorporating such features into the design of synthetic AM polymers while ensuring ever increasing levels of anti-microbial efficacy and selectivity. Further, here atomistic simulations were utilized to study AM polymers and their membrane interactions. A natural direction is then to employ coarse-grained modelling of such polymers to study their membrane interactions at spatio-temporal scales that can approximate experimental scenarios. In particular, such methods can unravel the precise modes of disruption in membrane structural properties caused by AM polymers. Another avenue is to explore multi-scale modelling of the bacterial cell envelope (comprising the outer membrane, cell wall with a thin PG layer and the inner membrane for Gram negative bacteria and the cell wall with a multi-layered PG network and the cell membrane in case of Gram positive bacteria) and the action of anti-microbial agents on it. Such a study will lead to an in-depth understanding of how the cell envelope, the first line of defence of bacterial cells, protects it against external threats and how the design of anti-microbial agents can be optimized to overcome the same.

Synopsis

Bacteria are single celled, prokaryotic micro-organisms that were one of the first life forms to appear on earth and have since emerged as one of the most successful organisms as well, populating habitats as diverse as hot springs, human gut, even radioactive waste [1]. They have formed complex and varied associations with humans, which in several instances has turned out to be beneficial for both. However, bacteria are also responsible for causing several serious diseases in human beings, including tuberculosis, diptheria, typhus, leprosy [2]. A crucial step in managing such bacterial infections has been the development of antibiotics, which fight bacterial infections either by killing bacteria or by slowing its growth, usually by impeding crucial cellular functions like cell wall synthesis and protein synthesis in the cell. However, several strains of bacteria have started displaying an alarming rise in resistance to antibiotic treatment. This has rendered several commonly used antibiotics largely ineffective. Indeed, strains of the bacteria *Escherichia coli* have even developed resistance to colistin and carbapenem, two antibiotics of "last resort" [3]. It has been estimated that by 2050, infections from multi-drug resistant pathogens will cause higher mortality than cancer [4], which gives an insight into the graveness of this public health crisis. This necessitates the exploration and design of newer antibacterial agents. For this, an important pathway is to utilize biophysical methods to unravel the design principles of the bacterial cell and to model the action of antimicrobial agents on them, thus enabling us to effectively design and test the efficacy of new age antibacterials.

This thesis is divided into two parts. In the first part, we study the design features of the cell wall of bacteria, which is primarily composed of the peptidoglycan (PG) network, a mesh of relatively long and stiff glycan chains, cross-linked intermittently by flexible peptides. We explore the molecular scale architecture of the PG mesh and its role in enhancing the toughness or the resistance to crack propagation,

of the cell wall, utilizing theoretical methods. We also investigate the effect of variability in the elastic properties of the PG mesh on its bulk mechanical response, by studying an appropriately modelled spring system using theoretical methods and simulations. In the second part of the thesis, we study the conformational landscape, aggregation dynamics and interactions with model bacterial membrane of biomimetic antimicrobial polymers (AMPolys), utilizing detailed atomistic molecular dynamics simulations. We specifically examine the role played by neutral polar groups in influencing the aggregation dynamics of such polymers in solution phase and study their membrane-interactions in depth. Further, we also investigate the conformational landscape of AMPolys that have anionic functional groups as constituents, with particular focus on probing the formation of salt bridges and their role in determining the conformational dynamics of such polymers.

Design principles of the bacterial cell wall

The cell wall is a critical component of the bacterial cell and plays a number of important roles, including resisting the high internal pressure (referred to as turgor pressure) and ensuring that the cell maintains its characteristic shape [5]. It is composed primarily of the peptidoglycan (PG) network, a sturdy mesh of relatively long and stiff glycan chains cross-linked intermittently by peptides. The molecular level architecture of the PG mesh displays an array of design components, including length distribution of the glycan chains, degree and placement of peptide cross-linkers along the glycan backbone, whose relevance in determining the bulk material properties of the cell wall remains to be fully explored and elucidated.

Safeguarding the bacterial cell wall against mechanical failure

For ensuring cell survival, the cell has to be stiff enough to bear the high turgor pressure and tough enough to prevent mechanical failure due to propagation of cracks. It is therefore natural to explore the molecular scale design features of

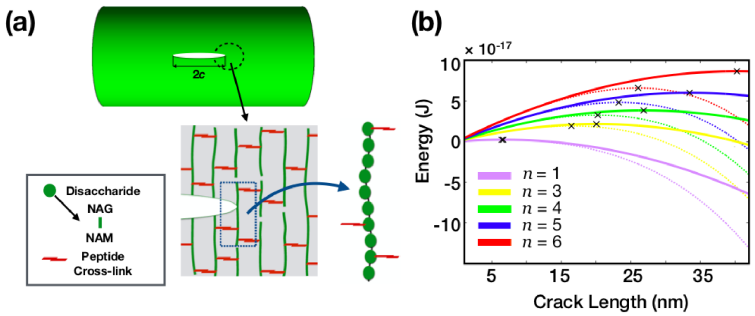

Figure 1: (a) A longitudinally aligned crack on the cell wall. Near the tip, the crack comes up against a glycan strand, which are composed of disaccharide units consisting of alternating sugars NAG and NAM connected by a glycosidic bond. (b) Plot of total energy as crack length varies, for different degrees of effect of cross-linking. The solid lines represent the plane case, while dotted lines represent the cylinder case. The cross ($\times$) represent the critical crack lengths.

the cell wall, specifically the PG mesh, which allow the mechanical requirements necessary for cell survival to be satisfied. While the stiffness of the cell wall has been well studied [6, 7], here we study the role of various design components of the cell in securing the cell wall by enhancing its toughness. In particular, we examine the role of the geometry of the cell, the cross-linked polymeric structure of the cell wall and the role of the MreB cytoskeleton [8] in ensuring stabilization of the cell wall against crack propagation. Our model, specifically, studies the Gram-negative rod-shaped bacteria (e.g. *E.coli*), with a single layer of the peptidoglycan mesh, with glycan strands oriented in the circumferential direction [9]. Our main results are summarized below-

- We show that cross-linking is crucial for maintaining the integrity of the cell wall, since the minimum energy needed for crack propagation, called the tearing energy, is largely controlled by the degree of cross-linking. We estimate the critical crack length for varying degrees of cross-linking, showing that it varies inversely with the degree of cross-linking (Fig. 1).

- We also show that terminally cross-linked short length glycan strands can greatly enhance the tearing energy. In particular, we show that for about 30%

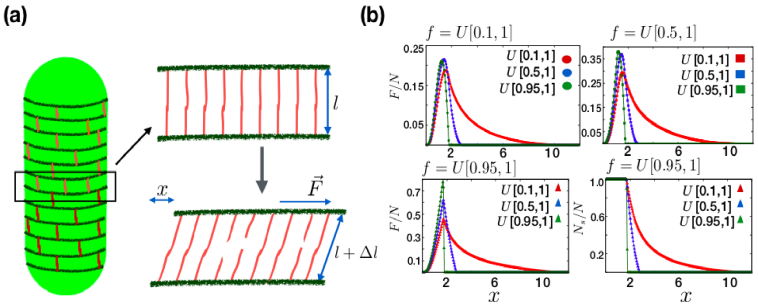

Figure 2: (a) Schematic representation of spring system considered, subjected to shear loading. (b) Force-extension curves of spring systems and fraction of intact springs, with values of spring constant and rupture strength distributed as independent uniform distributions.

cross-linking of the cell wall, as has been observed for *E.coli* [10], the optimal length of the glycan strands for maximizing the tearing energy, are shorter length glycan strands with length $\sim 7-8$ disaccharides, cross-linked at the ends. This provides an explanation for surprising experimental observations, which have demonstrated an abundance of shorter length filaments in the peptidoglycan mesh [11] and of the strong preference of glycan strands to cross-link to each other at the termini [10, 12].

- We also investigate the effect of the reinforcement of the cell wall by the actin homologue MreB cytoskeleton. Modelling MreB as several disconnected bent cylinders, we estimate the inward pressure exerted by it for a wide range of parameters. We conclude that the effect of the cross-linked structure of the cell wall plays the primary role in ensuring its integrity.

Modelling heterogeneities in the cross-linked bacterial sacculus

The PG mesh in the bacterial cell wall undergoes persistent remodelling in the cell, with cleaving of older cross-links under the action of hydrolases, incorporation of new cell wall material into it and the consequent formation of newer cross-links, a process that is essential for the growth of the cell [13]. This results in the presence of newer cross-links as well as hydrolase-degraded older cross-links in the cell

wall. While the exact mechanical effect of hydrolases on the peptide cross-linkers is unclear, this effect can result in the lowering of rupture strength of the bond or lowering of the stiffness of the bond or both, introducing heterogeneities into the ultrastructure of the PG mesh, specifically in the mechanical properties of the cross-linkers. This is further evidenced by experimental observations in Ref. [14], where isolated cell wall fragments subjected to sonication showed an immediate drop in the degree of cross-linking that persisted even as the structure remained intact, before becoming relatively constant after a period of time. This suggests that the peptide cross-linkers act in a differential manner under loading, due to variations in their elasticity and rupture strengths. A natural question then is to understand effect of the variability in the mechanical properties of the cross-linkers, specifically their strength and elasticity, on the bulk mechanical response of the cell wall. Motivated by this and as a first step, here we explore a spring system, in which we incorporate variability in both the spring constant of the constituent springs as well as their rupture strengths and study the response of the system to shear loading (Fig. 2(a)). Our main results are summarized below-

- We derive the force extension relation and show that in general, wider variability in the elasticity of springs can ensure more robust resistance to failure but it also lowers the load capacity whereas lower variability results in a more brittle response to loading even as the load capacity increases (Fig. 2(b)). Our analysis suggests that a possible mechanism for hydrolytic action to act on the cross-linkers in a safe manner while ensuring sufficient load bearing ability is by maintaining high order of variability in the spring constants while limiting the variability in the rupture strengths.

- Next, we examine a step wise loading regime which allows us to exhibit a quasi-brittle to brittle transition as the load per step increases. This transition, which is a feature that seems universal in systems which have inhomo-

geneities built into their ultrastructure, has been observed in other natural materials, e.g. snow [15] and can be useful tool to experimentally detect such inhomogeneities present in the system.

- We also study the case when the distributions of the spring constants and the rupture strengths of the constituent springs in the system are (positively or negatively) correlated. We show that while in the case of positive correlation, the response to loading is considerably brittle, negative correlation of spring constant and rupture strength values results in quasi-brittle behaviour, although the maximum load carrying capacity drops.

Designing new class of ternary antimicrobial polymers

Biomimetic antimicrobial polymers, or AMPolys, have been a focus of research in recent times due to the possibility of their usage as novel therapeutic agents against infectious pathogens [16]. Such polymers are designed based on the basic functional themes present in the large class of naturally occurring AM peptides [17]. Most of the studies on AMPolys have focused on inclusion of only cationic and hydrophobic groups as primary constituents of designed biomimetic polymers [16, 18]. However, in such binary polymers it is very difficult to optimize the monomer composition appropriately for potent antibacterial activity and reasonable selectivity. Indeed, naturally occurring AMPs are not just binarily composed of hydrophobic and cationic functionalities, but are typically composed of multiple functional groups. For instance, neutral polar residues are one of the most common constituents of natural AMPs [19]. Similarly, while most AMPs display a net charge of +2 to +9, several of them, such as defensin, magainin, LL-37, contain negatively charged amino acids in their sequences [20]. Here, using detailed atomistic molecular dynamics (MD) simulations, we study ternary biomimetic copolymers, by incorporating additional functionalities in their design, as compared to traditional binary polymers. This

opens up not only new paradigms of designing more effective AM polymers with more nuanced mechanisms, but also helps in delineating the specific contributions of different functional groups in such polymers.

Role of polar group in the aggregation dynamics of biomimetic polymers in solution phase

We explore the conformational landscape of aggregates formed in solution phase by ternary biomimetic antimicrobial (AM) methacrylate polymers, composed of hydrophobic, charged cationic and polar functional groups and compare it with aggregate morphologies of binary methacrylate polymers, composed only of hydrophobic and charged cationic functional groups (Fig. 3(a) and Fig. 3(b)). The effect of sequence of the functional groups on aggregate conformation is also studied by considering random and block sequences along the polymer backbone. This study elucidates the functionally tuneable role of inclusion of polar groups in the way antimicrobial agents interact with each other in solution phase, which can eventually dictate their partitioning behaviour into bacterial and mammalian membranes. Our main results are summarised below-

- We show that block polymers tend to form larger sized aggregates displaying more compact structures as compared to their random counterparts. The binary polymers, composed of charged and hydrophobic functional groups, form relatively well packed, stable aggregates. However, there are differences in the aggregate morphologies arising due to differential sequencing of the constituent groups along the polymer backbone: while block binary (model BB) aggregates display a spherical conformation with a remarkably strong hydrophobic core which is almost impermeable to water surrounded by cationic groups, the random binary (model B) aggregates display a more ellipsoidal shape with relatively weaker core displaying higher permeability to water.

- We study in detail the effect of presence of polar HEMA groups in ternary

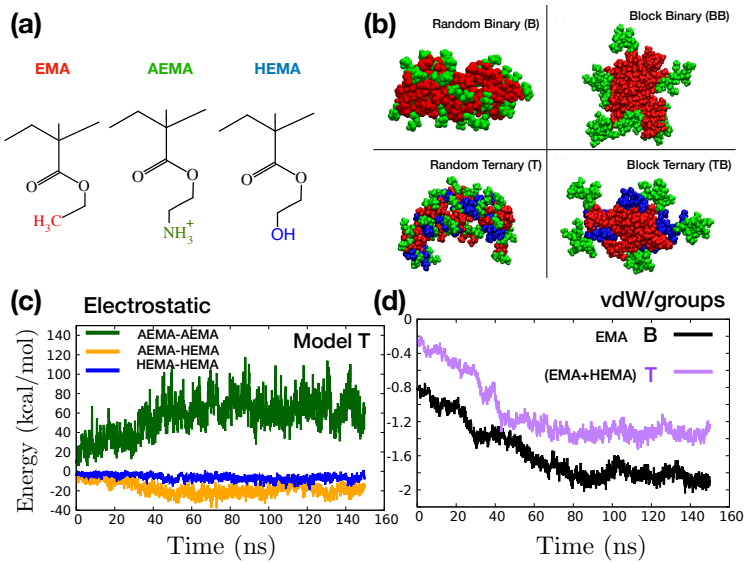

Figure 3: (a) Functional groups (EMA: hydrophobic, AEMA: charged cationic, HEMA: neutral polar) in the model polymers. (b) Representative snapshots of the aggregates of binary and ternary polymers, in random and block arrangements, in solution phase. EMA, AEMA and HEMA groups are shown in red, green and blue colour respectively. (c) Total electrostatic energy is plotted as a function of simulation time for the model T aggregate. (d) van der Waals energy per group is plotted as a function of simulation time for the model B aggregate and model T aggregate.

polymers in determining their aggregation dynamics, exhibiting that this induces conformational fluctuations and in general, results in the formation of loosely packed, somewhat extended aggregates, particularly in the case when the groups are randomly distributed along the polymer backbone.

- We also examine the effect of polar HEMA subunits on the binding energies of the inter-polymers in the aggregate, showing that replacing some of the hydrophobic groups by polar groups disperses the overall hydrophobicity of the aggregates while retaining the total attractive van der Waals interactions and counteracting the strong repulsive electrostatic interactions between the cationic groups. The HEMA groups also form attractive electrostatic interactions with both cationic AEMA and polar HEMA groups, which contribute to aggregate formation (Fig. 3(c) and Fig. 3(d)).

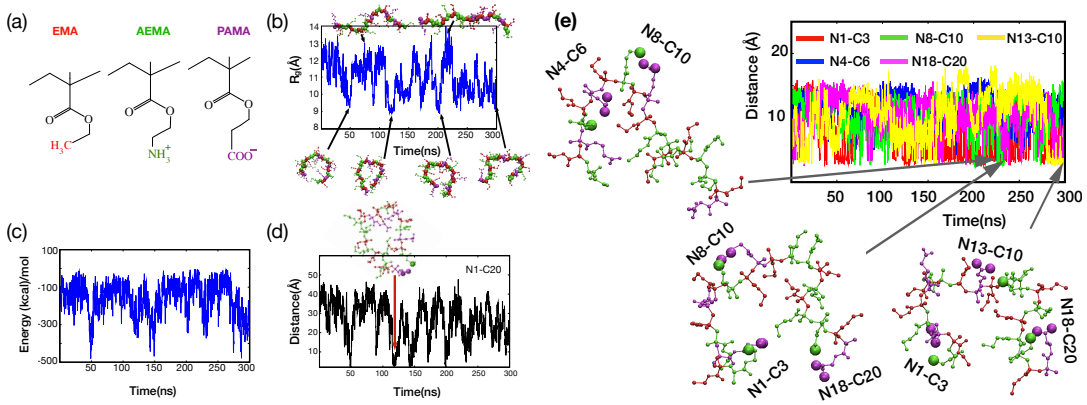

Figure 4: (a) Functional groups and the sequence of the model polymer considered, (b) Radius of gyration (R_g) of model polymer as a function of simulation time and representative snapshots of the polymer in extended and ring-like conformations. (c) Electrostatic interaction between the anionic PAMA and cationic AEMA groups. (d) Time series of the distance between the two most sequentially distant oppositely charged pairs in the polymer chain. (e) Multiple salt bridges formed in the polymer at same time, with the representative polymer conformation.

- Our analysis thus indicates that the role of inclusion of polar groups in ternary polymers is two-fold: (1) to reduce possible strong local concentration of hydrophobic groups and "smear" the overall hydrophobicity along the polymer backbone to increase the solubility of the polymers (2) to compensate the loss of attractive hydrophobic interactions by forming attractive electrostatic interactions with the cationic groups and contribute to aggregation formation, albeit weak.

Role of anionic functional groups in conformational landscape of biomimetic polymers in solution phase

Negatively charged amino acids occur in the sequences of several natural AMPs [20]. A natural question then is - What is the role played by these negatively charged moieties? In this context, the role of salt bridge formation in protein structure and function has long been explored- salt bridge interactions between anionic and cationic amino acids contribute to the structural stability of proteins and can play a significant role in determining the conformational landscape. For instance, in

case of α-defensin AMPs, salt bridges induce increased structural flexibility, which enhance peptide sensitivity to proteolysis, in addition to conferring stability [21]. Here, we explore the structural effect of inclusion of negatively charged monomers in biomimetic AMPolys, in determining the conformational landscape of such polymers in solution phase. The model polymers considered are composed of hydrophobic (EMA), cationic (AEMA) and anionic (PAMA) functional groups (Fig. 4(a)). We investigate the formation and lifetime of salt bridges between pairs of oppositely charged cationic and anionic moieties and the effect of such interactions on specific conformations of the polymer in solution phase. Our main results are summarised below-

- We show that the model polymers dynamically switch between compacted and extended conformations (Fig. 4(b)), with the sequence of the functional groups along the polymer backbone playing a role in influencing the conformational landscape.

- To understand the formation and stability of salt bridges, we analyse the distance between various possible ion-pairs for model polymers considered. We establish that salt bridge formation is consistently exhibited, particularly after around 100 ns of simulation time. Our analysis also shows that multiple salt bridges can form at the same time (Fig. 4(e)).

- Our results show that salt bridges act as transient cross-linkers, which affect polymer conformation and lead to a dynamic switching of compact and extended conformations. However, the salt bridges do not exert the polymers to adopt specific conformations.

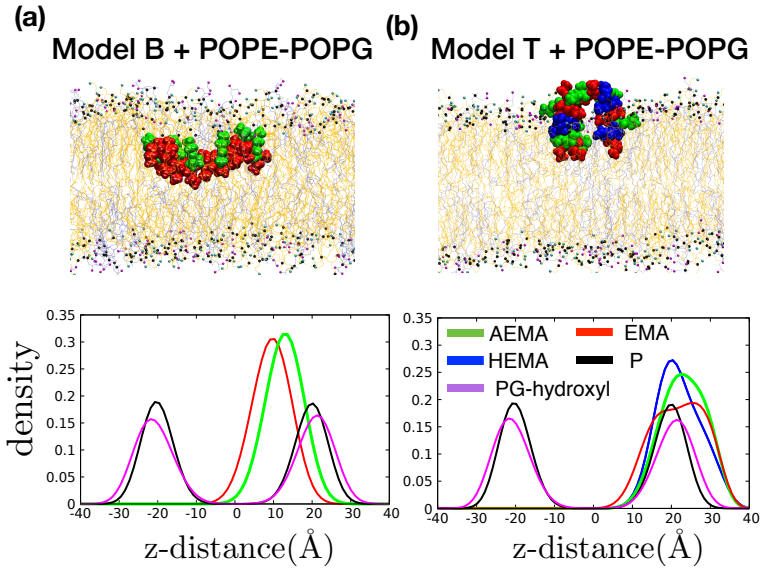

Figure 5: (a,b) Representative snapshot of interaction of binary (model B) and ternary (model T) polymer with model bacterial membrane. Density profiles of various components of lipid-polymer systems POPE-POPG-Model B, POPE-POPG-Model T are also shown. Green colour represents the polymer charged group, red represents the polymer hydrophobic group and blue marks the polymer polar group. The density profile of phosphate atoms, hydroxyl groups of POPG lipids are shown in black and magenta, respectively.

Role of polar groups in interaction of ternary polymers with model bacterial membrane

Finally, we examine the interaction of methacrylate ternary AMPolys, composed of charged, hydrophobic and neutral polar groups, with model bacterial membrane and compare it with the membrane interaction of binary polymers. The model bacterial membrane that was used to study the membrane interactions of the AM polymers was composed of POPG and POPE lipids in a 3:7 ratio, which is similar to the inner membrane composition of the Gram negative bacteria *E.coli* [22]. Our main results are summarised below-

- Our simulation data shows that random ternary polymers can penetrate deep into the membrane interior. Membrane insertion modes are also shown to be significantly different for binary and ternary polymers. While binary polymers exhibit acquired amphiphilic conformation upon membrane insertion, with

cationic amide groups localizing close to the interfacial lipid head groups, the hydrophobic moieties buried deeper within the hydrophobic tails of the bilayer and the polymer adopting a conformation parallel to the membrane orientation (Fig. 5(a)), we find that a clear segregation of groups is absent in ternary polymer case (Fig. 5(b)), as had been surmised in previous experimental work [23]. The ternary polymer adopts a folded conformation perpendicular to the membrane upon insertion.

- To understand the effect of polymer binding on membrane configuration, we examine lipid reorganization in the vicinity of the model polymers in membrane phase and observe the strong affinity of the ternary polymer for POPG lipids, resulting in substantial lipid reorganization in polymer neighbourhood.

- Finally, we study interactions of aggregates of binary and ternary polymers with bacterial membrane, showing that the weaker ternary aggregate undergoes fairly rapid partitioning and subsequent membrane insertion while polymer partitioning is robustly obstructed in case of the strong binary aggregates. Our work therefore highlights strong indications of effective bactericidal action of ternary copolymers, depicting a good degree of penetration into interior of bacterial membrane, while inducing extensive lipid reorganization in the process.

Thesis Keywords

Name of the Student: Garima Rani
Name of the CI/OCC: The Institute of Mathematical Sciences (IMSc), Chennai
Enrolment No.: PHYS10201504003
Thesis Title: Understanding the mechanical response of bacterial cell walls and cell membranes against antimicrobial agents
Discipline: Physical Sciences **Sub-Area of Discipline:** Biophysics
Date of viva voce: 04/01/2021

Thesis Keywords: *Bacteria, Cell Wall, Cell Membrane, Biomechanics, Antimicrobial Polymers, Molecular Dynamics.*

Thesis Highlight

Name of the Student: Garima Rani

Name of the CI/OCC: The Institute of Mathematical Sciences (IMSc), Chennai.

Enrolment No.: PHYS10201504003

Thesis Title: Understanding the mechanical response of bacterial cell walls and cell membranes against antimicrobial agents

Discipline: Physical Sciences **Sub-Area of Discipline:** Biophysics

Date of viva voce: 04/01/2021

Bacteria are responsible for causing several serious diseases in human beings. A crucial step in managing such bacterial infections has been the development of antibiotics, which fight bacterial infections either by killing bacteria or by slowing its growth. However, several strains of bacteria have started displaying an alarming rise in resistance to antibiotic treatment. This has rendered several commonly used antibiotics largely ineffective. This necessitates the exploration and design of newer antibacterial agents. For this, an important pathway is to utilize biophysical methods to unravel the design principles of the bacterial cell and to model the action of anti-microbial agents on them, thus enabling us to effectively design and test the efficacy of new age antibacterials.

Here, biophysical methods were employed to study the design principles of the bacterial cell wall and to study the efficacy of biomimetic methacrylate polymers as antimicrobial agents. The molecular level architecture of the peptidoglycan (PG) mesh, the primary component of the cell wall, and its role in enhancing the toughness of the cell wall was explored in detail. The effect of variability in the elastic properties of the PG mesh on its bulk mechanical response was also investigated. Next, the conformational characteristics, aggregation dynamics and interactions with model bacterial membrane of biomimetic methacrylate ternary antimicrobial polymers (AMPolys) were studied, utilizing detailed atomistic molecular dynamics simulations. The aim here was to go beyond the traditional binary composition design, constituting hydrophobic and charged cationic groups, of such AMPolys, by including additional functional groups in order to better optimize their antimicrobial action. In this context, the role played by neutral polar groups in influencing the aggregation dynamics of such polymers in solution phase and their membrane-interactions was studied in depth, highlighting the anti-microbial efficacy of ternary polymers, which can undergo rapid partitioning and deep insertion into membrane interior.

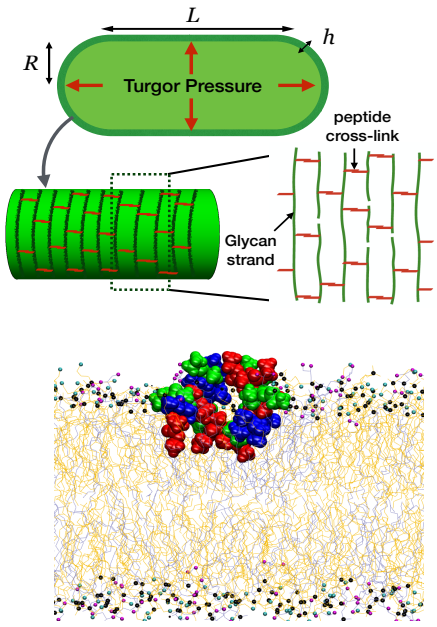

Figure 1. (Top) Peptidoglycan mesh in the bacterial cell wall. (Bottom) Ternary AMPoly interacting with bacterial cell membrane.